ADVANCED BULK NANOCOMPOSITE MATERIALS FOR THERMOELECTRIC APPLICATIONS

BY

Chen Zhou

A DISSERTATION

Submitted to
Michigan State University
in partial fulfillment of the requirements
for the degree of

DOCTOR OF PHILSOPHY

Materials Science and Engineering

2011

ABSTRACT

ADVANCED BULK NANOCOMPOSITE MATERIALS
FOR THERMOELECTRIC APPLICATIONS

BY

Chen Zhou

Thermoelectric materials have received rejuvenated interest for the past two decades due to the theoretical predictions that a high dimensionless thermoelectric figure of merit ZT > 1 can be obtained in materials with complex structures and reduced dimensions, termed "nanostructured materials". The underlying benefit of nanostructuring is the possibility of at least partially decoupling the interdependent relation between the Seebeck coefficient and electrical conductivity so that one has the flexibility to tune them individually. The thermal conductivity is expected to be reduced at the same time due to the phonon scattering from the nanoscopic interfaces.

In this work, we investigate the thermoelectric properties of bulk nanocomposite materials, which boast both ease of synthesis and enhanced thermoelectric performance originating from the reduced dimension. Two material systems are of our interest: bismuth telluride and p-type skutterudite.

For bismuth telluride and its alloys based nanocomposites, we select $Bi_2Te_{2.85}Se_{0.15}$ as the n-type matrix and $Bi_{0.4}Sb_{1.6}Te_3$ as the p-type matrix respectively. The nanocomposite materials were prepared by a solution based incipient wetness impregnation method. Adding PbTe nanoparticles can effectively reduce the lattice thermal conductivity at low temperature.

But the doping effect from the excess Pb ion plays a dominant role compared to nanostructuring. This results in creating a two carrier system for the n-type nanocomposites, and decreased power factors for p-type nanocomposites.

For skutterudite based nanocomposites, we focus our attention on the under-developed p-type skutterudites. We start from the primitive Fe-doped binary skutterudite nanocomposite $Co_{0.9}Fe_{0.1}Sb_3$ with in-situ formed $FeSb_2$ as nanoparticles and demonstrate 100% enhancement in the overall thermoelectric performance. The success encouraged us to re-develop an Yb-filled skutterudite as the matrix material and explore the thermoelectric properties over a wide range of Yb filling fraction with various amount of antimonide based impurities (presumably $FeSb_2$). We achieve an enhanced thermoelectric performance up to 23% in optimized nanocomposites compared to the control sample.

Last but not least, we investigated the double filled p-type skutterudite $Yb_{0.6}Ga_zFe_2Co_2Sb_{12}$. The unique role of Ga inducing a deep defect level in band structure enhances the Seebeck coefficient without affecting the electrical resistivity. The best performing sample demonstrates 46% enhancement of thermoelectric performance compared to $Yb_{0.6}Fe_2Co_2Sb_{12}$ with only Yb filler.

Overall, our study indicates that nanostructuring does provide significant benefits when applied to thermoelectrics under certain conditions. Time and more research will tell if this approach is ultimately a viable one.

Copyright by

Chen Zhou

2011

To Wen, my parents
and
paternal grandparents

ACKNOWLEDGEMENTS

I feel fortunate to have found Prof. Donald Morelli as my advisor, the person who introduced me to the field of thermoelectricity and experimental materials physics. I knew little about thermoelectrics and had limited laboratory experience when I first joined him. It is Prof. Morelli who taught and advised me from the very basics of equipment operations and material synthesis all the way to data interpretation, conference presentation and journal publication. I still remember the first time when he showed me how to mount a sample on a cryostat and the days when we kneeled on the floor to fix the broken vacuum pump. I am very impressed by his keen intuition and foresight, extreme patience and kindness to students, and his optimistic and altruistic characters. Pursuing a PhD degree is not an easy task. But with the guidance and encouragement from my advisor, my PhD life has been a memorable and pleasant journey.

I would also like to thank my other PhD committee members for their guidance and contribution. Prof. Sakamoto introduced me the novel material synthesis techniques and generously allowed me to use some of his equipment for my research. He is always full of ideas and offers constructive critique on my work. Prof. Subramanian's class on crystal anisotropy is one of the best classes that I have had in the graduate school. Prof. Hogan generously shared his thermal measurement instrument with us and offered many good suggestions.

I am blessed to have the opportunity to work with renowned professors and very talented colleagues from other institutions in the framework of the RMSSEC Energy Frontier Research Center. They are Prof. Brock and Dr. Shreyashi Ganguly from Wayne State University; Prof.

Ctirad Uher and Dr. Xiaoyuan Zhou, Dr. Guoyu Wang, and Mr. Hang Chi from University of Michigan.

Many thanks go to my colleagues Dr. Yanzhong Pei (former post-doctoral associate in our group), Dr. Long Zhang, Dr. Ponnambalam Vijayabarathi, Mr. Eric Skoug, Mr. Chang Liu, Mr. Hui Sun, Mr. Xu Lu, Mr. Hao Yang, Miss Gloria Lehr and Mr. Steve Boona, with whom I built and shared the laboratory. I am especially thankful to technician Brian Wright for assisting me with thermal measurement; technician Gary Keeney for gladly taking the extra effort to help me machine parts; and the MSU Physics machine shop manager Tom Palazzolo and other technicians for their fast handling of my machining requests.

I also benefited tremendously from fruitful discussion with Prof. Joseph Heremans from the Ohio State University on the topic of Nernst coefficient measurement.

Last but not least, I want to thank my beloved wife Wen for her unconditional support, warm encouragement, tender care and endurance during the past three years. I feel to be a better person with her in my life. I am also indebted to my parents and paternal grandparents for nurturing me, educating me through my youth and the sacrifices they made. Their noble characters are beacons in my soul. I am grateful to all of my relatives, home and abroad, who have consistently supported me and encouraged me. This dissertation is also dedicated to them.

TABLE OF CONTENTS

LIST OF TABLES x

LIST OF FIGURES xi

Chapter 1 Introduction to Thermoelectricity 1
1.1 The thermoelectric effect 1
1.2 The efficiency for thermoelectric device 3
1.3 Electron transport 7
1.4 Thermal transport 11
1.5 The effect of low dimensional materials 17
1.6 The state-of-the-art thermoelectric materials 19

Chapter 2 Measurement Technique and Equipment Setup 22
2.1 Seebeck coefficient measurement 22
2.2 Electrical resistivity measurement 24
2.3 Thermal conductivity measurement 24
2.4 Hall effect measurement 25
2.5 Nernst-Ettingshausen effect measurement 26
2.6 Automatic data acquisition process using Labview program 28
2.7 Sample synthesis 31

Chapter 3 Bismuth Telluride Based Nanocomposites 32
3.1 Synthesis and characterization of PbTe nanoparticles (NP) 32
3. 2 Synthesis and TE properties of n-type $Bi_2Te_{2.85}Se_{0.15}$ 37
3.3 Synthesis and TE properties of n-type $Bi_2Te_{2.85}Se_{0.15}$/xPbTe nanocomposite (NC) 46
3.4 Synthesis and TE properties of p-type $Bi_{0.4}Sb_{1.6}Te_3$ 52
3.5 Synthesis and TE properties of p-type $Bi_{0.4}Sb_{1.6}Te_3$/xPbTe nanocomposite (NC) 56
3.6 Summary of the chapter 68

Chapter 4 Unfilled P-type Skutterudite Based Nanocomposite 69
4.1 Experiment 71

4.2 Results 72
4.4 Summary of the chapter 80

Chapter 5 High Temperature Thermoelectric and Magnetic Properties of P-type Yb filled skutterudite $Yb_xFe_yCo_{4-y}Sb_{12}$ 82
5.1 Experiment 83
5.2 Results and discussion 84
5.3 Summary of the chapter 94

Chapter 6 Thermoelectric Properties and Galvanomagnetic Properties of P-type Yb-filled Skutterudite Nanocomposites with $FeSb_2$ Nanoinclusions 96
6.1 Sample synthesis 97
6.2 Results 99
6.4 Summary of the chapter 115

Chapter 7 Thermoelectric Properties of Double Filled P-type Skutterudite $Yb_yGa_zFe_xCo_{4-x}Sb_{12}$ 116
7.1 Sample synthesis 118
7.2 Results 119
7.3 Discussion 124
7.4 Summary of the chapter 128

Chapter 8 Conclusions and Future Work 130

Bibliography 134

LIST OF TABLES

Table 1 Scattering parameter s and temperature dependence of carrier mobility for different scattering mechanisms. 11

Table 2 Sample identification and some room temperature physical properties of $Bi_{0.4}Sb_{1.6}Te_3$/xPbTe NC 57

Table 3 Some physical properties of Yb filled Fe compensated p-type skutterudite sample $Yb_xFe_yCo_{4-y}Sb_{12}$ at room temperature. 85

Table 4 Some physical properties of Yb filled Fe compensated p-type skutterudite sample $Yb_xFe_yCo_{4-y}Sb_{12}$ at room temperature. The lower and upper boundaries of estimated number of carrier/formula unit are calculated assuming a variant Yb valence of +2 and +3. Minus sign in estimated number of carrier/formula unit indicates the major carrier is electron. 94

Table 5 Sample ID and nominal chemical composition for $Yb_yFe_xCo_{4-x}Sb_{12}/zFeSb_2$ included in this study. 98

Table 6 Some room temperature physical properties of $Yb_{0.6}Fe_2Co_2Sb_{12}/xFeSb_2$ samples. 107

Table 7 Sample designation of double filled skutterudite $Yb_yGa_zFe_xCo_{4-x}Sb_{12}$..... 118

LIST OF FIGURES

Figure 1 Schematic illustration of the Seebeck voltage induced by the temperature gradient. For interpretation of the references to color in this and all other figures, the reader is referred to the electronic version of this dissertation. 1

Figure 2 Schematic illustration of Peltier effect 2

Figure 3 Themoelectric uni-couple for power generation (a) and cooling (b) 3

Figure 4 Efficiency ϕ_{max} as a function of ZT for an ideal TE power generator operating between a heat source of 600K, 700K, 800K and a sink of 300K. 6

Figure 5 Schematic illustration of the interdepedent relations among the Seebeck coefficient S, electrical conductivity σ, the thermal conductivity κ, and the resulting ZT for insulators, semiconductors and metals. 7

Figure 6 Seebeck coefficient as a function of reduced Fermi energy for different scattering mechanisms. 11

Figure 7 Schematic illustration of different phonon scattering mechanisms as a function of temperature 17

Figure 8 Electronic density of states (DOS) for a bulk 3D crystalline semiconductor, a 2Dquantum well, a 1D nanowire or nanotube, and a 0D quantum dot[13] 18

Figure 9 Milestones of ZT in the history of thermoelectrics. 1. $CsBi_4Te_6$;[28, 29] 2. Bi_2Te_3;[30-35] 3. PbTe;[36] 4. Zn_4Sb_3;[37] 5. $Yb_{0.2}Co_4Sb_{12}$;[38] 6. $CeFe_4Sb_{12}$;[39] 7. MM/DDFe_4Sb_{12};[40, 41] 8. SiGe;[42] 9. $Yb_{14}MnSb_{11}$;[9] 10. $Yb_xGa_{8-x}Ga_{16}Ge_{30}$ (clatharates);[43] 11. $Hf_{0.6}Zr_{0.4}NiSn_{0.98}Sb_{0.02}$ (half-Heusler);[44] 12. $Ba_{0.08}La_{0.05}Yb_{0.04}Co_4Sb_{12}$ (triple filled skutterudite);[22] 13. $NaPb_{20}SbTe_{22}$ (SALT);[45] 14. $AgPb_{18+x}SbTe_{20}$ (LAST);[23] 15. $Ag(PbSn)_mSbTe_{2+m}$ (LASTT);[24] 16. $AgSbTe_2$-GeTe (TAGS);[46] 17. PbTe-PbSe;[25] 18. Tl-PbTe.[26] 20

Figure 10 Photograph of the flow cryostat used to measure the low temperature transport properties. 22

Figure 11 Schematic illustration of sample setup for low temperature transport properties measurement 23

Figure 12 Hall coefficient measurement setup and wiring on a standard sample puck for Quantum Design Versalab system. 25

Figure 13 (a) Schematic illustration of the Nernst effect and (b) the sample setup for measurement. 27

Figure 14 Schematic illustration of the Nernst field under typical charge carrier scattering mechanisms. 28

Figure 15 Screenshot of the labview based automatic data acquisition program. 29

Figure 16 Flow chart of the labview based automatic data acquisition program 30

Figure 17 X-ray diffraction of PbTe NPs. 33

Figure 18 TEM image of PbTe NPs. We estimate the particle size to be about 13nm 34

Figure 19 IR spectroscopy of PbTe NPs sintered at 350°C (a) and 410°C (b) in inert gas environment for two hours. 35

Figure 20 X-ray diffraction shows that PbTe NPs heated at 410°C for 2 hours still retain the altaite phase (the fine lines shown at the bottom is the reference) with no impurity phase. The crystallite size is estimated to be about 17-22nm using Scherrer formula. 36

Figure 21 Seebeck coefficients as a function of temperature for $Bi_2Te_{2.85}Se_{0.15}$ annealed at different temperatures. 39

Figure 22 Temperature dependence of electrical resistivity for $Bi_2Te_{2.85}Se_{0.15}$ annealed at different temperatures. 40

Figure 23 Lattice thermal conductivity as a function of temperature for $Bi_2Te_{2.85}Se_{0.15}$ annealed at different temperatures. 41

Figure 24 Dimensionless FOM ZT as a function of temperature 42

Figure 25 Carrier concentration as a function of temperature for samples annealed at different temperatures. 43

Figure 26 Pisarenko relation (the room temperature Seebeck coefficient as a function of carrier concentration) for samples annealed at different temperatures. 44

Figure 27 Room temperature *ZT* as a function of annealing temperature. 45

Figure 28 Hall coefficient as a function of temperature for $Bi_2Te_{2.85}Se_{0.15}$/PbTe NCs..... 47

Figure 29 Thermopower as a function of temperature for $Bi_2Te_{2.85}Se_{0.15}$/PbTe NCs 48

Figure 30 Electrical resistivity as a function of temperature $Bi_2Te_{2.85}Se_{0.15}$/PbTe NCs 49

Figure 31 Power factor as a function of temperature $Bi_2Te_{2.85}Se_{0.15}$/PbTe NCs..... 50

Figure 32 Thermal conductivity as a function of temperature for $Bi_2Te_{2.85}Se_{0.15}$/PbTe NCs 51

Figure 33 *ZT* as a function of temperature for $Bi_2Te_{2.85}Se_{0.15}$/PbTe NCs 51

Figure 34 Seebeck coefficient and electrical resistivity as a function of temperature for $Bi_{0.4}Sb_{1.6}Te_3$ hot pressed at 350°C, 380°C and 410°C..... 52

Figure 35 Power factor as a function of temperature for $Bi_{0.4}Sb_{1.6}Te_3$ hot pressed at 350°C, 380°C and 410°C..... 53

Figure 36 Carrier concentration as a function of temperature for $Bi_{0.4}Sb_{1.6}Te_3$ hot pressed at 350°C, 380°C and 410°C 54

Figure 37 Carrier mobility as a function of temperature for $Bi_{0.4}Sb_{1.6}Te_3$ hot pressed at 350°C, 380°C and 410°C..... 55

Figure 38 Thermal conductivity as a function of temperature for $Bi_{0.4}Sb_{1.6}Te_3$ hot pressed at 350°C, 380°C and 410°C 55

Figure 39 *ZT* as a function of temperature for $Bi_{0.4}Sb_{1.6}Te_3$ hot pressed at 350°C, 380°C and 410°C..... 56

Figure 40 IR spectroscopy of hydrazine PbTe NPs with oleate ligands, hydrazine treated PbTe NPs and thermal treated PbTe NPs. 58

Figure 41 TGA of oleate capped PbTe NPs heat treated under N_2 atmosphere 59

Figure 42 PXRD patterns of NCs with 1wt% and 10wt% PbTe NPs loading. Asterisk indicates the PbTe impurity phase..... 60

Figure 43 TEM images of PbTe NPs and NCs with 1 %, 0.5 % and 0.1 wt% discrete PbTe NPs inside the $Bi_{0.4}Sb_{1.6}Te_3$ matrix 61

Figure 44 Seebeck coefficient, electrical resistivity and power factor as a function of temperature for $Bi_{0.4}Sb_{1.6}Te_3$/xPbTe NC 62

Figure 45 Thermal conductivity as a function of temperature for $Bi_{0.4}Sb_{1.6}Te_3$/xPbTe NC. The inset shows the lattice thermal conductivity as a function of temperature..... 63

Figure 46 *ZT* as a function of temperature for $Bi_{0.4}Sb_{1.6}Te_3$/xPbTe NC. 65

Figure 47 Temperature dependence of carrier concentration for $Bi_{0.4}Sb_{1.6}Te_3$/xPbTe NC..... 66

Figure 48 Pisarenko relation of NCs. The fitted line is constructed as an aid to the eye. All matrix bismuth antimony telluride of various carrier concentrations were synthesized in our lab..... 67

Figure 49 Unit cell of a filled skutterudite. *R*: filler atom, *M*: transitional metal, *A*: pnicogen atom..... 70

Figure 50 X-ray diffraction patterns of samples x=0, 0.05, 0.1, 0.2 and control sample $Co_{0.75}Fe_{0.25}Sb_3$ 72

Figure 51 High resolution FESEM images on the fractured surface of nanocomposite samples $Co_{0.9}Fe_{0.1+x}Sb_{3+2x}$ and control sample $Co_{0.75}Fe_{0.25}Sb_3$. (a) x=0.05, the inset image zooms in the circled area to reveal the nanoscopic feature; (b) x=0.1; (c) x=0.2; (d) $Co_{0.75}Fe_{0.25}Sb_3$. 73

Figure 52 Seebeck coefficient as a function of temperature. Ref data are excerpted from reference.[87] 74

Figure 53 Electrical resistivity as a function of temperature 75

Figure 54 Temperature dependence of the power factor 76

Figure 55 Thermal conductivity as a function of temperature..... 77

Figure 56 *ZT* as a function of temperature..... 78

Figure 57 Lattice constant with respect to the Fe/metal ratio. The square at x=0 on the abscissa corresponds to $CoSb_3$ with a lattice constant of 9.0385Å[47]..... 79

Figure 58 Seebeck coefficient as a function of hole concentration. Reference data are from Reference [88] on $Fe_xCo_{4-x}Sb_{12}$. The fitted line is calculated based on the reference. 80

Figure 59 X-ray diffraction patterns for all samples. (a) x=0.4; (b) x=0.6; (c) x=0.8; (d) x=1 . 84

Figure 61 Temperature dependence of Seebeck coefficient. Ref data are the Seebeck coefficients of $YbFe_4Sb_{12}$ measured by Kuznetsov et al[91]..... 86

Figure 62 Electrical resistivity as a function of temperature. Ref data are $YbFe_4Sb_{12}$ measured by Kuznetsov et al[91] 87

Figure 63 Power factors as a function of temperature. Ref1 are data calculated based on $YbFe_4Sb_{12}$ measured by Kuznetsov et al[91]. Ref2 is the power factor for $Ce_{0.9}Fe_{3.5}Co_{0.5}Sb_{12}$ synthesized by us as a control sample. 88

Figure 64 Thermal conductivity as a function of temperature. The inset graph shows the lattice thermal conductivity. 1/T relation is plotted as an aid to understand the graph. 89

Figure 65 TE dimensionless figure of merit *ZT* as a function of temperature. Ref1 is the estimated highest ZT of $YbFe_4Sb_{12}$ by Kuznetsov et al[91]. Ref2 ($Yb_{0.8}Fe_4Sb_{12}$) and Ref3 ($Yb_{0.5}Fe_2Co_2Sb_{12}$) are near room temperature *ZT* reported by Bauer et al[94]. 90

Figure 66 Magnetization of $Yb_xFe_yCo_{4-y}Sb_{12}$ for sample x=0.4, x=0.6, x=0.8 and x=1 at 60K, 80K, 100K, 150K, 200K, 250K and 300K..... 91

Figure 67 χT vs T 93

Figure 68 $1/(\chi - \chi_0)$ vs T..... 93

Figure 69 X-ray diffraction of $Yb_{0.6}Fe_2Co_2Sb_{12}/zFeSb_2$ (a) 12.12 0.6R 0.2FS2 (b) 12.11 0.6R 0.1FS2 (c) 12.10 0.6R 0.05FS2 (d) 12.5 0.6R. Trace antimony was also observed in (a) 99

Figure 70 Zoomed in x-ray diffraction of two $Yb_{0.6}Fe_2Co_2Sb_{12}/0.1FeSb_2$ samples synthesized under the same condition. The major impurity phase is $FeSb_2$ while another closely related $CoSb_2$ and some Sb is also observed. 100

Figure 71 Zoomed in x-ray diffraction of $Yb_{0.4}FeCo_3Sb_{12}/zFeSb_2$ (a) 12.4 0.4R (b) 14.9 0.4R $0.1FS_2$ (c) 14.18 0.4R0.05FS2 (d) 14.10 0.4R 0.2FS2 (e) 14.11 0.4R 0.3FS2. The expansion of the primary skutterudite peak around 31 degree 2θ indicates the existence of $FeSb_2$. 101

Figure 72 FESEM images on the fractured surface of sample 13.9 0.6R0.05FS2(1) which demonstrate the existence of $FeSb_2$ nanoparticle. Images from (a) to (d) are in increasing magnification. 102

Figure 73 Power factors of nanocomposite samples and control samples as a function of temperature. The samples are grouped according to the Yb filling ratio "y" (a) y=0.4; (b) y=0.5; (c) y=0.6; (d) y=0.7; (e) y=0.8; (f) y=0.9; (g) y=1. Generally, nanocomposite samples could exhibit enhanced power factors when $y \leqslant 0.7$ as shown from (a) to (d). Once y>0.7, most nanocomposite samples show comparable or smaller power factors compared to control samples as shown from (e) to (g). .. 106

Figure 74 Seebeck coefficient and electronic resistivity as a function of temperature for $Yb_{0.6}Fe_2Co_2Sb_{12}/xFeSb_2$ 107

Figure 75 Temperature dependence of thermal conductivity for $Yb_{0.6}Fe_2Co_2Sb_{12}/xFeSb_2$. The inset graph displays the lattice thermal conductivity. 109

Figure 76 *ZT* as a function of temperature for $Yb_{0.6}Fe_2Co_2Sb_{12}/xFeSb_2$. 110

Figure 77 Pisarenko relation of nanocomposites and regular skutterudite samples at room temperature. Blue diamond (skutterudite) points represent regular skutterudite samples of various carrier concentrations prepared in our lab. The fit line serves as an aid to the eye. 111

Figure 78 DOS effective mass m^* and carrier scattering parameter s as a function of reduced Fermi energy E_F. 114

Figure 79 (a) 3D graph of the projected Seebeck coefficient S as a function of electrical resistivity ρ and lattice thermal conductivity κ_l. (b) Cross section of $\kappa_l = 0.2$W/mK from (a) which is used to identify the minimum Seebeck coefficient needed to attain certain ZT. 117

Figure 80 Powder x-ray diffraction patterns of samples included in the study. (a) Y60; (b) Y60G10; (c) Y60G15; (d) Y60G20; (e) Y65. The major peaks of all samples are indexed to the skutterudite phase $CoSb_3$ PDF# 01-073-7899. Trace amount of Sb phase can also be detected in (a) but unidentifiable in the graph. Trace amount of Yb can be found in (b), (c), and (d) and are labeled in the graph accordingly. 119

Figure 81 Lattice constant as a function of Ga filling fraction. 120

Figure 82 Temperature dependence of the Seebeck coefficient and the electrical resistivity. 121

Figure 82 Power factor as a function of temperature 122

Figure 83 Total thermal conductivity and lattice thermal conductivity as a function of temperature. 123

Figure 84 *ZT* as a function of temperature. Ref represents *ZT* of $YbFe_4Sb_{12}$ reported by Kuznetsov and Rowe[91] 124

Figure 85 Pisarenko relation of single filled Yb based p-type skutterudite and Yb Ga double filled skutterudite at 300K. Circles in the figure represent additional Yb filled skutterudite samples. Fit line represents the logarithmic relation expressed by Equation 74 and serves as an aid to the eye. 125

Figure 86 (a) DOS effective mass as a function of Fermi energy E_F at 300K. Circle represents Yb filled skutterudite and serves as supplemental datum. (b) Carrier scattering parameter s as a function of temperature. 127

Figure 87 Carrier concentration as a function of temperature. 128

Chapter 1 Introduction to Thermoelectricity

1.1 The thermoelectric effect

The discovery of the thermoelectric (TE) effect dates back in 1821 when Seebeck reported to the Prussian Academy of Science that he had observed a potential difference by heating the junctions between two dissimilar conductors.[1] The Seebeck coefficient, also known as the thermopower S, is defined as the ratio of potential difference and temperature gradient.

$$S = \lim_{\Delta T \to 0} \frac{\Delta V}{\Delta T} \qquad 1$$

Figure 1 is a schematic explanation for the Seebeck coefficient where carriers with higher kinetic energy on the hot side migrate to the cold side, resulting in a voltage difference. The sign of the Seebeck coefficient is determined by the dominant carrier in the material and it is positive for holes and negative for electrons.

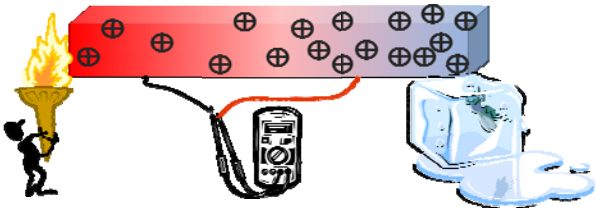

Figure 1 Schematic illustration of the Seebeck voltage induced by the temperature gradient. For interpretation of the references to color in this and all other figures, the reader is referred to the electronic version of this dissertation.

Thirteen years later, the French watchmaker Peltier discovered a second thermoelectric effect (shown in Figure 2): when a current passes through a junction of different metals, there is an absorption or generation of heat, which is distinct from the Joule heating and depends on the

direction of current. The Peltier coefficient Π_{ab} is defined as the rate of reversible heat generation Q over the current I passing through the junction.

$$\Pi_{ab} = \frac{Q}{I} \qquad 2$$

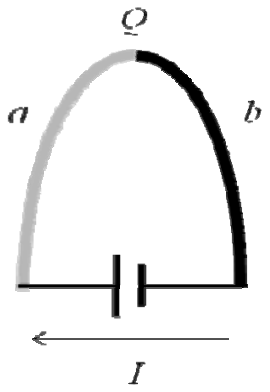

Figure 2 Schematic illustration of Peltier effect

From thermodynamic arguments, Thomson derived the Kelvin relations and discovered the third thermoelectric effect, now termed "Thomson effect". Thomson effect is the heat generation or absorption in a homogeneous conductor besides Joule heating when a current passes through a temperature gradient. The Thomson coefficient γ is defined as:

$$\gamma = \lim_{\Delta T \to 0} \frac{\Delta Q}{I \Delta T} \qquad 3$$

where ΔQ is the rate of reversible heat generation. The importance of Kelvin relations is that it not only connects the Seebeck and Peltier coefficients as shown in Equation 4, but also offers a way of calculating the absolute Seebeck coefficient using Equation 5. Equation 5 also indicates the Seebeck coefficient for all material is zero at zero kelvin.

$$\Pi_{ab} = S_{ab} T \qquad 4$$

$$\frac{dS}{dT}=\frac{\gamma}{T};\quad S=\int_0^T\frac{\gamma}{T}dT \tag{5}$$

1.2 The efficiency for thermoelectric device

The basic thermoelectric device is a uni-couple that consists of a p-type material coupled with an n type material. The device is capable of converting heat into electricity thus working as a power generator [Figure 3(a)], or transfering heat from one end to the other under electric current thus working as a heat pump [Figure 3(b)]. Here we use the generator model to discuss the parameters that govern the efficiency of thermoelectric devices.

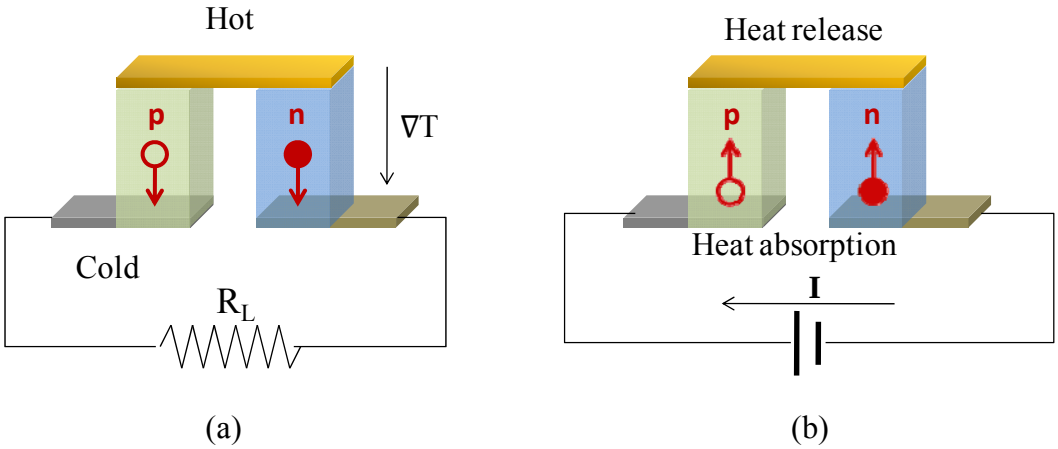

Figure 3 Themoelectric uni-couple for power generation (a) and cooling (b)

The efficiency ϕ is the ratio of power W delivered to the load to the heat supply Q from the source. The current I generated by the thermal electromotive force (EMF) can be expressed as:

$$I=\frac{\left(S_p-S_n\right)\left(T_h-T_c\right)}{R_p+R_n+R_L} \tag{6}$$

where T_h and T_c are temperature of the heat source and sink; and R_p, R_n and R_L represent electrical resistance of the p-type leg, n-type leg and load respectively. The heat supply Q comprises the Peltier effect, the heat conductance and half of the Joule heating that is returned to the source.

$$Q = \left(S_p - S_n\right) I T_h + \left(K_p + K_n\right)\left(T_h - T_c\right) - \frac{1}{2} I^2 \left(R_p + R_n\right) \tag{7}$$

Thus

$$\begin{aligned} \phi = \frac{W}{Q} &= \frac{I^2 R_L}{\left(S_p - S_n\right) I T_h + \left(K_p + K_n\right)\left(T_h - T_c\right) - \frac{1}{2} I^2 \left(R_p + R_n\right)} \\ &= \frac{T_h - T_c}{T_h} \frac{r}{\left(1+r\right) + \frac{\left(1+r\right)^2}{Z_{pn} T_h} - \frac{1}{2}\frac{T_h - T_c}{T_h}} \end{aligned} \tag{8}$$

where $r=R_L/(R_n+R_p)$. It can be seen that ϕ is a function of r. The maximum efficiency can be obtained by setting $d\phi/dr=0$, which yields:

$$r = \sqrt{1 + Z_{pn}\overline{T}}; \quad \overline{T} = \frac{T_h + T_c}{2} \tag{9}$$

So the maximum efficiency $\phi_{\max}$ is:

$$\phi_{\max} = \frac{T_h - T_c}{T_h} \frac{\sqrt{1 + Z_{pn}\overline{T}} - 1}{\sqrt{1 + Z_{pn}\overline{T}} + \frac{T_c}{T_h}} \tag{10}$$

Similarly, the coefficient of performance (*COP*) for thermoelectric refrigeration can be derived as:

$$COP_{\max} = \frac{\overline{T}}{T_h - T_c} \frac{\sqrt{1 + Z_{pn}\overline{T}} - 1}{\sqrt{1 + Z_{pn}\overline{T}} + 1} - \frac{1}{2} \qquad 11$$

The first term in both equations of $\phi_{\max}$ and $COP_{\max}$ is the Carnot efficiency and the second term is related to the material properties Z_{pn}. For fixed T_h and T_c, $\phi_{\max}$ increases with an increasing Z_{pn} towards the Carnot limit. For optimized geometries of the p-type and n-type elements, Z_{pn} is

$$Z_{pn} = \frac{S_{pn}^2}{\left\{ \left(\frac{\kappa_p}{\sigma_p} \right)^{1/2} + \left(\frac{\kappa_n}{\sigma_n} \right)^{1/2} \right\}^2} \qquad 12$$

where κ is the thermal conductivity and σ the electrical conductivity.

The requirement for high conversion efficiency translates to separately seeking p-type or n-type materials with high Seebeck coefficient, electrical conductivity and low thermal conductivity. Therefore we define the thermoelectric figure of merit (FOM) Z for a given material as:

$$Z = \frac{S^2 \sigma}{\kappa} \qquad 13$$

Since Z itself is usually a function of temperature and has dimension of inverse temperature, it is more practical to use the dimensionless FOM ZT in place of Z. For most thermoelectric devices at their operational temperature, the p and n-type elements have nearly identical thermoelectric properties, so Z_{pn} can be approximated by the average of Z_p and Z_n.

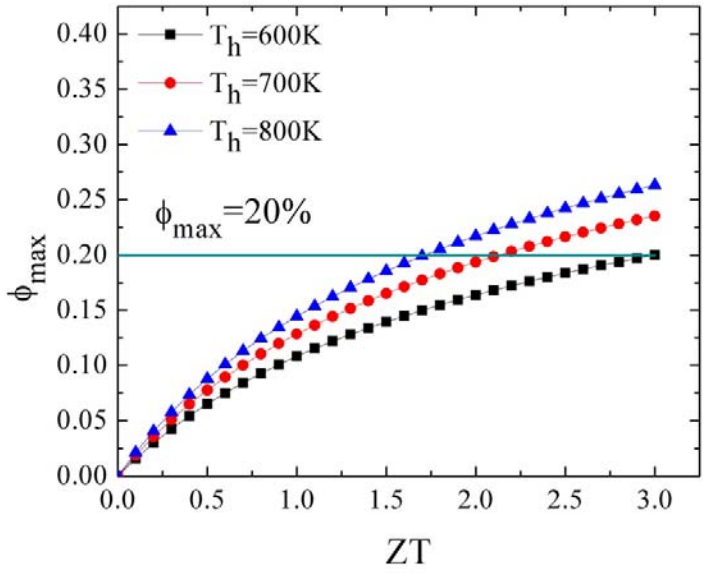

Figure 4 Efficiency ϕ_{max} as a function of ZT for an ideal TE power generator operating between a heat source of 600K, 700K, 800K and a sink of 300K.

Figure 4 plots the maximum power generation efficiency as a function of average *ZT* for a fixed sink temperature of 300K and various heat source temperatures of 600K, 700K and 800K based on Equation 10. In order to gain a conversion efficiency of 20%, thus capable of competing with the conventional heat engines, a *ZT* greater than 2 is needed. Unfortunately, the best known TE materials prior to 1990s have a *ZT* around unity. The definition of FOM is very deceptive as the three seemingly independent physical quantities are intricately related to each other as shown in Figure 5. For example, insulators may have a large Seebeck coefficient and low thermal conductivity, but have low electrical conductivity; on the other hand, metals are good electrical conductors, but they also conduct heat well and suffer a low Seebeck coefficient, typically only a few $\mu V/K$. It is found that semiconductors have the best compromise and tunability among S, σ, and κ in order to yield a high FOM, which explains why most good

thermoelectric materials are heavily doped semiconductors. We will briefly discuss the transport theories in the next sections.

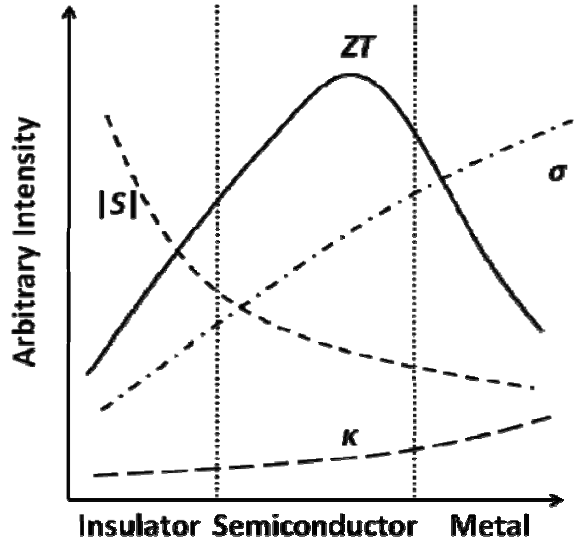

Figure 5 Schematic illustration of the interdepedent relations among the Seebeck coefficient S, electrical conductivity σ, the thermal conductivity κ, and the resulting ZT for insulators, semiconductors and metals.

1.3 Electron transport

The probability of an electron occupying the level of energy E is described by the Fermi-Dirac distribution function $f(E)$:

$$f(E) = \frac{1}{1 + \exp\left(\frac{E - E_F}{kT}\right)} \qquad 14$$

where E_F is the Fermi energy, k the Boltzmann constant. The number of available states at a energy level E is given by the density of states function $g(E)$. For a simple parabolic band, $g(E)$ can be expressed as:

$$g(E) = \frac{4\pi\left(2m^*\right)^{3/2}}{h^3} E^{1/2} \tag{15}$$

where $m^* = \hbar^2 \left(\partial^2 E / \partial k^2\right)^{-1}$ is the effective mass, h is the Planck constant. The carrier concentration is obtained by multiplying *f(E)* and *g(E)* and integrate over the all possible energy levels:

$$n = \int_0^\infty f(E)g(E)dE = \frac{4\pi\left(2m^* kT\right)^{3/2}}{h^3} F_{1/2}(\eta) \tag{16}$$

here $\eta = E_F / kT$, $\varepsilon = E/kT$ is the reduced Fermi energy and kinetic energy of carriers respectively. $F_r(\eta)$ is the Fermi-Dirac integral defined as:

$$F_r(\eta) = \int_0^\infty \varepsilon^r f(\eta) d\eta = \int_0^\infty \frac{\varepsilon^r d\varepsilon}{1 + \exp(\varepsilon - \eta)} \tag{17}$$

The Equation 14 describes the electron distribution under no applied electric field. Suppose an electric field is applied and a steady state is set up. If the field is small, *f(E)* can be replaced by a new distribution function $f_1(E)$ and the rate of change is

$$\frac{df}{dt} = \frac{f_1(E) - f(E)}{\tau} \tag{18}$$

where τ is the relaxation time of the system. Two processes are involved in calculating the electrical conductivity: 1) the electrons will acquire a drift velocity under the electric field ***E*** and 2) the electrons will be scattered by lattice vibrations, other electrons, and crystal imperfections. In the steady state, the two processes are balanced so we have:

$$\left(\frac{df(E)}{dt}\right)_{drift}+\left(\frac{df(E)}{dt}\right)_{scattering}=0 \tag{19}$$

The drift term is:

$$\left(\frac{df(E)}{dt}\right)_{drift}=\left(\frac{df(E)}{dv}\right)\frac{dv}{dt}=-\frac{e\mathbf{E}}{m^*}\frac{df(E)}{dv} \tag{20}$$

and the scattering term is:

$$\left(\frac{df(E)}{dt}\right)_{scattering}=\frac{f_1(E)-f(E)}{\tau} \tag{21}$$

Combining Equation 19-21, we have the new distribution function $f_1(E)$:

$$f_1(E)=f_0(E)+\frac{e\mathbf{E}}{m^*}\tau\frac{df(E)}{dv} \tag{22}$$

The one dimensional current density is:

$$j=-e\int_0^\infty vf_1(E)g(E)dE=-\int_0^\infty\frac{e^2\mathbf{E}}{m^*}\tau v\frac{df(E)}{dv}g(E)dE \tag{23}$$

Hence we obtain the expression for the electrical conductivity σ according to its definition.

$$\sigma=\frac{j}{\mathbf{E}}=\frac{16\sqrt{2}\pi m^{*1/2}e^2}{3h^3}\int_0^\infty\tau(E)E^{3/2}\frac{df(E)}{dE}dE \tag{24}$$

The average energy of electrons in the current is

$$\overline{E}=\frac{\int_0^\infty Ej(E)dE}{\int_0^\infty j(E)dE}=\frac{\int_0^\infty\frac{df(E)}{dE}l(E)E^2dE}{\int_0^\infty\frac{df(E)}{dE}l(E)EdE} \tag{25}$$

where the electron mean free path $l(E)=\tau v$. From the thermodynamic perspective, the Seebeck coefficient is the flow of entropy per passing electron, so

$$
\begin{aligned}
S = \frac{\boldsymbol{S}_{entropy}}{e} &= \frac{1}{e}\left(\frac{\overline{E}}{T} - \frac{E_F}{T}\right) = \frac{k_B}{e}\left(\frac{\overline{E}}{k_B T} - \frac{E_F}{k_B T}\right) \\
&= \frac{k_B}{e}\left(\frac{\int_0^\infty \frac{df(\varepsilon)}{d\varepsilon} l(\varepsilon)\varepsilon^2 d\varepsilon}{\int_0^\infty \frac{df(\varepsilon)}{d\varepsilon} l(\varepsilon)\varepsilon d\varepsilon} - \eta\right) \\
&= \pm\frac{k_B}{e}\left(\frac{(s+2)F_{s+1}(\eta)}{(s+1)F_s(\eta)} - \eta\right)
\end{aligned}
\qquad 26
$$

s is the power for the square of the matrix element of the scattering transition $W(E) \propto E^{-s}$, also referred to as the carrier scattering parameter. Although we use electrons as an example to derive the Seebeck coefficient, the case for holes is identical. The positive sign in Equation 26 represents the case for holes and negative sign for electrons. The above equation is the most general expression for the Seebeck coefficient which is valid for both non-degenerate and degenerate semiconductors and metals. In some texts, $s'=s-1/2$ is used in place of s. This comes from the fact that for simple parabolic bands $g(E) \propto E^{1/2}$, so $\tau(E) \propto W^{-1}(E) g^{-1}(E) = E^{s-1/2}$. We will use the notation of s throughout this dissertation. When this is the case, the carrier mobility has a temperature dependence of $\mu \propto T^{s-3/2}$ for scattering by lattice vibration (thermal fluctuation) and $\mu \propto T^{s-1/2}$ for scattering by ionized and neutral lattice defects. Table 1 lists the values of s for common scattering mechanisms, together with corresponding s' and the temperature dependence of mobility μ. Figure 6 plots the Seebeck coefficient as a function of reduced Fermi energy η for different scattering mechanisms.

Scattering mechanism	s	s'	μ
Phonon	0	-1/2	$\mu \propto T^{-3/2}$
Neutral impurity	1/2	0	$\mu \propto T^{0}$
Ionic impurity	2	3/2	$\mu \propto T^{3/2}$

Table 1 Scattering parameter s and temperature dependence of carrier mobility for different scattering mechanisms.

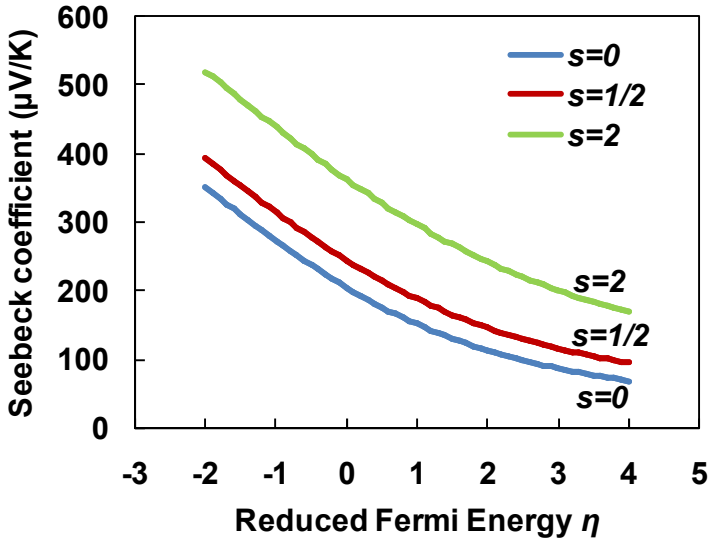

Figure 6 Seebeck coefficient as a function of reduced Fermi energy for different scattering mechanisms.

1.4 Thermal transport

The thermal conductivity κ comprises two parts, the electronic thermal conductivity κ_e and the lattice thermal conductivity κ_l:

$$\kappa = \kappa_e + \kappa_l \tag{27}$$

κ_e is usually calculated by Wiedemann-Franz law $\kappa_e = L\sigma T$, where the general expression for Lorenz number L is given by[1]:

$$L = \frac{(1+s)(3+s)F_s F_{2+s} - (2+s)^2 F_{(1+s)}^2}{(1+s)^2 F_s^2}\left(\frac{k}{e}\right)^2 \quad 28$$

where F and s are Fermi integral and scattering parameters defined in the previous section. For metals and strongly degenerate semiconductors, the Lorenz number takes the value

$$L = \frac{\pi^2}{3}\left(\frac{k}{e}\right)^2 = 2.4453\times10^{-8}\ W\Omega K^{-2} \quad 29$$

For intrinsic semiconductors, the Lorenz number takes the value

$$L = 2\left(\frac{k}{e}\right)^2 = 1.4866\times10^{-8}\ W\Omega K^{-2} \quad 30$$

The Lorenz number of partially degenerate semiconductors falls between the above mentioned two extreme cases and could be calculated using Equation 28, although for a material whose lattice thermal conductivity κ_l is of major importance, assuming $L=2.4453\times10^{-8} W\Omega K^{-2}$ will not incur a huge error.[2]

A special case that should catch one's attention is the bipolar thermal diffusion, in which electrons in the conduction band and holes in the valence band both contribute to the electronic thermal conductivity. In this case, κ_e is not a simple addition of κ_{e1} from electron and κ_{e2} from the hole, but has a more complex form:

$$\kappa_e = \kappa_{e1} + \kappa_{e2} + \left(\frac{k}{e}\right)^2 \frac{\sigma_1\sigma_2 T}{\sigma_1+\sigma_2}\left(4 + \frac{E_G}{kT}\right)^2 \quad 31$$

The additional last term on the right hand side of Equation 31 arises from the transportation of ionization energy of approximately equal number of electrons and holes created at the hot end

and recombined at the cold end. Thus this phenomenon will be most noticeable in intrinsic semiconductors where both electrons and holes have high mobility.[2, 3]

The lattice thermal conductivity κ_l is related to the transport of phonons, which are quanta of the vibrational energy of the lattice analogous to photon. The average number of phonons with energy $\hbar\omega$ is given by:

$$N_0(q) = \frac{1}{\exp\left(\frac{\hbar\omega}{kT}\right) - 1} \tag{32}$$

The total heat current Q due to all modes is:

$$Q = \sum N(q)\hbar\omega v_G(q) \tag{33}$$

where $v_G(q)=d\omega/dq$ is the group velocity of propagation. Similar to the electron transport, the phonon drift under the temperature gradient will be balanced by the phonon scattering so that at equilibrium one has:

$$\left(\frac{\partial N}{\partial t}\right)_{drift} + \left(\frac{\partial N}{\partial t}\right)_{scattering} = 0 \tag{34}$$

where

$$\left(\frac{\partial N}{\partial t}\right)_{drift} = -(v_G \bullet \nabla T)\frac{\partial N}{\partial T} \tag{35}$$

In the relaxation time method, it is assumed that the rate of the scattering process is proportional to the departure of the distribution from the equilibrium so that:

$$\left(\frac{\partial N}{\partial t}\right)_{scattering} = \frac{N_0 - N}{\tau} \tag{36}$$

If we further assume N is not too greatly different from N_0, then $\partial N/\partial T$ in Equation 35 can be replaced by $\partial N_0/\partial T$. Thus we have the following equation for one dimensional case.

$$\left(\frac{\partial N}{\partial t}\right)_{scattering} = \frac{N_0 - N}{\tau} = \left(v_G \bullet \nabla T\right)\frac{\partial N}{\partial T} = v^z{}_G \frac{\partial N_0}{\partial T}\frac{\partial T}{\partial z} \qquad 37$$

The lattice thermal conductivity κ_l is defined as:

$$\kappa_l = -\frac{Q}{\partial T/\partial z} = \sum \hbar\omega v_G^2 \tau \frac{\partial N_0}{\partial T} \qquad 38$$

If we replace the summation by integral over ω and write $(v_G^z)^2 = 1/3(v_G)^2$, we obtain

$$\kappa_l = \frac{1}{3}\int_0^{\omega_{\max}} \hbar\omega v_G^2 \tau f(\omega)\frac{\partial N_0}{\partial T} d\omega \qquad 39$$

where $f(\omega)d\omega$ is the number of phonon modes between ω and $\omega+d\omega$ per unit volume:

$$f(\omega)d\omega = \frac{3\omega^2}{2\pi^2 v^3} d\omega \qquad 40$$

so that Equation 39 transforms into

$$\kappa_l = \frac{1}{2\pi^2 v}\int_0^{\omega_{\max}} \hbar\omega^3 \tau \frac{\left(\hbar\omega/kT^2\right)\exp\left(\hbar\omega/kT\right)}{\left[\exp\left(\hbar\omega/kT\right)-1\right]^2} d\omega \qquad 41$$

If we let $x=\hbar\omega/kT$ and write $\omega_{max}=\omega_D=\theta(k/\hbar)$, where the Debye temperature θ is chosen to be such that there are just $3N$ distinguishable modes:

$$3N = \int_0^{\omega_D} f(\omega) d\omega \qquad 42$$

then

$$\kappa_l = \frac{k}{2\pi^2 v}\left(\frac{k}{\hbar}\right)^3 T^3 \int_0^{\vartheta/T} \tau(x) \frac{x^4 e^x}{\left(e^x - 1\right)^2} dx \tag{43}$$

Equation 43 is the Debye approximation for the lattice thermal conductivity. The heat capacity is

$$C(x) = \frac{3k}{2\pi^2 v^3}\left(\frac{k}{\hbar}\right)^3 T^3 \frac{x^4 e^x}{\left(e^x - 1\right)^2} \tag{44}$$

and the conductivity given by Equation 43 can be simplified as

$$\kappa_l = \frac{1}{3} v^2 \int_0^{\vartheta/T} \tau(x) C(x) dx = \frac{1}{3} v \int_0^{\vartheta/T} l(x) C(x) dx \tag{45}$$

where $l(x)=v\tau(x)$ is the mean free path of the phonon. [3, 4]

Equation 43 is often used to analyze and predict the experimental data. This is done by calculating the relaxation time $\tau(x)$ for various phonon scattering mechanisms $\tau_i(x)$, the inverse of which are additive.

$$\tau^{-1} = \sum_i \tau_i^{-1}(x) \tag{46}$$

For phonon-phonon normal scattering (N-process), the relaxation rate:

$$\tau_N^{-1} = B\omega^a T^b \tag{47}$$

where B is a constant independent of ω and T. a and b are empirical constants for specific groups of elements or crystal structures. The N-processes do not directly contribute to the thermal resistance but have great effect on transferring phonons between different modes.

For phonon-phonon Umklapp scattering (U-process), Slack[5] proposed the following form:

$$\tau_U^{-1} \approx \frac{\hbar\gamma^2}{Mv^2\theta_D}\omega^2 T \exp\left(-\theta_D/3T\right) \quad (48)$$

where γ is the Gruneisen parameter and M the average atomic mass. At sufficiently high temperature, U-processes become the dominant phonon scattering mechanism and κ_l is proportional to $1/T$.

For point defect scattering:

$$\tau_{PD}^{-1} \approx \frac{V}{4\pi v^3}\omega^4 \sum_i f_i \left(\frac{\bar{m} - m_i}{\bar{m}}\right)^2 \quad (49)$$

where V is the volume per atom, m_i is the mass of an atom, f_i the fraction of atoms with mass m_i, and $\bar{m}$ is the average mass of all atoms.

For boundary scattering:

$$\tau_B^{-1} = \frac{v}{d} \quad (50)$$

where d is the grain size for polycrystals or sample size for single crystal. Figure 7 plots the schematic illustration of the temperature dependence of typical phonon scattering mechanisms in polycrystalline semiconductors.

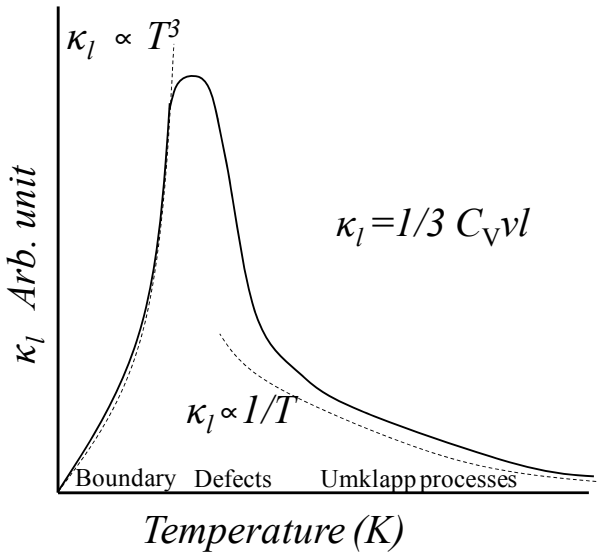

Figure 7 Schematic illustration of different phonon scattering mechanisms as a function of temperature

1.5 The effect of low dimensional materials

The optimization of ZT can be artificially divided into two routes according to its definition: 1) to reduce the lattice thermal conductivity κ_l , 2) to increase the power factor $S^2\sigma$ with the caution that compromises have to be made so that the overall ZT is enhanced. The first route of κ_l reduction appears easier as only one parameter is involved and over the years researchers have discovered a few successful methods to lower κ_l such as increasing the average atomic mass,[6] making alloys and solid solutions,[7, 8] seeking materials with intrinsic complex structures,[9] and creating phonon scattering by inserting foreign atoms into an open void.[10]

However, κ_l cannot be indefinitely reduced as the minimum κ_l is estimated to be 0.1-0.2 W/mK by using $\kappa_l = 1/3Cvl$ where the phonon mean free path l is assumed to be on the order of

interatomic spacing. Thus for even higher *ZT*, it is critical to enhance the power factor portion of the FOM. Traditionally, increasing $S^2\sigma$ relies on properly doping the material so that the Fermi level is positioned in the optimal region to yield the maximum value.[1] The limitation for this method is that 1) the maximum attainable value is very likely pre-set by the nature of the material and 2) it is very hard to independently tune *S* and σ.

In 1993, Hicks and Dresselhaus first predicted theoretically that the ZT in a 2D quantum well structure could be increased by several fold over the same 3D bulk materials, if superlattice multilayers are properly oriented and their size is comparable to the interatomic spacing. This work was soon expanded to quantum wires and quantum dots as they can offer more quantum confinement[11, 12].

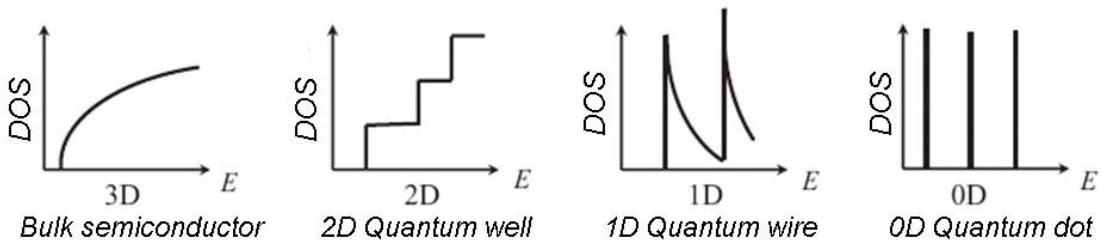

Figure 8 Electronic density of states (DOS) for a bulk 3D crystalline semiconductor, a 2Dquantum well, a 1D nanowire or nanotube, and a 0D quantum dot[13]

The following proof of principle experiments demonstrated that the enhancement of *ZT* in nanostructured materials comes from both the reduction of κ_l and the enhancement of $S^2\sigma$. The reduction of κ_l is not hard to understand as the reduced dimension caps the mean free path *l*. To understand the enhancement of $S^2\sigma$, it is helpful to express the Seebeck coefficient according to the Mott and Jones equation[14]:

$$S = \frac{\pi^2 k^2 T}{3e}\left(\frac{d\ln\sigma(E)}{dE}\right)\Bigg|_{E=E_F} = \frac{\pi^2 k^2 T}{3e}\left(\frac{d\ln g(E)}{dE} + \frac{d\ln v^2(E)}{dE} + \frac{d\ln \tau(E)}{dE}\right)\Bigg|_{E=E_F} \quad 51$$

where v is the average electron drift velocity, and τ is the relaxation time. For free electrons, $g(E) \propto E^{1/2}$, $v^2 \propto E$, and $\tau \propto E^s$. The first term $d\ln g(E)/dE$ suggests that a large thermopower is possible if the Fermi level is positioned near a sharp spike in the density of state (DOS). Theoretical calculation indeed shows that the DOS becomes discontinuous when the dimension of the constituent is reduced as illustrated in Figure 8. This mechanism has been corroborated by the large power factor enhancement in PbTe quantum well structures[15, 16], Si/Ge superlattice[17], PbSeTe based quantum dot superlattice (ZT~1.3-1.6) [18] and Bi_2Te_3/Sb_2Te_3 superlattice (ZT~2.4) [19]. The third term $d\ln\tau(E)/dE$ indicates that it is also possible to enhance the Seebeck coefficient by tweaking the scattering parameter s (also known as the energy filtering effect[20]). In fact, this method has been proposed by Ioffe and his coworkers as a way to search for new TE materials with ionic bonding.[1] Heremans *et al* has demonstrated in PbTe nanostructures[21] that the enhanced Seebeck coefficient is the result of a greater scattering parameter s caused by resonant scattering.

1.6 The state-of-the-art thermoelectric materials

Figure 9 plots the ZT as a function of temperature for selected materials that mark the milestones on the advancement of TE materials. By discovering materials with intrinsic complex structures,[9, 22] utilizing phase decomposition to create imbedded nanostructures,[23, 24] band

structure engineering[25, 26] and advanced materials processing techniques (such as melt spinning[27]), many material systems exhibit a *ZT* above unity and some even get close to 2.

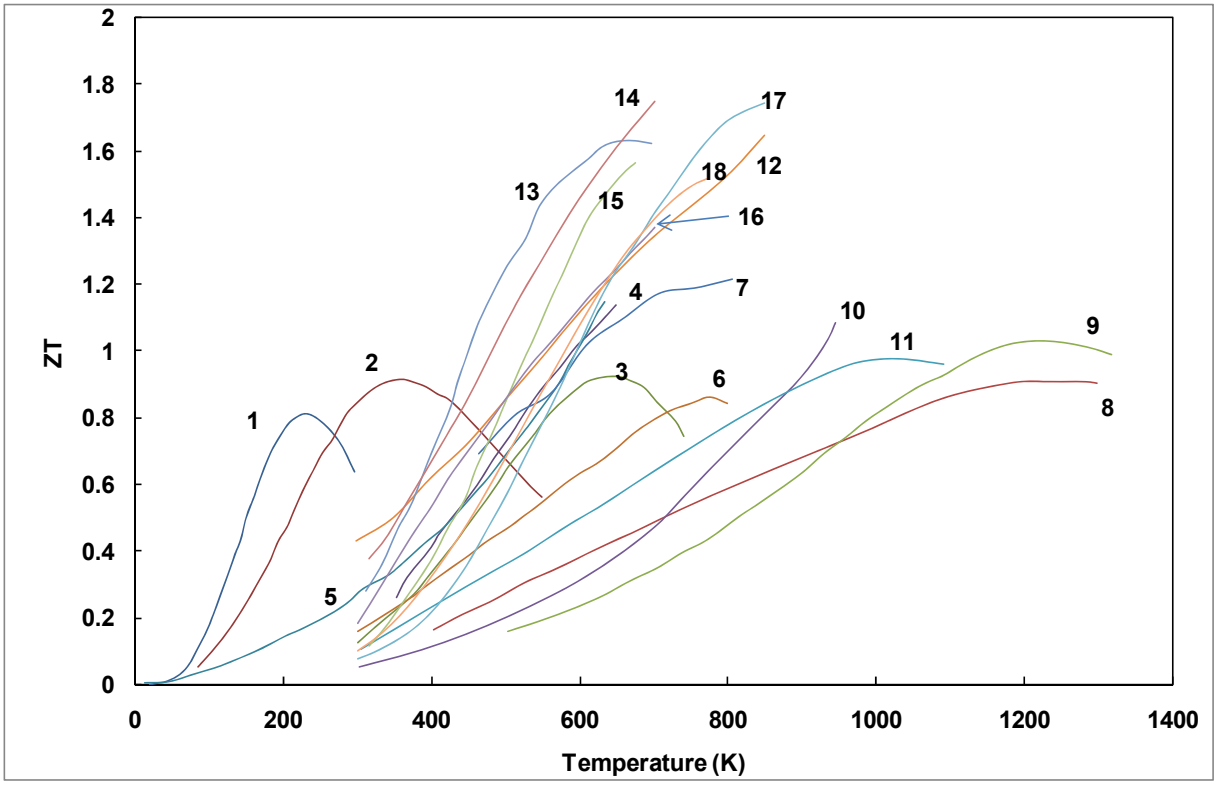

Figure 9 Milestones of ZT in the history of thermoelectrics. 1. $CsBi_4Te_6$;[28, 29] 2. Bi_2Te_3;[30-35] 3. PbTe;[36] 4. Zn_4Sb_3;[37] 5. $Yb_{0.2}Co_4Sb_{12}$;[38] 6. $CeFe_4Sb_{12}$;[39] 7. MM/DDFe_4Sb_{12};[40, 41] 8. SiGe;[42] 9. $Yb_{14}MnSb_{11}$;[9] 10. $Yb_xGa_{8-x}Ga_{16}Ge_{30}$ (clatharates);[43] 11. $Hf_{0.6}Zr_{0.4}NiSn_{0.98}Sb_{0.02}$ (half-Heusler);[44] 12. $Ba_{0.08}La_{0.05}Yb_{0.04}Co_4Sb_{12}$ (triple filled skutterudite);[22] 13. $NaPb_{20}SbTe_{22}$ (SALT);[45] 14. $AgPb_{18+x}SbTe_{20}$ (LAST);[23] 15. $Ag(PbSn)_mSbTe_{2+m}$ (LASTT);[24] 16. $AgSbTe_2$-GeTe (TAGS);[46] 17. PbTe-PbSe;[25] 18. Tl-PbTe.[26]

The pioneering results inspired us to investigate bulk nanocomposite materials that incorporate the relative ease of synthesis with the possible enhancement of TE properties due to the reduced dimension of the nanoparticles. We expect the myriad nanoscopic interfaces

produced by these nanoparticles can effectively scatter the phonons, thus reducing the lattice thermal conductivity. We are also interested in finding out if these nanoparticles can at least partially preserve the feature of DOS as that exhibited by 0D quantum dots or act as an energy filter at the grain boundaries, thus improving the Seebeck coefficient without affecting the electrical conductivity too much. With these hypotheses in mind, we start our exploration to the nanocomposite TE materials.

Chapter 2 Measurement Technique and Equipment Setup

2.1 Seebeck coefficient measurement

The Seebeck coefficient is calculated as the ratio of the potential difference ΔV and temperature difference ΔT across the sample as shown in Equation 52.

$$S = \frac{\Delta V}{\Delta T} \qquad 52$$

For low temperature from 80K to room temperature, this is measured under vacuum in a continuous flow cryostat (see Figure 10) using steady state technique with liquid nitrogen as the refrigerant.

Figure 10 Photograph of the flow cryostat used to measure the low temperature transport properties.

The setup for measuring low temperature Seebeck coefficient is shown in Figure 11. A rectangular parallelepiped shape sample with dimensions of approximately 2.4mm × 2.4mm × 8mm is cut out of the ingot or the consolidated pellet. The sample is usually anchored to a copper base using a conducting silver epoxy. A 800Ω resistor wrapped by copper foil is attached to the top of sample to work as a mini heater and generate the temperature gradient for Seebeck coefficient and thermal conductivity measurement. Two copper-constantan thermocouples are anchored to the middle of the sample to measure the temperature difference. The copper leads also serve to measure the voltage difference at the same time.

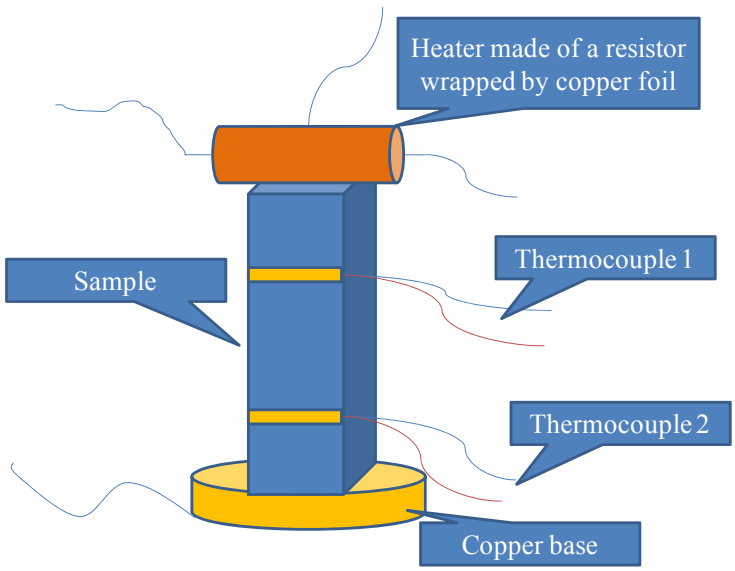

Figure 11 Schematic illustration of sample setup for low temperature transport properties measurement

The high temperature Seebeck coefficient (from room temperature up to 800K) is measured in a commercial equipment ULVAC ZEM-3. The principle of measurement is identical to that of the low temperature except the Seebeck coefficient is calculated as the slope of a set of different ΔV vs ΔT.

2.2 Electrical resistivity measurement

The electrical resistivity ρ is measured by standard four-point method and calculated by using Ohm's law. The resistivity measurement is carried out in parallel with the Seebeck coefficient measurement in the cryostat (for low temperature) and in ZEM3 (for high temperature).

Care must be paid to the influence of Peltier effect on the accuracy of voltage measurement. The as-measured voltage consists of the voltage drop due to the sample resistance and Seebeck voltage, $V_{total}=V_{IR}+V_{Seebeck}=V_{IR}+S\Delta T$. Since TE materials usually have large S, it is possible to incur a large error during the measurement. To minimize the Seebeck induced voltage, the measurement must be completed in short time (usually less than 5 seconds). In addition, it is better to use an AC resistance bridge or the polarized DC current (providing a current from both positive and negative direction) to subtract the $V_{Seebeck}$ part.[47]

$$V_{IR}=\frac{\left(V_{I+}+S\Delta T\right)-\left(V_{I-}+S\Delta T\right)}{2} \tag{53}$$

Another source of error for ρ is from the accuracy of measuring the cross sectional area a and the distance between thermocouple leads l. The error of geometry, however, does not influence ZT as the errors from ρ and κ usually cancel out each other.

2.3 Thermal conductivity measurement

The low temperature thermal conductivity is measured in the cryostat and calculated as:

$$\kappa=K\times\frac{l}{a}=\frac{Ql}{\Delta Ta}=\frac{VI}{\Delta T}\times\frac{l}{a} \tag{54}$$

where K is the thermal conductance, l is the probe separation between the two thermocouples and a is the cross-sectional area. The radiation loss is corrected by subtracting the thermal conductance to the ambient K_{loss} from the total thermal conductance K.

High temperature thermal conductivity is obtained by the laser flash thermal diffusion technique, in which thermal conductivity is related to thermal diffusivity D, isobaric specific heat C_p, density d by $\kappa=dDC_p$. Thermal diffusivity D and specific heat C_p were measured in commercial equipments Netzsch LFA 457 and Netzsch DSC 200F3 respectively. Density d was measured at room temperature by Archimedes method with 200 proof ethanol as the medium.

2.4 Hall effect measurement

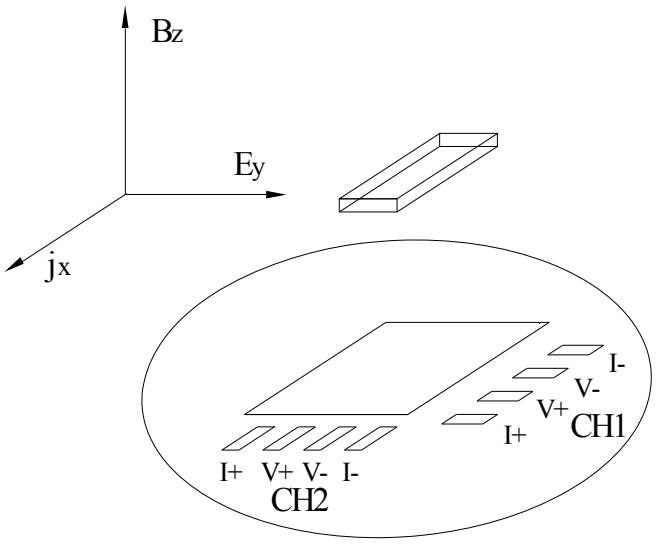

Figure 12 Hall coefficient measurement setup and wiring on a standard sample puck for Quantum Design Versalab system.

Hall coefficients and electrical resistivity from 60K to 400K were carried out using AC current in a varying magnetic field from -3T to 3T in a Quantum Design Versalab system. A thin slab with approximate thickness of 1mm was cut out of the same ingot or sample that is used for low temperature transport measurement. The sample mounting and wiring are illustrated in Figure 12, where the four contacts of CH1 are assigned for measuring the Hall resistance and CH2 is used to measure the electrical resistivity. Since the majority of materials studied in this project are heavily doped semiconductors, we assume a single carrier model with a scattering parameter of unity to calculate the Hall coefficient, hence the carrier concentration given by Equation 55.

$$R_H = \frac{E_y}{j_x B_z} = \frac{V_y t}{I_x B_z} = \frac{R_{xy} t}{B_z} = -\frac{1}{ne} \qquad 55$$

2.5 Nernst-Ettingshausen effect measurement

The Nernst-Ettingshausen effect is another galvanomagnetic effect that provides very important information to the transport properties of TE materials. The Nernst effect [Figure 13(a)] is very analogous to the Hall effect (Figure 12) except that the driving force of charge carriers is the thermal gradient rather than the electric field in the Hall effect. The Nernst coefficient is measured in the cryostat under the magnetic field capable of -2T to 2T. The sample setup is virtually the same as that for low temperature cryostat measurement with a third thermocouple to measure the transverse temperature gradient and transverse voltage incurred by the Nernst effect. The calculation of Nernst coefficient N is given in Equation 56.

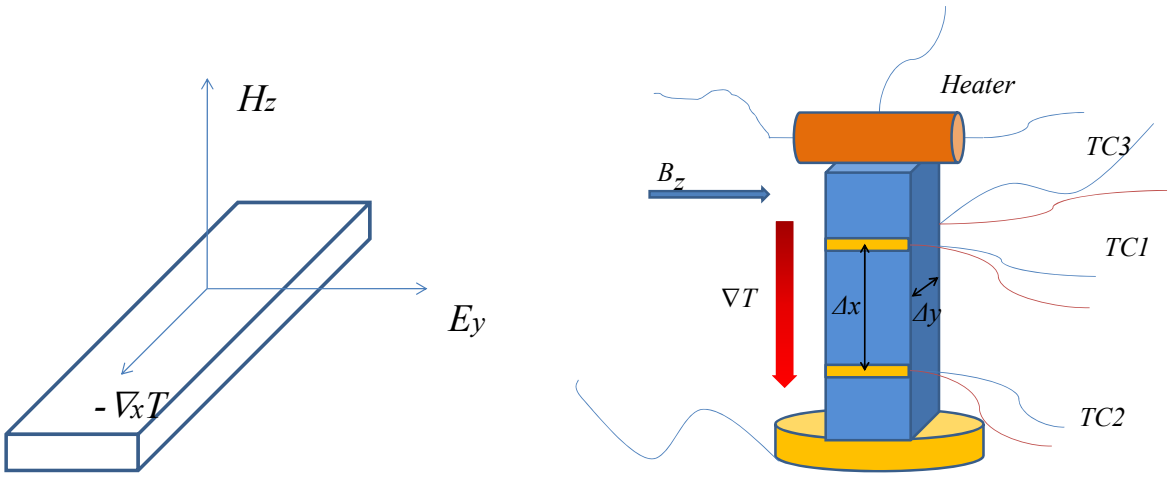

(a) (b)

Figure 13 (a) Schematic illustration of the Nernst effect and (b) the sample setup for measurement.

$$N = -\frac{E_y}{\nabla T_x B_z} \approx -\frac{V_y / \Delta y}{\Delta T / \Delta x}\frac{1}{B_z} = -\frac{V_y}{\Delta T B_z}\frac{\Delta x}{\Delta y} \qquad 56$$

The Nernst field is highly dependent on the scattering mechanisms of the charge carriers.[48] As shown in Chapter 1, the relaxation time $\tau(E) \propto E^{s-1/2} = E^{s'}$. The deflection angle φ depends on the relaxation time τ. If τ is smaller, the arc length of the charge orbit is shorter, hence φ is smaller. Conversely, a larger τ means a larger deflection angle φ. For ionized impurity scattering $s'>0$, τ is larger for more energetic electrons from the hot side than the less energetic electrons from the cold side. Hence $\varphi_1>\varphi_2$, the Nernst field points to the right. This gives a positive Nernst coefficient. Similarly, for acoustic phonon scattering, $s'<0$, τ is larger for the less energetic electrons from the cold side. Hence $\varphi_1<\varphi_2$, the Nernst field points to the left and Nernst coefficient is negative. For neutral impurity scattering, $s'=0$, $\varphi_1=\varphi_2$, Nernst coefficient is zero.

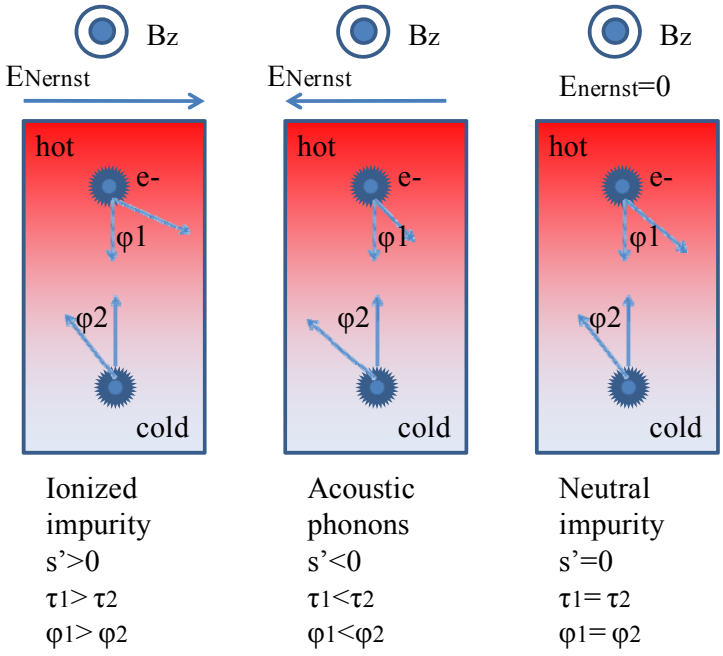

Figure 14 Schematic illustration of the Nernst field under typical charge carrier scattering mechanisms.

Combining the Nernst coefficient N with the Seebeck coefficient S, electrical conductivity σ, and the Hall coefficient R_H, one is able to calculate the DOS effective mass m^* and the carrier scattering parameter s. This method is known as the "method of four coefficients" [21, 48-51], which is well documented in the literature and will be discussed in details in the later chapter.

2.6 Automatic data acquisition process using Labview program

The labview based automatic data acquisition program was developed in our laboratory in the summer of 2009 and has been continually upgraded/expanded to refine the operating parameters and accommodate more testing capabilities. The PC based program controls the temperature controllers, magnets, and meters etc. via National Instruments GPIB card and

Standard Commands for Programmable Instruments (SCPI) language. At the present, the program is able to fully control every aspect of the measurement, perform measurements that otherwise cannot be performed by manual operation, has a user friendly input and output panel, real time data graphing and instant data saving capability. The key operational functions have been compacted to subVIs to improve the readability of the program and facilitate the ease of future expansion. Now, the only things that still need to be done manually are mounting samples in the instruments, turning on the vacuum pump and liquid nitrogen supply. Everything else can be adjusted and controlled by program from any place in the world where there is internet connection. This greatly improves the research productivity in our laboratory from 1 sample/2 days to 2 samples/day or even 3 samples/day if needed. Figure 15 displays the screenshot of the program interface which can measure the Seebeck coefficient, electrical resistivity, thermal conductivity, Hall coefficient and Nernst coefficient simultaneously. Figure 16 displays the flow chart of the program.

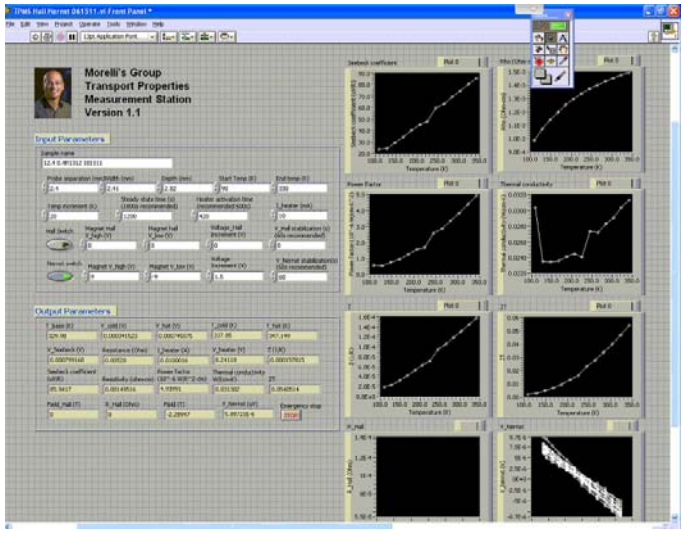

Figure 15 Screenshot of the labview based automatic data acquisition program.

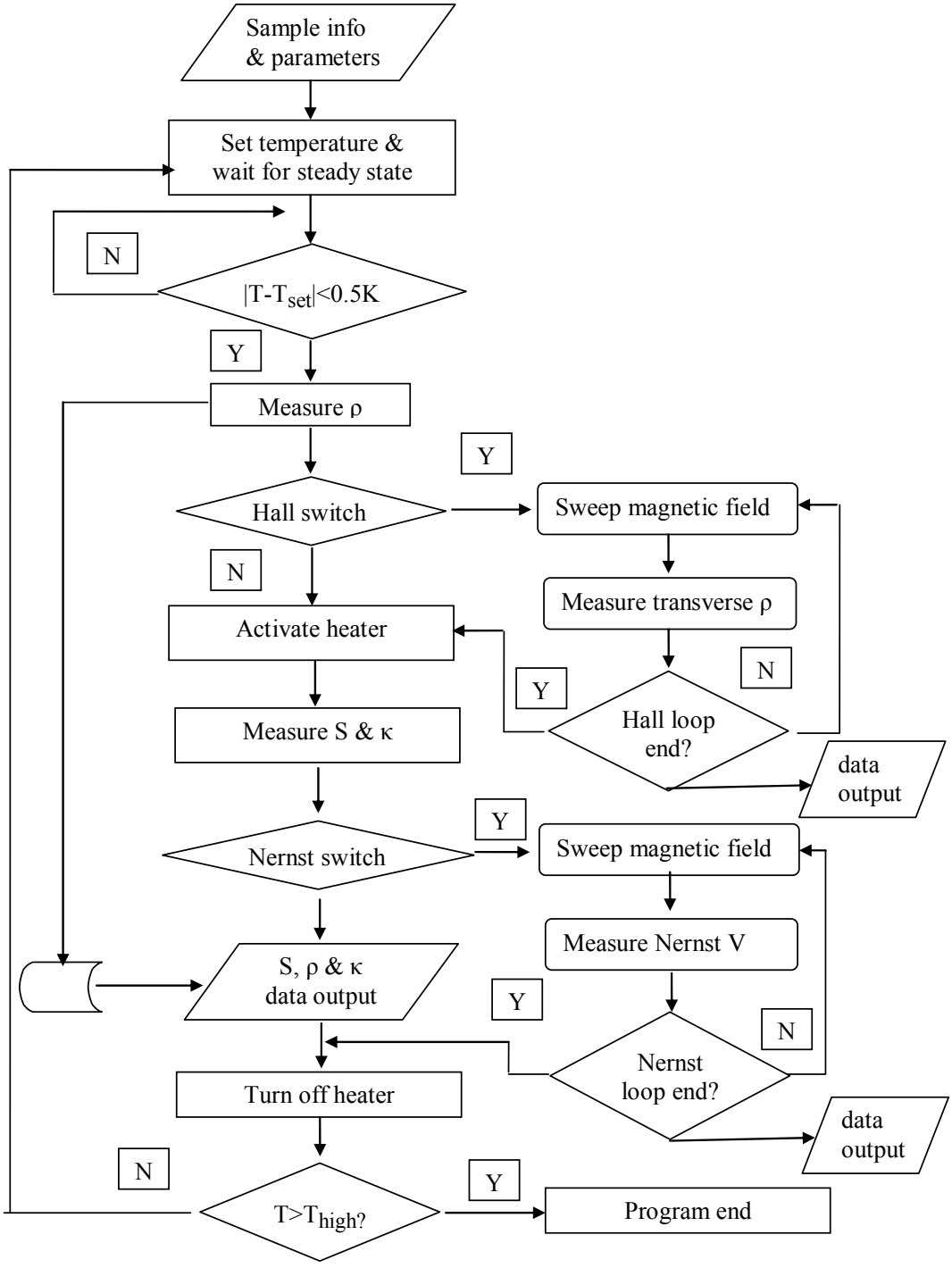

Figure 16 Flow chart of the labview based automatic data acquisition program

2.7 Sample synthesis

Since the methods for synthesizing our samples are different for each material system, details of sample synthesis will be given in the corresponding chapters covering each material.

Chapter 3 Bismuth Telluride Based Nanocomposites

Bismuth telluride based nanocomposites use bismuth telluride and its alloys as the matrix material and lead telluride nanoparticles (NPs) as the nanoinclusions. We select bismuth telluride and lead telluride because both materials are well-known good TE materials in their bulk form with comparable TE properties, thus making them more likely to enhance the overall properties of the composites.[52] As a first step, we prepare our matrix materials and lead telluride nanoparticles separately. N-type $Bi_2Te_{2.85}Se_{0.15}$ and p-type $Bi_{0.4}Sb_{1.6}Te_3$ were prepared and characterized at Michigan State University; PbTe NPs were prepared through wet chemistry method by our collaborators at Wayne State University. The well characterized matrix material and NPs were mixed together using incipient wetness impregnation method, consolidated into the bulk materials and characterized at Michigan State University. The following sections offer detailed descriptions of our study.

3.1 Synthesis and characterization of PbTe nanoparticles (NP)

The PbTe NPs were synthesized by our collaborators Shreyashi Ganguly and Prof. Stephanie Brock at Wayne State University. Discrete PbTe nanoparticles were prepared by combining lead acetate trihydrate ($Pb(OAc)_2 \cdot 3H_2O$) (1.317 g, 3 mmol) with oleic acid (OA) (3 mL, 6 mmol) and 1-octadecene (ODE) (6 mL, 18 mmol) and heating this mixture under inert atmosphere on a Schlenk line at 170 °C for 30 min to obtain a colorless solution [53]. The temperature of the solution was then reduced to 150 °C followed by rapid injection of 3 mL of 1M trioctylphosphine (TOP) tellurium, which was formed by dissolving 1.27 g of Te in 10 mL of

trioctylphosphine solution in a glove box. The resultant solution was left at 150 °C for 5 min and then the reaction was quenched by plunging the flask into a cold-water bath. The NPs were precipitated inside a glove box by adding hexane as the solvent and acetone as the antisolvent, and isolated by centrifugation.

X-ray diffraction (Figure 17) has confirmed the phase purtiy of our PbTe NPs. We applied the Scherrer analysis to estimate the crystallite size to be around 13-19 nm based on the characteristic peak broadening of the NPs, which agrees very well with the NP size given TEM image (Figure 18).

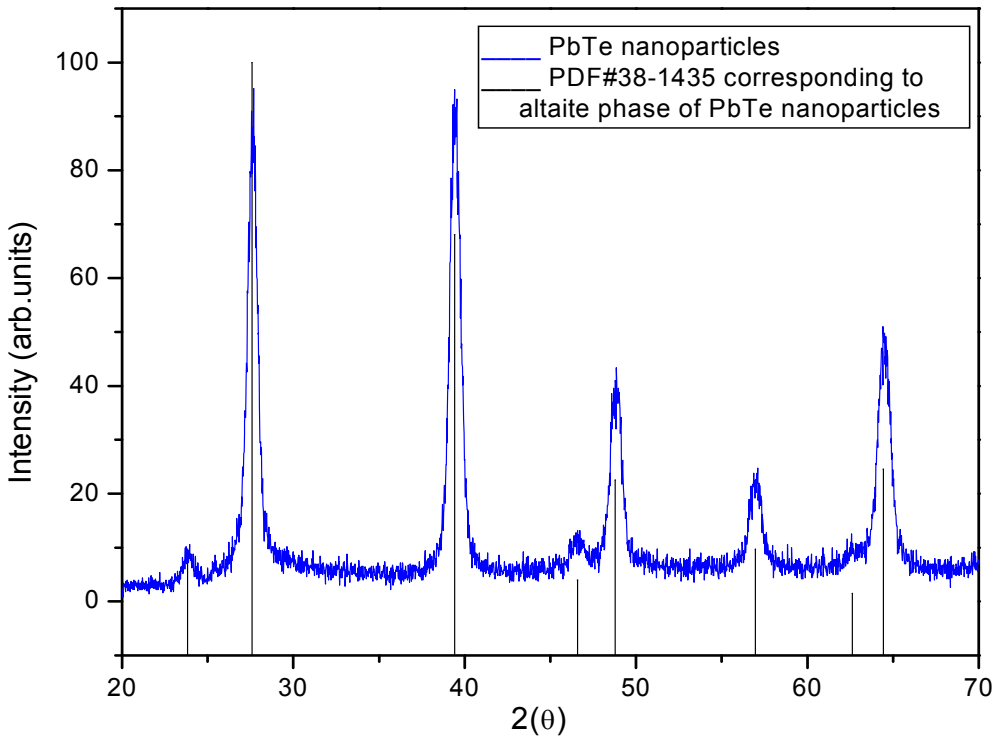

Figure 17 X-ray diffraction of PbTe NPs.

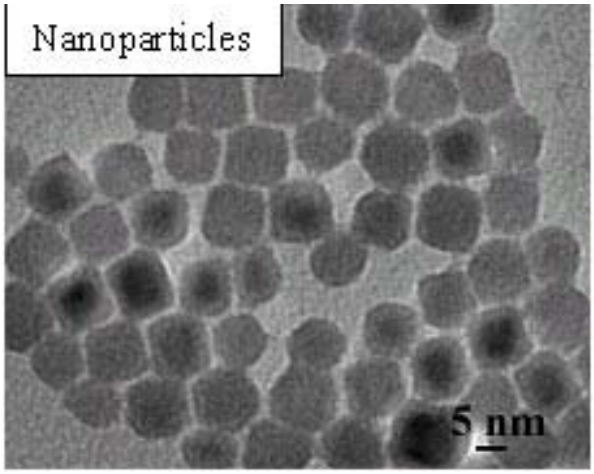

Figure 18 TEM image of PbTe NPs. We estimate the particle size to be about 13nm

Thermogravimetric (TGA) analysis was performed at Wayne State University to test the thermal stability of PbTe NPs. PbTe NPs were heated in a nitrogen protected environment. At 500°C, TGA result shows 15 % weight loss in the PbTe NPs but x-ray diffraction confirms that the characteristic peaks match the diffraction pattern of cubic PbTe (altaite phase), with no other peaks observed. The size of the nanoparticles increased slightly from 16 nm to 24 nm which was estimated by Scherrer formula. At 600C, TGA result shows 25 % weight loss. An extra impurity phase indexed to Pb was also observed along with the PbTe phase. We conclude that the PbTe NPs are thermally stable below 500°C. Such a finding has been confirmed by TEM images on the heated PbTe NPs.

In order to remove the organic ligands that encapsulate the PbTe NPs, we sintered the PbTe NPs in inert gas protected environment for 2 hours at various temperatures below 500°C. IR spectroscopy analysis shows that for sintering temperature of 350°C as shown in Figure 17(a),

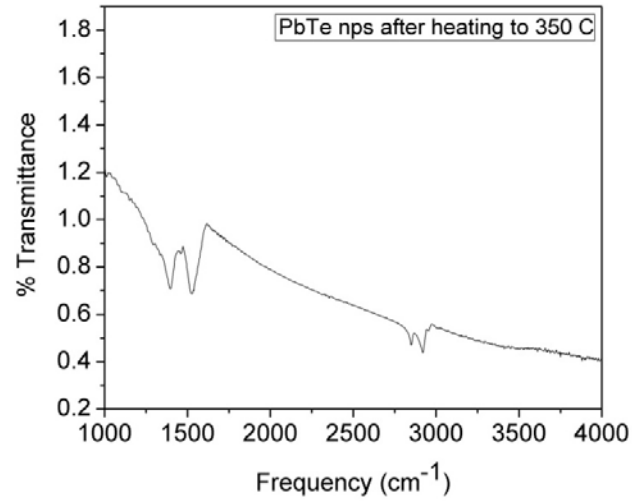

(a)

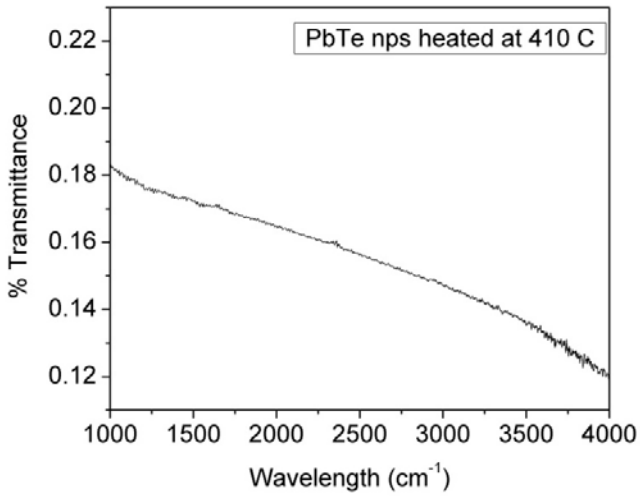

(b)

Figure 19 IR spectroscopy of PbTe NPs sintered at 350°C (a) and 410°C (b) in inert gas environment for two hours.

the organic groups are still present (peak at 1512 cm^{-1} and 1394 cm^{-1} for the symmetric and asymmetric stretching vibrations of COO^- and 2918 cm^{-1} and 2840 cm^{-1} corresponding to

aliphatic –CH stretches). Figure 19(b) shows that for sintering temperature of 410°C, no peak was observed, suggesting that the organic ligands have been completely removed.

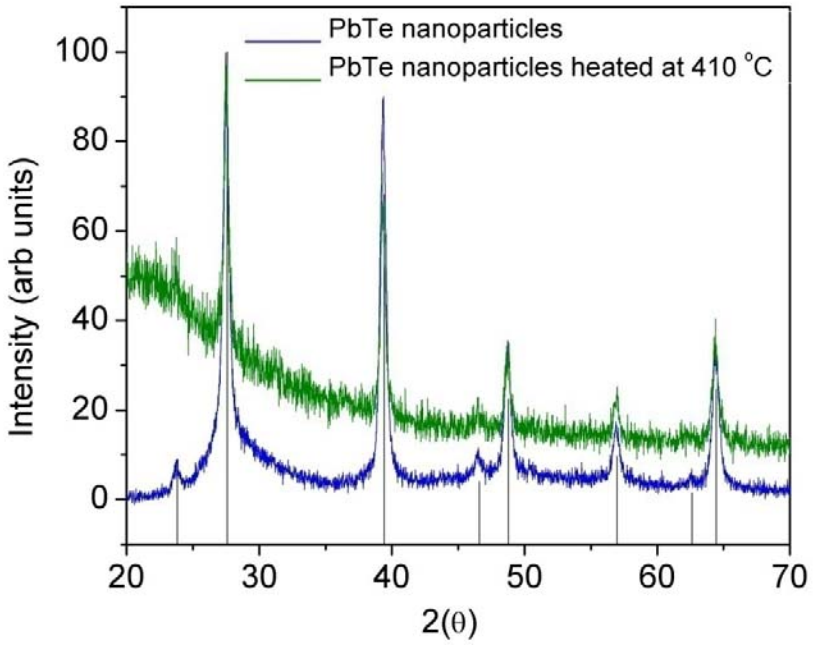

Figure 20 X-ray diffraction shows that PbTe NPs heated at 410°C for 2 hours still retain the altaite phase (the fine lines shown at the bottom is the reference) with no impurity phase. The crystallite size is estimated to be about 17-22nm using Scherrer formula.

In conclusion, we have successfully synthesized PbTe NPs which are thermally stable up to 500°C. X-ray powder diffraction has confirmed the phase purity of the NPs and the particle size is estimated to be about 13nm based on Scherrer analysis and TEM image. IR spectroscopy suggests that heating PbTe NPs at 410°C in inert gas protected environment for two hours is an effective way to remove the surface organic ligands encapsulating the PbTe NPs.

3. 2 Synthesis and TE properties of n-type $Bi_2Te_{2.85}Se_{0.15}$

Bismuth telluride (Bi_2Te_3) has a rhombohedral unit cell of space group $R\bar{3}m$, which can often be envisioned more conveniently as a hexagonal primitive cell with quintuple layers of $-Te^{(1)} - Bi - Te^{(2)} - Bi - Te^{(1)} -$ along c-axis.[47] Bi_2Te_3 can be made both p-type and n-type by alloying with Sb_2Te_3 or Bi_2Se_3 of similar tetradymite structure. Single crystalline Bi_2Te_3 have been grown successfully using the Bridgman method[54], travelling heater method (THM)[32] and zone melting[55]. In spite of the high FOM they present, these single crystals suffer inevitable drawback of poor mechanical properties due to the weak Van der Waals bonding between $Te^{(1)} - Te^{(1)}$ basal planes[56, 57]. Thus polycrystalline Bi_2Te_3 fabricated by powder metallurgy are sought for their improved mechanical properties. However, their thermoelectric properties are very sensitive to processing procedures and have been shown to be quite widely varying.[58-62] This is especially true for n-type $Bi_2(Te, Se)_3$, which may largely be contributed to the electronically active point defects[63] and inhomogeneity of selenium[64].

In order to obtain reproducible TE properties for our n-type $Bi_2Te_{2.85}Se_{0.15}$, we first investigated the influence of annealing on the TE properties of undoped $Bi_2Te_{2.85}Se_{0.15}$. High purity starting materials of Bi, Te, and Se of stoichiometric ratio were charged into a carbon coated quartz ampoule and sealed under vacuum of 10^{-6} Torr. The quartz ampoule was slowly heated to 750°C and held for 12 hours to melt all constituents before being quenched in a water bath. The glossy ingot was milled for 15 min. into fine powders in a Spex mill/mixer.

The milled powders were cold pressed under the load of 1 ton in an 8mm stainless steel die. Cold pressed pellets were re-sealed under vacuum, and annealed at temperatures of 350°C, 400°C, 450°C, 500°C, 520°C, 540°C, 560°C, and 580°C respectively. All samples were annealed for 2 days except that of 450°C sample due to an unexpected fuse break. We estimate the actual time is 2-3 days at 450°C. An individual type-K thermocouple was used to calibrate the temperature inside the furnace. The annealed samples were sliced to rectangular parallelepiped of approximately 3mm × 3mm × 7.5mm for transport property measurement and 1mm × 2.2mm × 7.6mm for Hall measurement. The relative density of our samples is estimated to be about 80% of theoretical density.

X-ray diffraction was performed on the surface perpendicular to the pressing direction. The characteristic peaks match the indices of PDF reference 01-085-0439, which indicates we successfully obtained $Bi_2Te_{2.85}Se_{0.15}$. We also calculated the *F* factor for the degree of orientation and observe no apparent anisotropy.[62]

Figure 21 shows the Seebeck coefficient as a function of temperature. Here for the sake of simplicity in discussion, we arbitrarily divide the annealed samples into two categories: samples annealed at 520°C and above are referred to as high temperature group while those annealed at 500°C and below are referred to as low temperature group. As shown in Figure 21, the Seebeck coefficient for as-pressed unannealed sample is slightly positive, which implies the actual chemical composition is Bi rich and falls in the p-type region. Upon annealing, all samples were converted to n-type and Seebeck coefficients generally become more negative with increasing annealing temperatures. For samples annealed at high temperatures (520°C and above), all Seebeck coefficients achieve their negative peaks below room temperature and then

rise with increasing temperature. The marginal effect of annealing on maxima is reduced at higher temperature with the exception of the sample annealed at 580°C, which is only 5°C below the melting point.

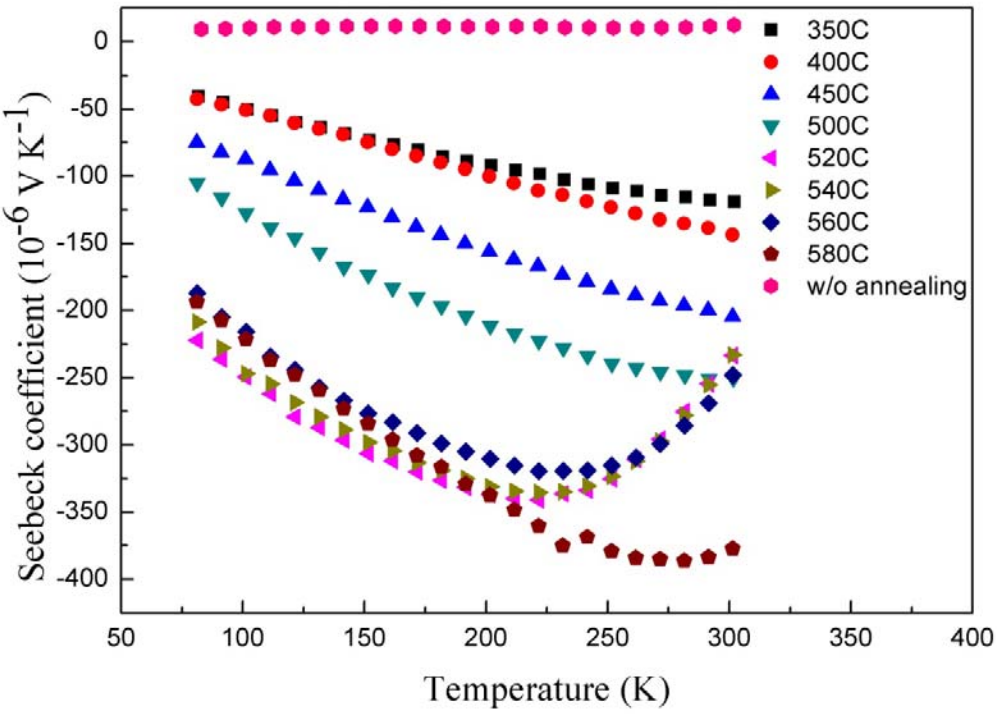

Figure 21 Seebeck coefficients as a function of temperature for $Bi_2Te_{2.85}Se_{0.15}$ annealed at different temperatures.

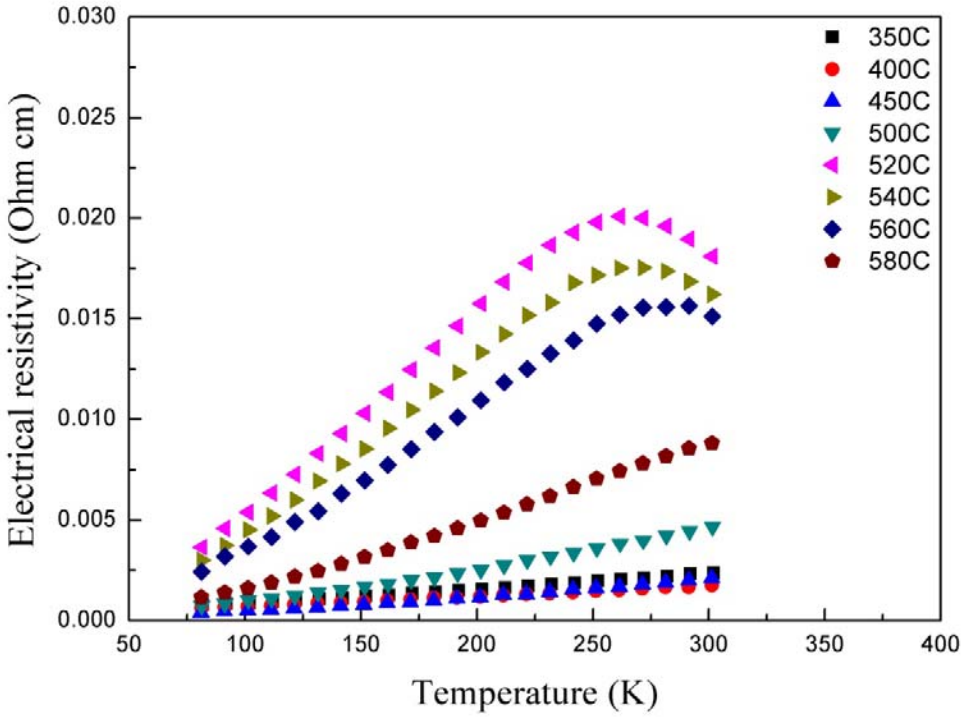

Figure 22 Temperature dependence of electrical resistivity for $Bi_2Te_{2.85}Se_{0.15}$ annealed at different temperatures.

Figure 22 reveals the temperature dependence of electrical resistivity. Samples annealed at lower temperatures (500°C and below) have a smaller resistivity compared to that of the higher temperature group. Increasing the annealing temperature increases the resistivity in general. Resistivity for samples annealed at higher temperature region, on the contrary shows a decreasing trend and its peak shifts to higher temperature as annealing temperature increases with the sample annealed at 520°C on top of all the other samples. The emergence of the resistivity peaks indicates the loss of selenium.

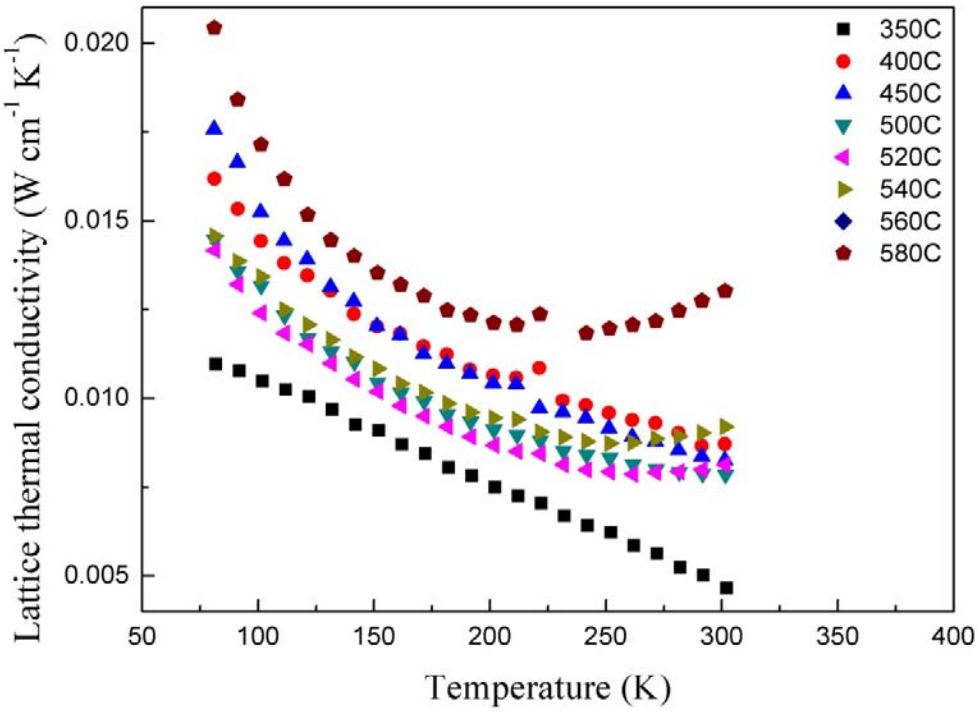

Figure 23 Lattice thermal conductivity as a function of temperature for $Bi_2Te_{2.85}Se_{0.15}$ annealed at different temperatures.

Figure 23 shows the lattice thermal conductivity as a function of temperature. The electronic thermal conductivity has been subtracted by Wiedemann-Franz Law. Apart from samples annealed at the highest and lowest temperatures, all samples have similar values with a difference less than 25% at room temperature. The deviation for these samples can be attributed to the difference in porosity and measurement error. The large separation for samples annealed at both ends can be understood by considering the content and homogeneity of Bi_2Se_3 as a solid solution.

Figure 24 is the temperature dependence of dimensionless FOM ZT. The sample annealed at 450C has the highest ZT=0.51 at 300K and has not reached its full potential due to the limit of our measurement capability.

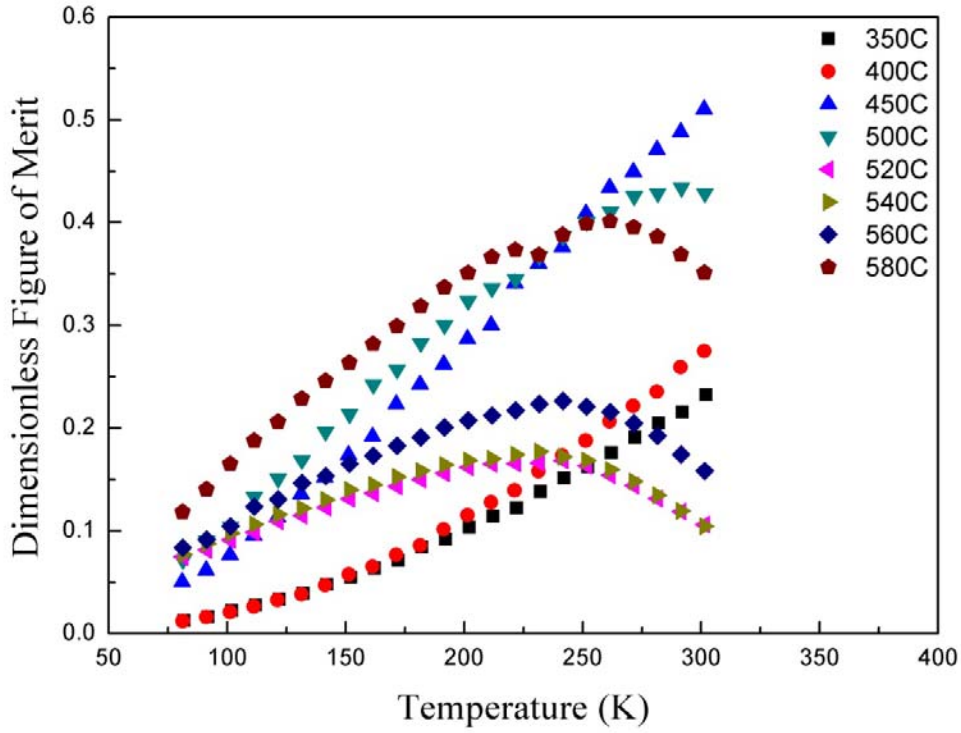

Figure 24 Dimensionless FOM ZT as a function of temperature

For bismuth telluride, the transport properties are very sensitive to the carrier concentration which is largely influenced by electronically active point defects and stoichiometry. The chalcogen elements Te and Se can segregate along the grain boundaries during solidification [64, 65]. The deficiency of chalcogen makes the actual stoichiometry Bi rich, which results in a p-type material. Upon annealing, segregated Se and Te are re-introduced into the material where most Se replaces $Te^{(2)}$ because of its higher diffusion coefficient and larger electronegativity.

This process converts the material to n-type. When the annealing temperature is high, chalcogens can evaporate and leave behind electronically active antisite defects and vacancies [66, 67]:

$$Bi_2Te_3 = 2Bi_{Te}^{/} + 2V_{Bi}^{///} + V_{Te}^{\bullet\bullet} + 3/2Te_2(g) + 8h^{\bullet} \quad 57$$

$$3Bi_2Se_3 = 4Bi_{Bi}^{\times} + 2Bi_{Se}^{/} + 2V_{Bi}^{1.5/} + 7V_{Se}^{\bullet} + 9/2Se_2(g) + 2e^{/} \quad 58$$

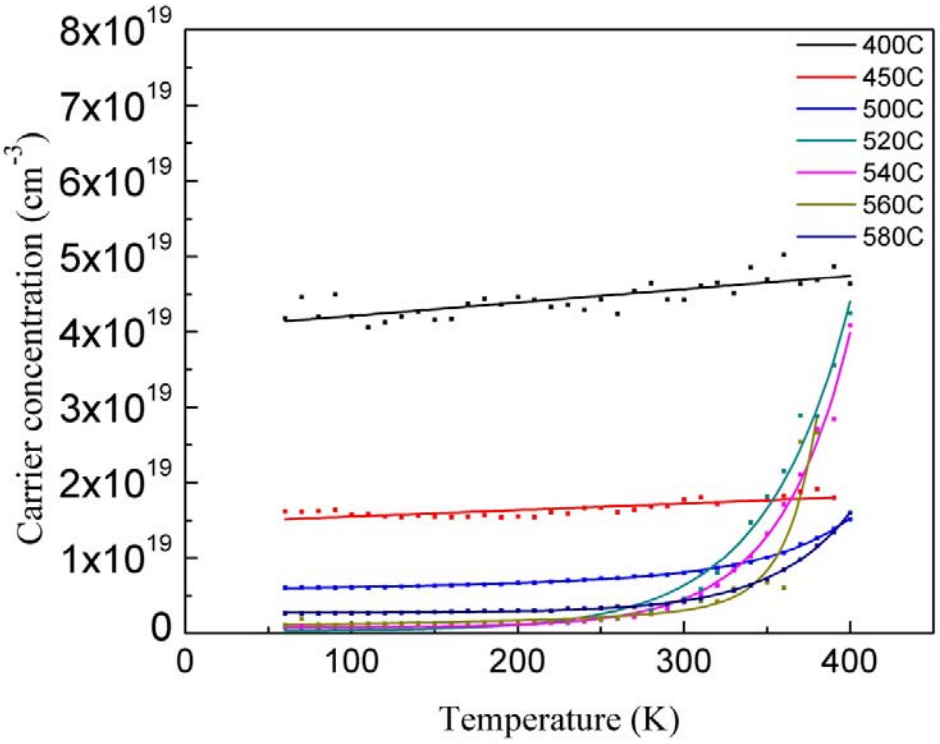

Figure 25 Carrier concentration as a function of temperature for samples annealed at different temperatures.

We believe the process described by Equation 57 of major importance because of the abundance of tellurium and a stronger bond between Bi-Se$^{(2)}$ [68]. The holes generated by $Bi_{Te}^{/}$ and $V_{Bi}^{///}$ reduce the carrier concentration through compensation as illustrated in Figure 25. As

we increase the annealing temperature, the number of charge carriers is reduced and we start to observe the advent of extrinsic to intrinsic conversion in 500°C annealed sample. It is worth noticing that for samples annealed above 520°C, the carrier concentration increases slightly in the extrinsic region which suggests larger amount of Se loss may contribute some extra electrons as described by Equation 58.

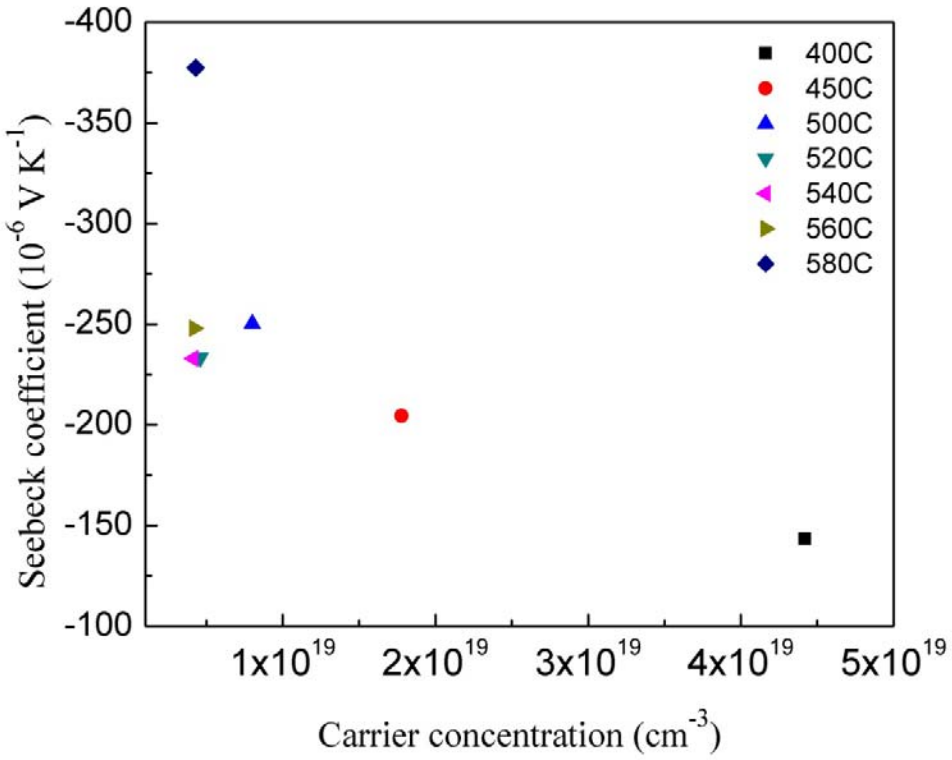

Figure 26 Pisarenko relation (the room temperature Seebeck coefficient as a function of carrier concentration) for samples annealed at different temperatures.

Figure 26 is the so-called Pisarenko relation of our samples, depicting the relation between Seebeck coefficient and electron concentration at room temperature. As annealing temperature is increased, the carrier concentration decreases; the absolute value of Seebeck

coefficient increases as a result until it hits the extrinsic-intrinsic border where it starts to drop off.

In order to seek the optimal temperature range for annealing, we plot the room temperature *ZT* as a function of annealing temperature as shown in Figure 27. We find the annealing temperature in the vicinity of 440°C offers the best TE performance at 300K.

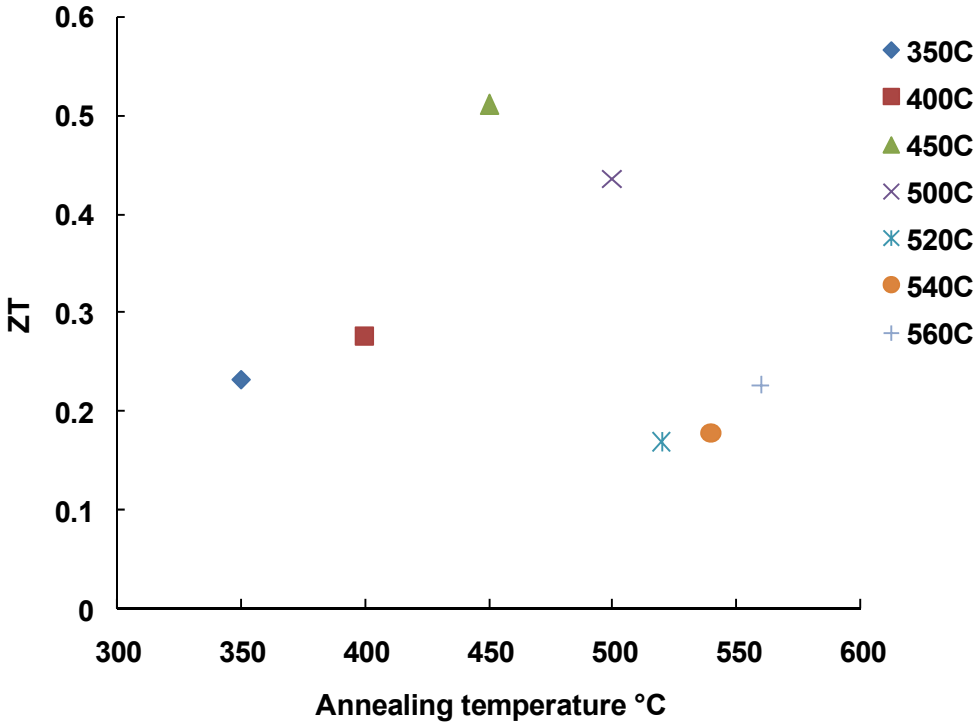

Figure 27 Room temperature *ZT* as a function of annealing temperature.

In summary, undoped n-type polycrystalline $Bi_2Te_{2.85}Se_{0.15}$ has been successfully fabricated by cold pressing and annealing. The transport properties, determined primarily by carrier concentration, are very sensitive to processing parameters. Annealing could be visualized as a dynamic equilibrium between homogenization through solid state diffusion and formation of antisite defects and vacancies induced by chalcogen evaporation. If the annealing temperature is

too low, the homogenization is incomplete resulting in inferior properties. If the temperature is too high, the excessive holes generated by electronically active defects will compensate the electrons and shift the carrier concentration out of the optimized zone. Thus a proper combination of annealing temperature and time is crucial to fine tune the carrier concentration. For our undoped n-type $Bi_2Te_{2.85}Se_{0.15}$ polycrystals, the sample annealed at 450°C for 2-3 days exhibits the highest ZT_{max}=0.51 at 300K.

3.3 Synthesis and TE properties of n-type $Bi_2Te_{2.85}Se_{0.15}$/xPbTe nanocomposite (NC)

The synthesis of nanocomposites involved dispersion of an appropriate mass of PbTe nanoparticles into a minimum amount of solvent, hexane. The resulting solution was sonicated for 10 minutes to make a colloidal suspension. The PbTe nanoparticle sol was then added dropwise to $Bi_2Te_{2.85}Se_{0.15}$ powders with constant stirring. The slurry was continuously stirred to facilitate incorporation of the PbTe nanoparticles throughout the matrix, then left to dry under ambient temperature and pressure inside Ar purged glovebox. This process is a variant of the incipient wetness impregnation technique. The resultant composite was placed inside a carbon crucible and heated at 410°C for two hours to pyrolyze organic ligands encapsulating the PbTe nanoparticles. The heat treated powder was then hot pressed inside a 12 mm graphite die under a pressure of 60 MPa at an approximate temperature of 350°C for 5 minutes. A total of five samples have been prepared with PbTe NP weight percentage of 0wt%, 0.1wt%, 1wt%, 5wt% and 10wt% respectively. The 0wt% sample represents the pure $Bi_2Te_{2.85}Se_{0.15}$ with no added PbTe NPs which serves as the control sample. All $Bi_2Te_{2.85}Se_{0.15}$ powders come from the same

batch which eliminates the influence of property deviation from the matrix material. The pressed disks all have densities greater than 90% of the theoretical density. Here for the sake of simplifying the discussion, we use the weight percentage of PbTe NPs to designate our samples.

X-ray diffraction scans were performed on all samples confirming that $Bi_2Te_{2.85}Se_{0.15}$ is the major phase with trace amount of PbTe phase observed around 39 degree 2θ. Figure 28 is the Hall coefficient as a function of temperature. As it can be seen from Figure 28, the matrix x=0 is n-type; upon adding PbTe NPs, the R_H is first reduced a little for x=0.1 sample, and gradually converted to positive region at low temperature. Sample x=5 and x=10 have overlapping temperature dependence of R_H, which starts from about 1×10^{-7} $\Omega m T^{-1}$ at 60K, gradually decreases crossing over 0 at 350K and falls into the negative region.

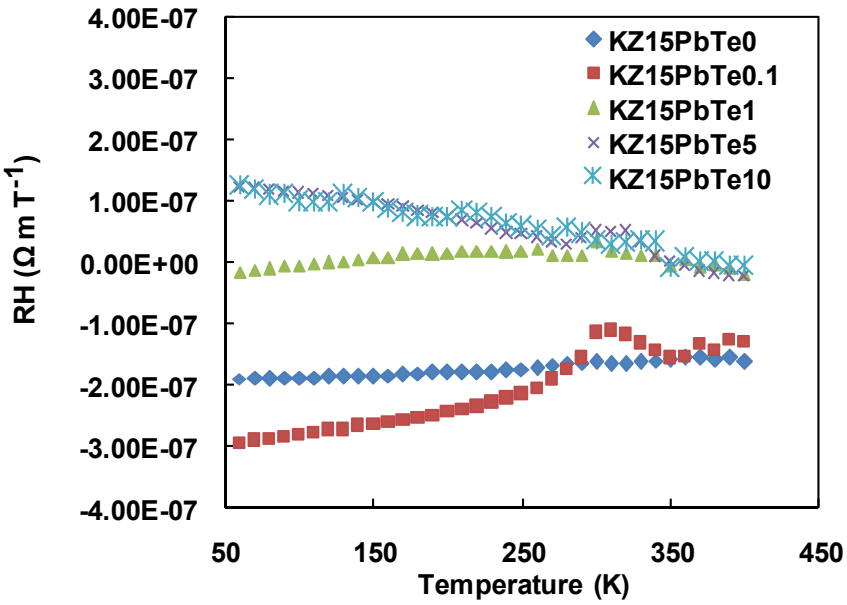

Figure 28 Hall coefficient as a function of temperature for $Bi_2Te_{2.85}Se_{0.15}$/PbTe NCs

Such a behavior can be explained by the two carrier system as shown in Equation 59, where $c=\mu_e/\mu_p$ is the mobility ratio between electrons and holes. Adding PbTe NPs into the n-type $Bi_2Te_{2.85}Se_{0.15}$ matrix introduces holes, which even converts the n-type matrix into p-type semiconductor at higher PbTe weight percentages. As temperature increases, the higher mobility of electrons leads to their dominance over the holes and brings R_H for x=5 and x=10 into the n-type region.

$$R_H = -\frac{3\pi}{8e}\frac{nc^2 - p}{(nc+p)^2} \qquad 59$$

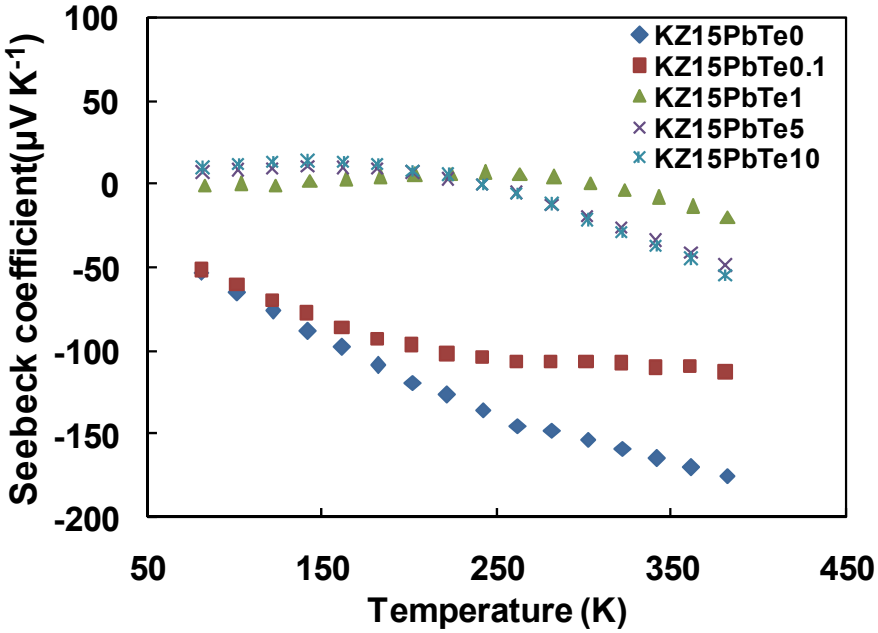

Figure 29 Thermopower as a function of temperature for $Bi_2Te_{2.85}Se_{0.15}$/PbTe NCs

Figure 29 displays the Seebeck coefficient as a function of temperature for NCs. The behavior of the Seebeck coefficients confirms the result of the Hall measurement that the

existence of two carriers leads to the reduction of the absolute value of thermopower as described in Equation 60

$$S = \frac{S_e\sigma_e + S_h\sigma_h}{\sigma_e + \sigma_h} \qquad 60$$

Figure 30 shows the electrical resistivity as a function of temperature for NCs. Resistivity for all samples except x=0.1 exhibits a metallic behavior. Resistivity ρ first increases with the addition of PbTe NPs from 0.1wt% up to 5wt% then decrease in 10wt% sample. The increase of ρ in NCs may be attributed to the reduced mobility from increasing carrier scattering between electrons and holes. The facts that x=10 has a lower resistivity than x=5 and x=0.1 exhibits an activated behavior above room temperature once again suggest that PbTe NPs generate holes in the n-type matrix and electrons in $Bi_2Te_{2.85}Se_{0.15}$ have a higher mobility than the holes.

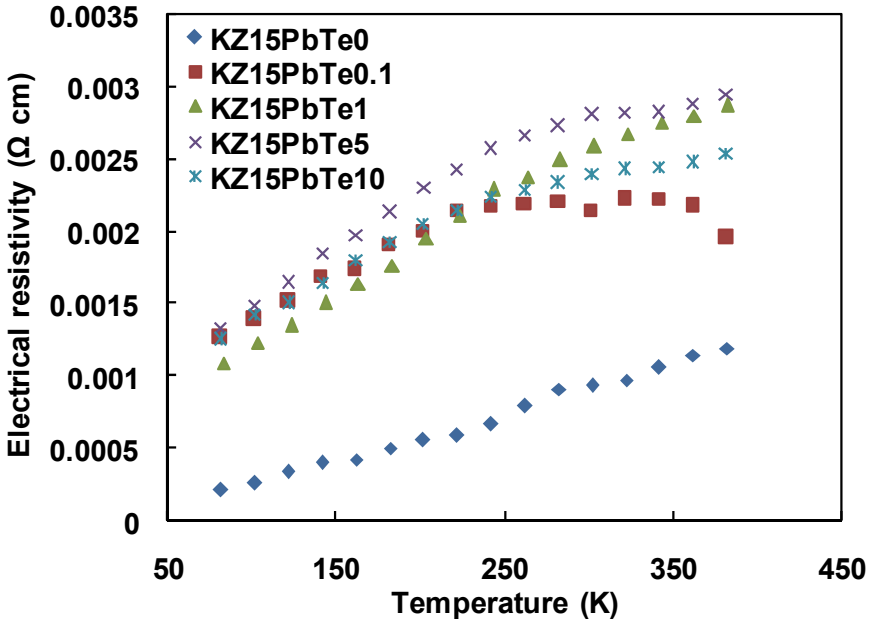

Figure 30 Electrical resistivity as a function of temperature $Bi_2Te_{2.85}Se_{0.15}$/PbTe NCs

Because of the decrease of the absolute Seebeck coefficient and increase of electrical resistivity, the power factors (Figure 31) in the NCs are lower than the pure matrix $Bi_2Te_{2.85}Se_{0.15}$. The reduction of power factor is evident even in the smallest PbTe NPs loading amount at 0.1wt%.

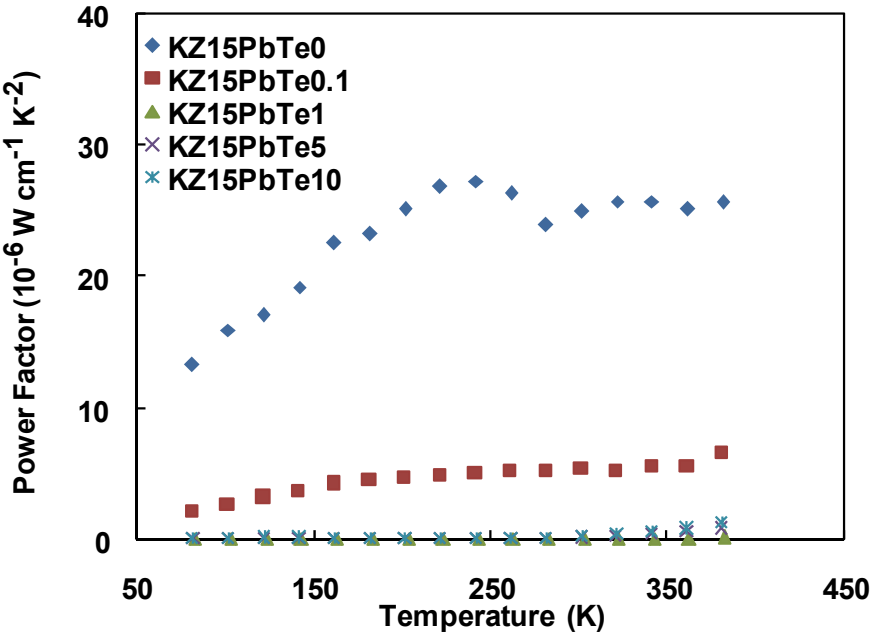

Figure 31 Power factor as a function of temperature $Bi_2Te_{2.85}Se_{0.15}$/PbTe NCs

The temperature dependence of the thermal conductivities κ is plotted in Figure 32. Lower PbTe containing samples x=0.1 and x=1 have a comparable thermal conductivity with the matrix material x=0. NCs x=5 and x=10 with higher PbTe NPs addition indeed show a reduced thermal conductivity below 300K but it rises faster and eventually exceeds the thermal conductivity of matrix material at 380K due to the much stronger influence from the bipolar thermal diffusion.

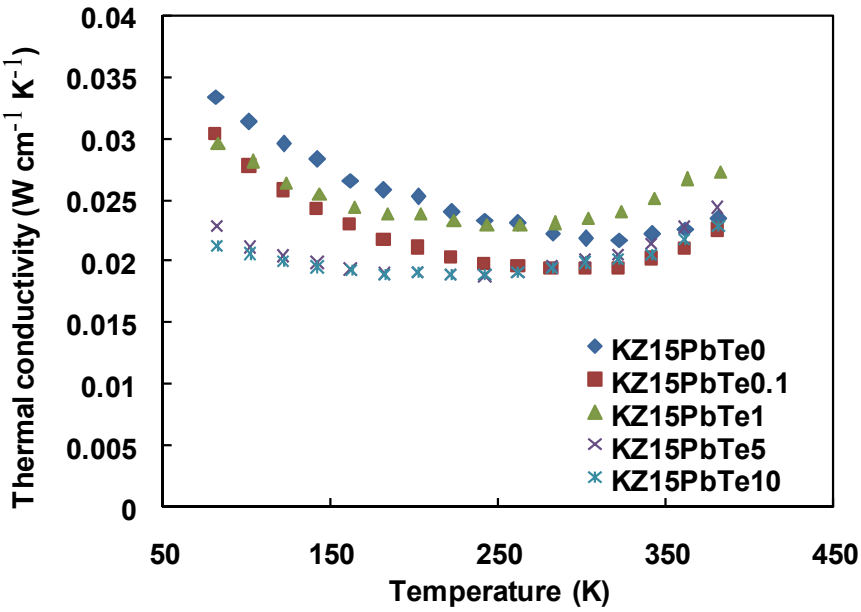

Figure 32 Thermal conductivity as a function of temperature for $Bi_2Te_{2.85}Se_{0.15}$/PbTe NCs

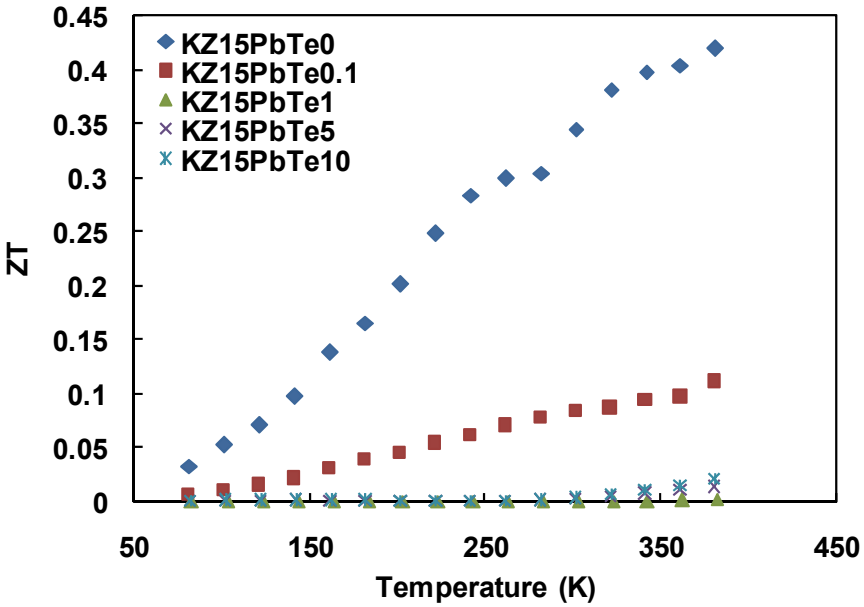

Figure 33 *ZT* as a function of temperature for $Bi_2Te_{2.85}Se_{0.15}$/PbTe NCs

Because of the strongly degraded electronic properties, *ZT* (Figure 33) in NCs are not enhanced compared to the matrix material. Because of the intrinsic p-type doping behavior of the PbTe NPs, we shifted our focus to the p-type bismuth telluride based NCs in order to avoid the two carrier system.

3.4 Synthesis and TE properties of p-type $Bi_{0.4}Sb_{1.6}Te_3$

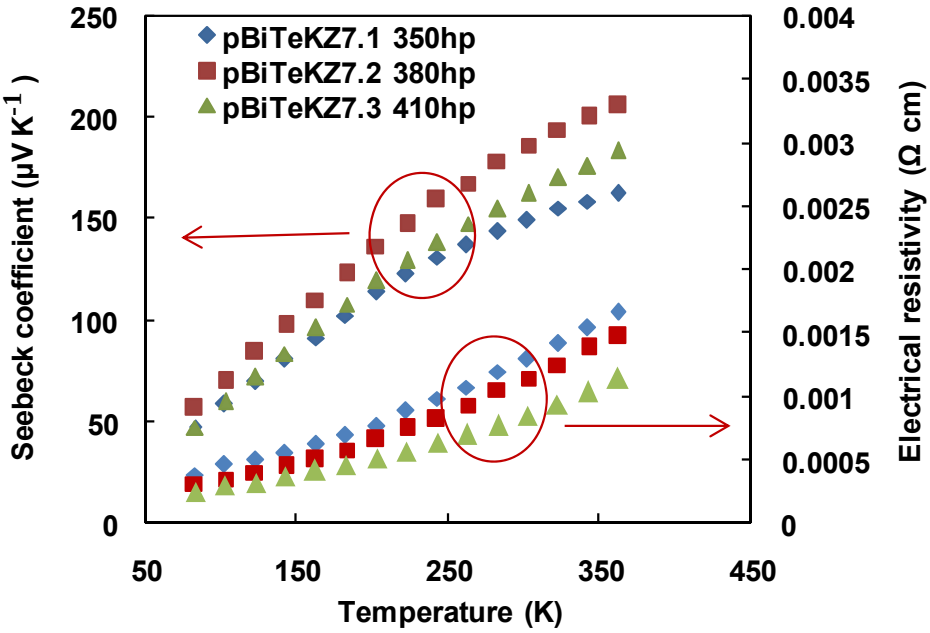

Figure 34 Seebeck coefficient and electrical resistivity as a function of temperature for $Bi_{0.4}Sb_{1.6}Te_3$ hot pressed at 350°C, 380°C and 410°C

P-type bismuth antimony telluride with nominal composition $Bi_{0.4}Sb_{1.6}Te_3$ was employed as the matrix material for making p-type nanocomposites. This matrix is a solid solution of 20% Bi_2Te_3 and 80% Sb_2Te_3 and can be seen more explicitly if we writte the chemical formula as $(Bi_2Te_3)_{0.2}(Sb_2Te_3)_{0.8}$. The synthesis procedure is identical to the

preparation of n-type matrix except the annealing temperature is set at 540°C for three days in order to homogenize the properties, and 1wt% excess Sb is added as a p-type dopant. The batch is labeled as pBiTeKZ7. X-ray diffraction has been performed on pulverized powders and confirmed the phase purity. The powders were hot pressed at 350°C, 380°C and 410°C respectivley for 15 minutes in order to find the optimum processing parameter. All hot pressed pucks have a density greater than 90% of the theoretical density.

Figure 34 shows the Seebeck coefficient and electrical resistivity as a function of temperature for p-type matrix hot pressed at 350°C, 380°C and 410°C. Seebeck coefficient first increases then decreases with the hot pressing temperature. The sample hot pressed at 380°C has the highest Seebeck coefficient about 200 μV/K at 360K. Electrical resistivity shows a monotonic reduction with the increase of hot pressing temperature.

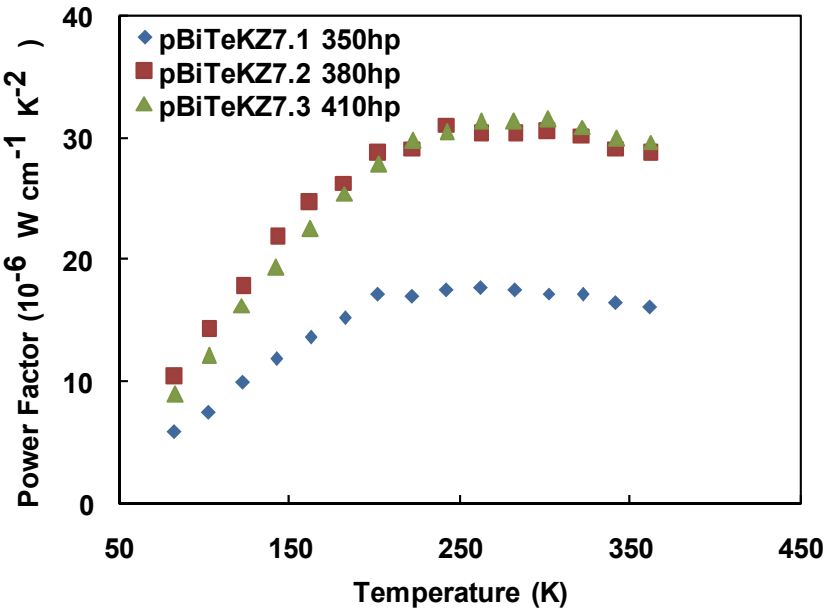

Figure 35 Power factor as a function of temperature for $Bi_{0.4}Sb_{1.6}Te_3$ hot pressed at 350°C, 380°C and 410°C

Figure 35 shows the power factors of the hot pressed p-type matrix materials. The sample hot pressed at 380°C has an overlapping power factor with sample hot pressed at 410°C. The peak power factors for sample 7.2 and 7.3 are about 30 $Wcm^{-1}K^{-2}$ at room temperature, well in the range reported in the literature.[62] Sample 7.1 showed a lower peak factor of 18 $Wcm^{-1}K^{-2}$.

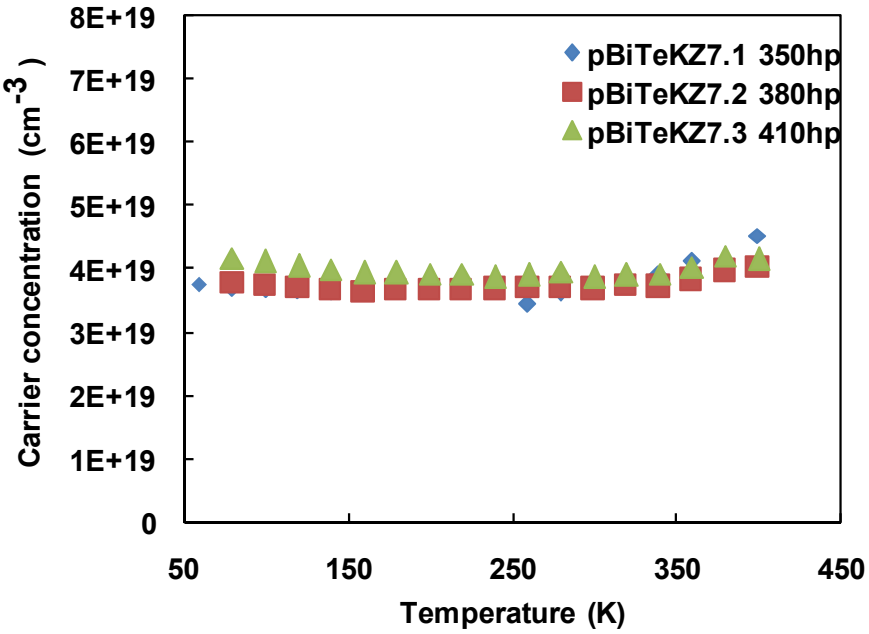

Figure 36 Carrier concentration as a function of temperature for $Bi_{0.4}Sb_{1.6}Te_3$ hot pressed at 350°C, 380°C and 410°C

Figure 36 reveals the temperature dependence of the carrier concentration. The carrier concentrations are identical for all samples at about 4×10^{19} cm^{-3} and are insensitive to the pressing temperature, suggesting a successful extrinsic doping. The carrier mobility as a function of temperature is plotted in Figure 37. Sample pBiTeKZ7.1 hot pressed at 350°C shows a lower mobility compared to other two hot pressed at higher temperature. The difference may result from a different degree of anisotropy due to the pressing temperature.

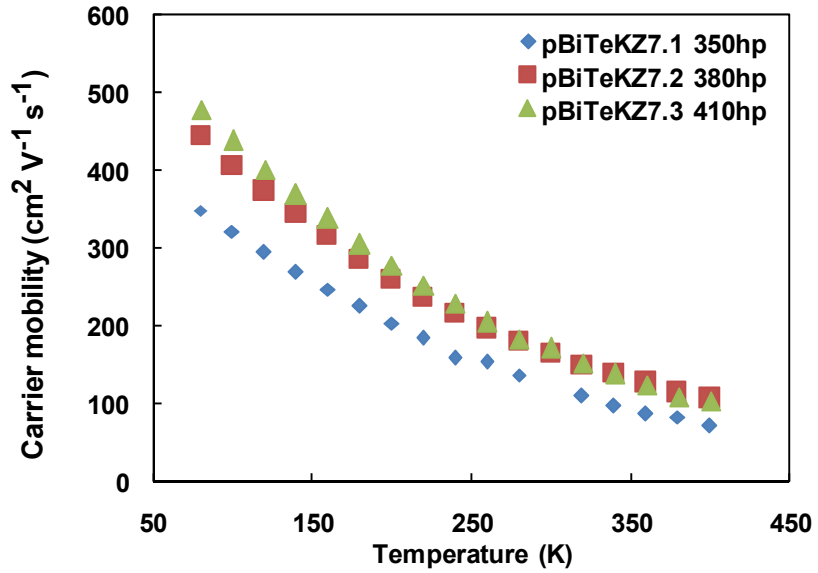

Figure 37 Carrier mobility as a function of temperature for $Bi_{0.4}Sb_{1.6}Te_3$ hot pressed at 350°C, 380°C and 410°C

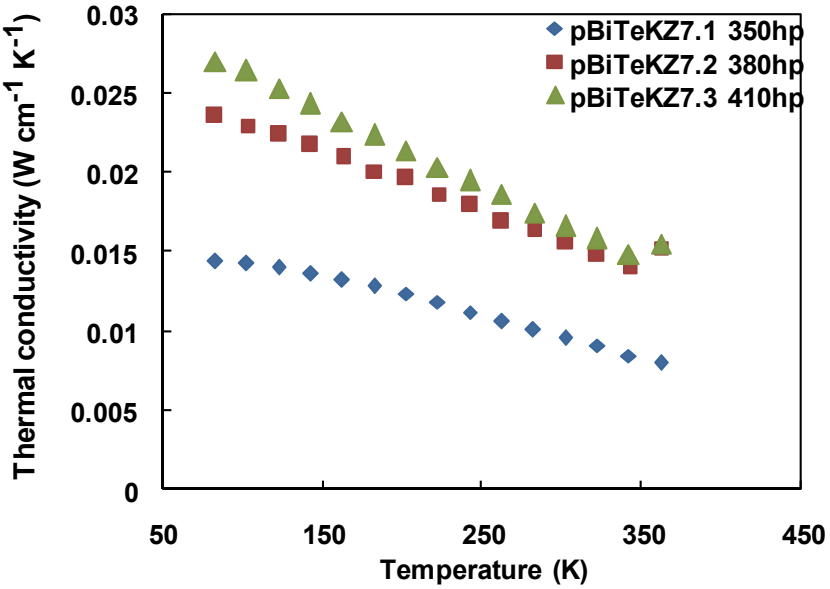

Figure 38 Thermal conductivity as a function of temperature for $Bi_{0.4}Sb_{1.6}Te_3$ hot pressed at 350°C, 380°C and 410°C

The thermal conductivity as a function of temperature plotted in Figure 38 corroborates our assumption. Sample pBiTeKZ7.1 exhibits the lowest thermal conductivity, while those for the other two samples are identical to each other.

Despite the difference between electronic properties and thermal conductivities, the *ZT* (shown in Figure 39) for samples hot pressed at different temperatures are almost the same in the whole temperature regime of the measurement, reaching ZT_{max}=0.73 at 360K.

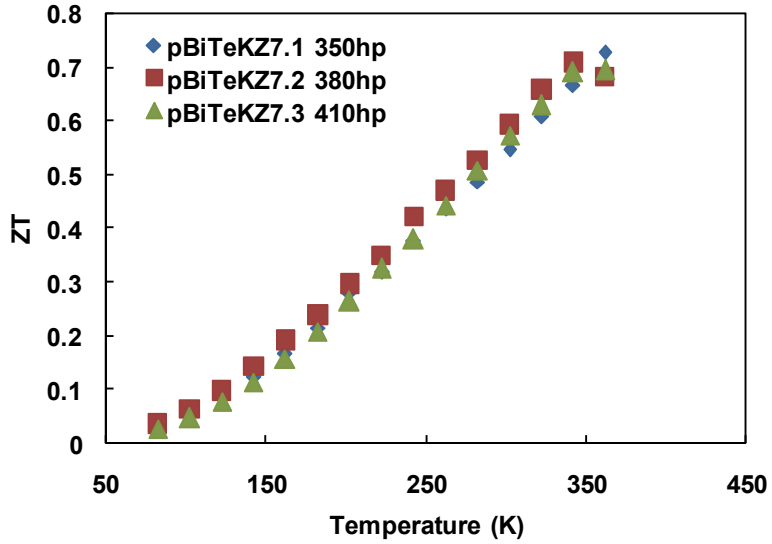

Figure 39 *ZT* as a function of temperature for $Bi_{0.4}Sb_{1.6}Te_3$ hot pressed at 350°C, 380°C and 410°C

3.5 Synthesis and TE properties of p-type $Bi_{0.4}Sb_{1.6}Te_3$/xPbTe nanocomposite (NC)

The synthesis of p-type $Bi_{0.4}Sb_{1.6}Te_3$/xPbTe NC follows the same procedure as that of the n-type NC described in Section 3.3. The mixed composite powder was loaded into a graphite crucible and heated at 410 °C for 2 hours in order to eliminate residual organics at the surface of the PbTe NPs. The heat treated powder was then hot pressed between at 380 °C under a pressure

of 60MPa for 15 minutes to form a dense disk. A total of four samples with PbTe weight percentage of 0%, 0.1%, 0.5% and 1% were prepared. The 0% sample was a pure $Bi_{0.4}Sb_{1.6}Te_3$ fabricated in the same procedure as NCs to serve as a control sample. Densities for all hot pressed samples are above 94% of the theoretical density. As in Section 3.3, we use the weight percentage x of PbTe NPs to designate our samples in order to simplify the discussion. Table 2 lists the identification of the samples together with some room temperature physical properties.

Sample name	x=0 (control)	x=0.1	x=0.5	x=1
PbTe nanoparticles weight percentage	0%	0.1%	0.5%	1%
Relative density	95.74%	97.09%	96.32%	94.15%
Seebeck coefficient (10^{-6} V/K)	186	136	110	84
Electrical resistivity (mΩ cm)	1.14	0.672	0.688	0.500
Power factor (10^{-6} $Wcm^{-1}K^{-2}$)	30.15	26.48	18.11	15.37
Thermal conductivity (10^{-2} W/cm-K)	1.48	1.65	1.71	1.81
Lorenz number (10^{-8} WΩ K^{-2})	1.65	1.78	1.82	2.00
Carrier density (10^{-19} cm^{-3})	3.68	5.41	7.90	10.8

Table 2 Sample identification and some room temperature physical properties of $Bi_{0.4}Sb_{1.6}Te_3$/xPbTe NC

The oleate groups terminating the surface of PbTe NPs can be expected to act as insulating barriers, decreasing the overall electrical conductivity of the system [69, 70]. To remove the oleate ligands, both thermal as well as chemical treatments were explored. For the chemical treatments, PbTe NPs dispersed in hexane were stirred along with anhydrous hydrazine followed by precipitation precipitated with acetonitrile [70]. The hydrazine-treated NPs retain the

cubic Altaite phase of the precursor NPs, but exhibit significant aggregation. A comparison of Infrared spectroscopy (IR) spectra obtained before and after hydrazine treatment is shown in Figure 40. The peak at 1512 cm^{-1} and 1394 $cm^{-1}$are attributed to the presence of symmetric and asymmetric stretching vibrations of oleate COO^-, whereas those at 2918 cm^{-1} and 2840 cm^{-1} correspond to oleate aliphatic –CH stretches. While significant reduction in peak intensity is observed complete removal of the oleate group was not achieved by hydrazine treatment.

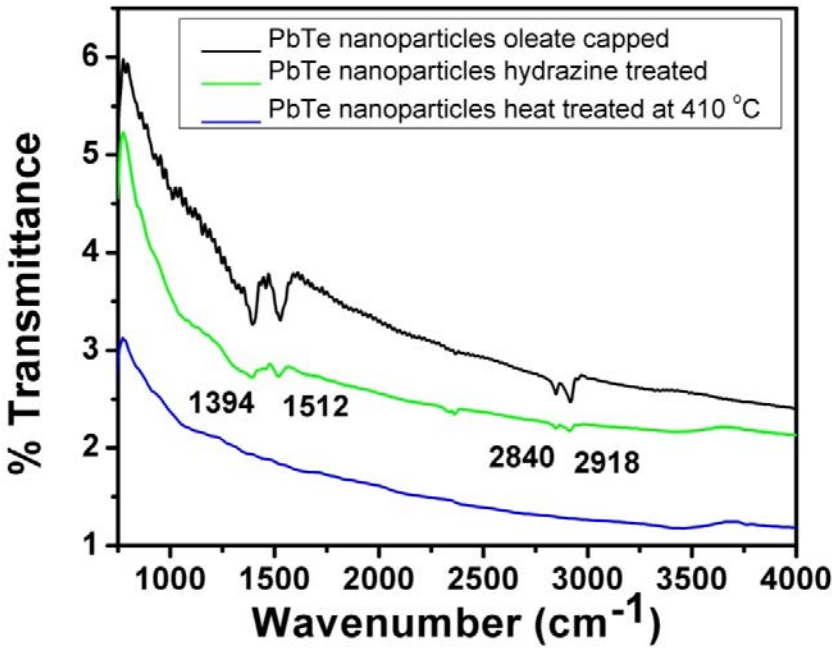

Figure 40 IR spectroscopy of hydrazine PbTe NPs with oleate ligands, hydrazine treated PbTe NPs and thermal treated PbTe NPs.

Thermal treatment was found to be more effective for oleate group removal. A suitable temperature was determined by thermogravimetric analysis (TGA). As shown in Figure 41 the TGA of the NPs revealed a 16 % weight loss overall between 255-455°C, which we attribute to desorption/decomposition of surface oleate functionalities. Based on the TGA data, heat

treatment of the nanoparticles was carried out in a flow furnace at 410 °C for 2 h under nitrogen. As it can be seen from Figure 40 both –COOH and the –CH stretching vibrations are absent after thermal treatment suggesting successful removal of the organic groups.

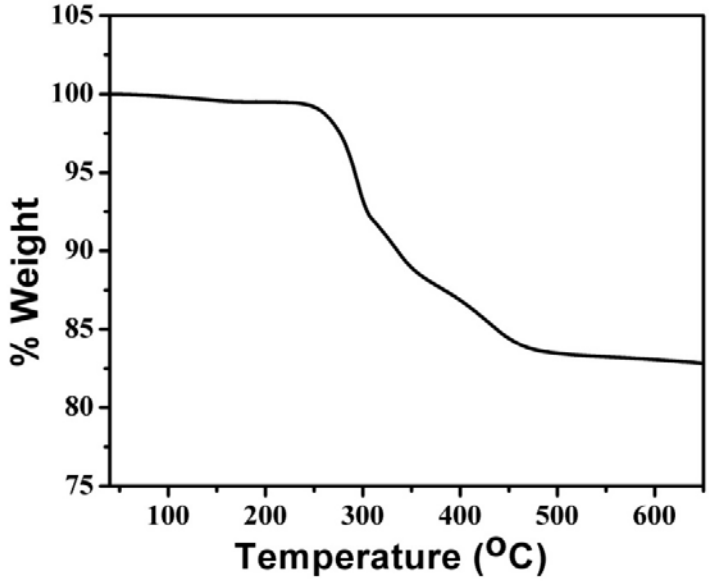

Figure 41 TGA of oleate capped PbTe NPs heat treated under N_2 atmosphere

Powder X-ray diffraction (PXRD) was collected on a Rigaku RU 200B (40kV, 150 mA, Cu Kα radiation) diffractometer. Samples were deposited on a quartz holder coated with a thin layer of grease and the data were acquired in the 2θ range 20-70° with a step size of 1.2°. PbTe NPs in the NCs cannot be detected by PXRD at the low concentrations explored here (Figure 42) due to sensitivity of the PXRD technique. In order to demonstrate that the PbTe phase can be retained under conditions of composite formation, an additional 10wt% PbTe NC sample was prepared. In this sample the most intense (220) plane of Altaite phase close to 40 degree 2θ is visible.

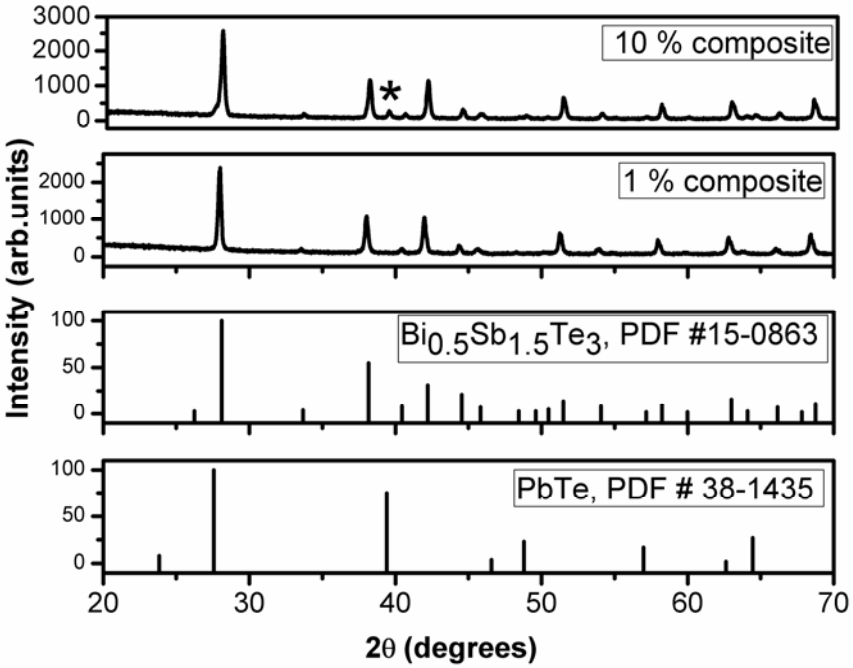

Figure 42 PXRD patterns of NCs with 1wt% and 10wt% PbTe NPs loading. Asterisk indicates the PbTe impurity phase.

Transmission electron microscopy (TEM) and energy dispersive spectroscopy (EDS) were performed using a JEOL 2010 transmission electron microscope operated at a voltage of 200kV and a current of 106-108 μA with a coupled EDS detector (EDAX Inc). Figure 43 shows the images of the precursor NPs as well as 1 wt %, 0.5 wt % and 0.1 wt % of PbTe nanoparticles in $Bi_{0.4}Sb_{1.6}Te_3$ matrix. The PbTe NPs were observed in all cases and showed no agglomeration, suggesting good dispersion. The presence of 13 nm sized PbTe cubes approximately scale with the nominal concentration of PbTe NPs added to the matrix. The elemental analysis (EDS) of the as prepared nanoparticles gives a composition of Pb:Te of 1:0.94 close to the ideal value of Pb:Te of 1:1, with a slight excess of Pb.

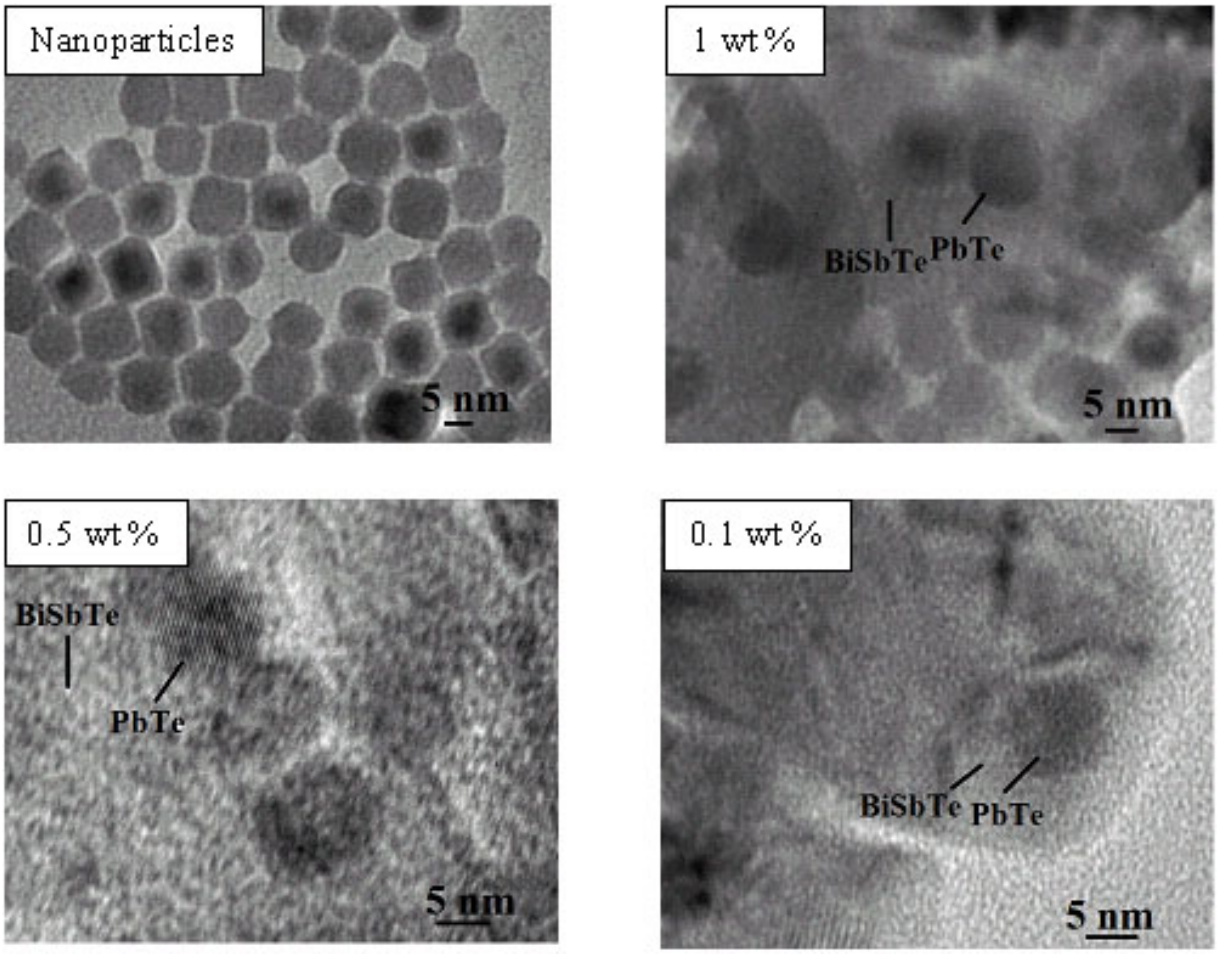

Figure 43 TEM images of PbTe NPs and NCs with 1 %, 0.5 % and 0.1 wt% discrete PbTe NPs inside the $Bi_{0.4}Sb_{1.6}Te_3$ matrix

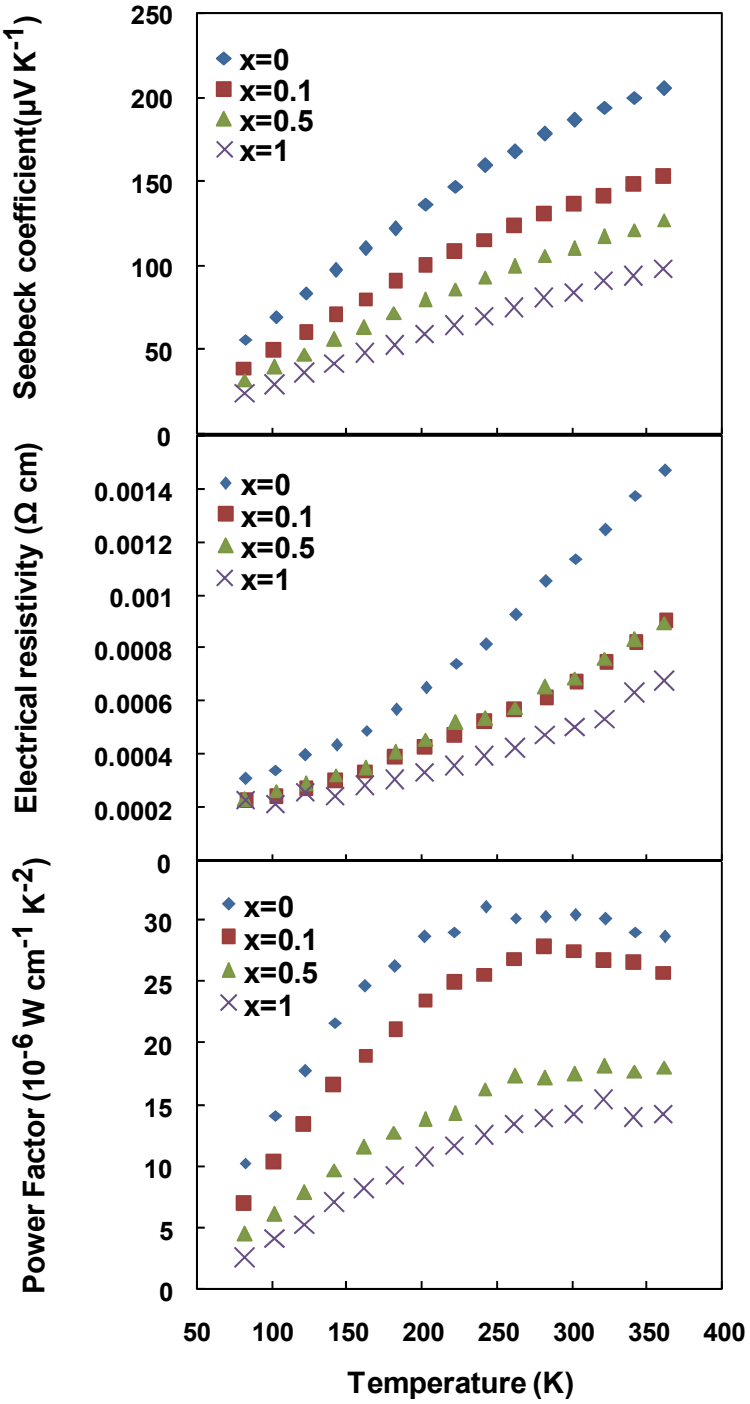

Figure 44 Seebeck coefficient, electrical resistivity and power factor as a function of temperature for $Bi_{0.4}Sb_{1.6}Te_3$/xPbTe NC

Figure 44 displays the temperature dependence of electronic properties for our nanocomposite samples as well as the control sample, x=0. The Seebeck coefficients of NCs decrease monotonously with increasing concentration of PbTe NPs. The electrical resistivity exhibits the same trend, except that x=0.1 and x=0.5 have nearly identical values. Despite the decrease in resistivity the thermoelectric power factors ($S^2\sigma$) of nanocomposites are lower than the control sample due to the much stronger reduction of the Seebeck coefficients.

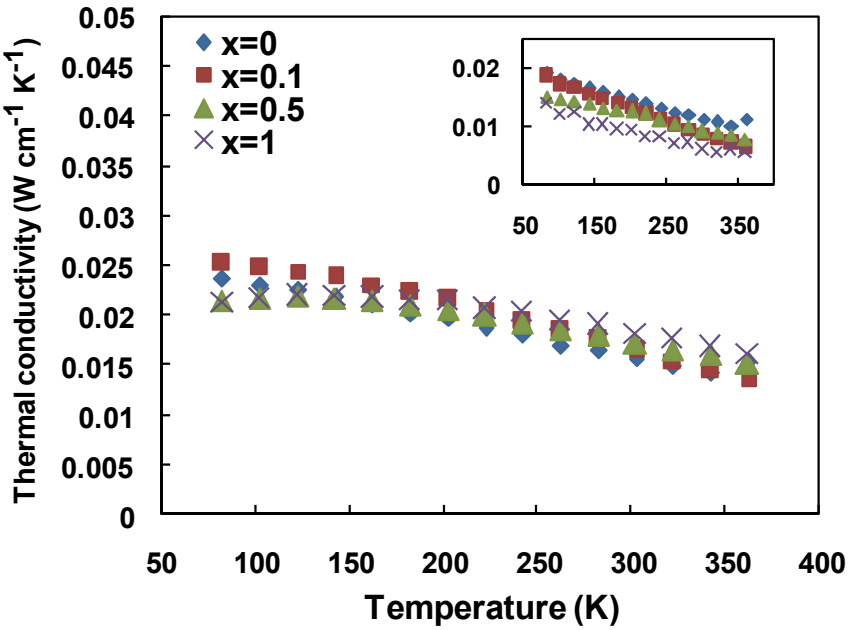

Figure 45 Thermal conductivity as a function of temperature for $Bi_{0.4}Sb_{1.6}Te_3$/xPbTe NC. The inset shows the lattice thermal conductivity as a function of temperature.

Figure 45 shows the thermal conductivity as a function of temperature. The lattice thermal conductivity κ_l shown in the inset of Figure 45 was calculated by subtracting the electronic thermal conductivity κ_e from the total thermal conductivity. The electronic thermal conductivity is estimated by using Wiedemann-Franz law $\kappa_e = L\sigma T$, where L is the Lorenz number,

σ the electrical conductivity and T the absolute temperature. The choice of a reasonable Lorenz number is a delicate issue as we cannot assume our samples to be degenerate semiconductors. We also note that there is approximately a factor of three differences between the most resistive and least resistive samples, so one Lorenz number may not fit all data equally well. To tackle this problem, we first estimated the reduced Fermi energy η from the Seebeck coefficient by using

$$S = \mp\frac{k}{e}\left\{\frac{\left(\frac{5}{2}+s'\right)F_{3/2+s'}}{\left(\frac{3}{2}+s'\right)F_{3/2+s'}}-\eta\right\} \qquad 61$$

where k is the Boltzmann constant s' is the exponent of energy in the scattering law, $\tau \sim E^{s'}$ and F is the Fermi-Dirac integral defined in Equation 17. For this study, we use s'=-0.5, a value typically used for acoustic phonon scattering of carriers in Equation 61 to estimate the reduced Fermi energy η. From η, we calculated the Lorenz number by:

$$L = \frac{3F_0F_2 - 4F_1^2}{F_0^2}\left(\frac{k}{e}\right)^2 \qquad 62$$

A more detailed description of the above analysis can be found in reference [1]. We repeated this process for each sample in order to get a more accurate estimation about lattice thermal conductivity. The calculated Lorenz number for different samples can be found in Table 2. We found that, despite overall increase in total thermal conductivity, lattice thermal conductivities in NCs are indeed reduced compared to the matrix sample due to the additional phonon scattering resulting from the PbTe NPs. The lattice thermal conductivity of sample x=1 is reduced by close

to 50% compared to the control sample. The increase of thermal conductivity in NCs comes from the increased electronic thermal conductivity κ_e.

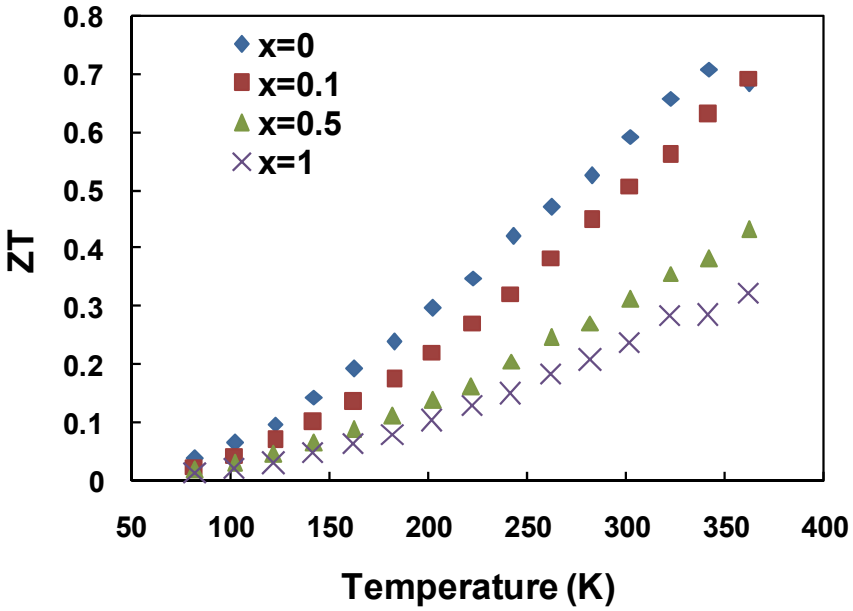

Figure 46 *ZT* as a function of temperature for $Bi_{0.4}Sb_{1.6}Te_3$/xPbTe NC.

Figure 46 shows FOM *ZT* as a function of temperature. *ZT*s of NCs are reduced compared to matrix due to the decreased Seebeck coefficient. A noticeable *ZT* reduction starts at PbTe loading as little as 0.5wt%.

Figure 47 shows the carrier concentration as a function of temperature. The hole concentration increases with increasing PbTe concentration, suggesting a doping effect of PbTe nanoparticles. This doping effect may come either directly from PbTe as an inclusion, since PbTe is generally a p-type semiconductor, or from Pb^{2+} leaching from the incorporated

nanoparticles and occupying the Bi^{3+} site, generating a hole and thus increasing the overall hole concentration. This hypothesis is consistent with the work by Kusano and coworkers, who have

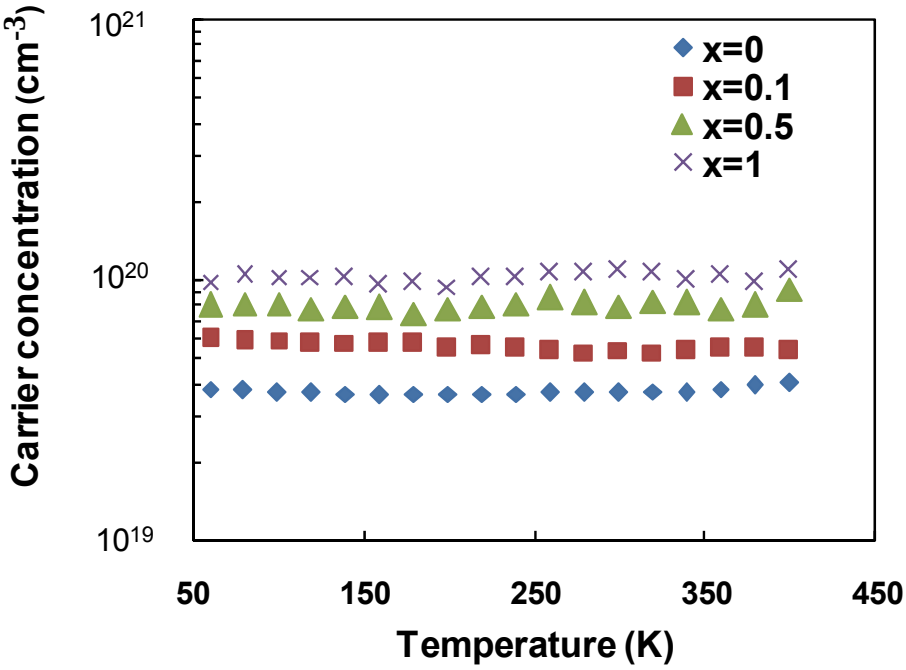

Figure 47 Temperature dependence of carrier concentration for $Bi_{0.4}Sb_{1.6}Te_3$/xPbTe NC.

attempted to mechanically alloy bulk bismuth antimony telluride and PbTe and consolidated the powder by spark plasma sintering. The TE transport properties of such composite materials exhibited a similar trend as in our study and they concluded the increase of carrier concentration is due to the doping effect of PbTe.[71] Pb was also used as a p-type dopant for both Bi_2Te_3 and Sb_2Te_3 as reported by Plachacek *et al*. where they concluded that the increase of hole concentration was attributed to the interaction between Pb atom and native point defects in Bi_2Te_3 and Sb_2Te_3. [72, 73]

$$S \propto \frac{k}{e}\left(s' + const + \ln \frac{2\left(2\pi m^* kT\right)^{3/2}}{h^3 n_p} \right) \qquad 63$$

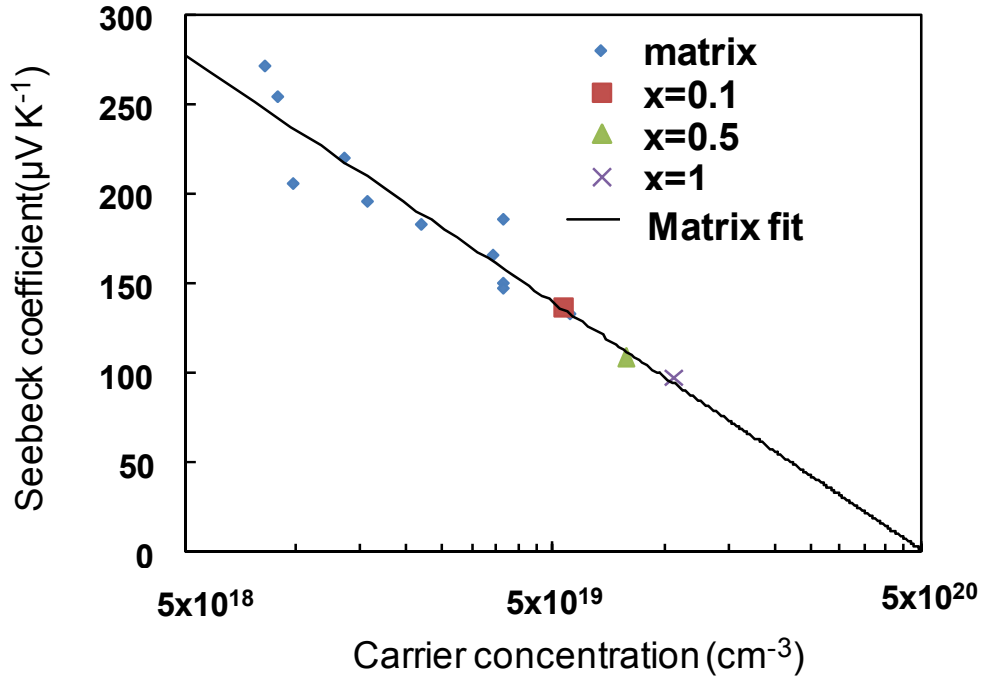

Figure 48 Pisarenko relation of NCs. The fitted line is constructed as an aid to the eye. All matrix bismuth antimony telluride of various carrier concentrations were synthesized in our lab.

To elucidate the effect of PbTe NPs on the Seebeck coefficient of the matrix $Bi_{0.4}Sb_{1.6}Te_3$, we plot the Pisarenko relation of our p-type matrix $Bi_{0.4}Sb_{1.6}Te_3$ and NCs (shown in Figure 48). The fit line is created from a number of $Bi_{0.4}Sb_{1.6}Te_3$ samples of various carrier concentrations synthesized in our lab. From the approximate Equation 63, based on a simplified one carrier model [36], for a series of samples that share the same exponent of scattering *s'* and approximately the same effective mass *m**, the Seebeck coefficient is

proportional to the logarithmic inverse of the hole concentration n_p and should fall close to the fitted line in a plot constructed as in Figure 48. The points representing NCs fall in the vicinity of the fitted line in Figure 48. This suggests that the charge carrier scattering mechanism for NCs is the same as for matrix materials if we assume the effective mass is not affected by a low percentage of PbTe incorporation. As the doping effect of PbTe NPs has been confirmed, it is reasonable to attribute part of the reduced lattice thermal conductivity to the phonon scattering caused by the collateral PbTe doping. Such a behavior has been reported by Zhu *et. al*. in antimony telluride doped with lead telluride [74].

3.6 Summary of the chapter

We systematically investigated the thermoelectric properties of bismuth telluride and its alloys based nanocomposites with PbTe as nanoinclusions. The NCs were synthesized using a novel incipient wetness impregnation method wherein nanosized PbTe NPs were encapsulated in bulk bismuth telluride matrix. NCs that retain the nanosized PbTe inclusions have been successfully synthesized. Introducing PbTe NPs inside the n-type matrix materials generates a two carrier system which generally is not a favorable case for TE materials. For p-type NCs, the Seebeck coefficients and electrical resistivity decrease with the addition of PbTe NPs. The lattice thermal conductivity also decreases with the addition of PbTe NPs and the carrier concentration increases with the increasing concentration of PbTe NPs. The Pisarenko relation reveals that the carrier scattering mechanism in the nanocomposites does not deviate from that of the bulk bismuth antimony telluride. Considering the presence of PbTe NPs found in hot pressed NC samples, we conclude that the effect of doping from PbTe dominates that from nanostructuring.

Chapter 4 Unfilled P-type Skutterudite Based Nanocomposite

Skutterudite compounds were identified as good candidates for TE application almost two decades ago.[75] Unfilled skutterudites are binary compounds of the form MA_3, where M is a metal such as Co, Rh, or Ir, and A is As, P, or Sb.[76, 77] The high carrier mobility and large effective mass [78, 79] found in some skutterudites endow them with power factors comparable to and even exceeding Bi_2Te_3 and PbTe. Their thermal conductivities, on the other hand, are relatively too large to make them useful TE materials.[10, 78] Previous attempts at reducing thermal conductivity focused on inserting foreign atoms into the large voids in the unfilled skutterudite structure, thus producing "filled" skutterudite compounds.[80-82] Figure 49 schematically shows the unit cell of a filled skutterudite. The foreign atom confined in the cage exhibits an Einstein-like mode that provides additional phonon scattering to dampen the lattice thermal conductivity.[10, 83, 84] This approach has achieved great success especially in enhancing the *ZT* in n-type filled skutterudites, for instance, it is not unusual for double-filled skutterudites to display[85] *ZT* greater than 1.3, and the melt-spun filled skutterudites containing InSb nanoinclusions reaching[27] *ZT* in excess of 1.4. Recently, even p-type filled skutterudites exceeded *ZT* of unity [40].

Another direction originating from a different train of thought for improving the TE properties is to reduce the dimension of materials' building block, also referred to as "nanostructuring". The physics is either to evoke quantum confinement in order to alter the DOS[86] or to tweak the electron scattering parameter so that one may have the chance to boost the Seebeck coefficient, and hence the power factor.[21] The thermal conductivity is also

expected to be reduced because of the extra phonon scattering from the myriad of nanoscopic interfaces.

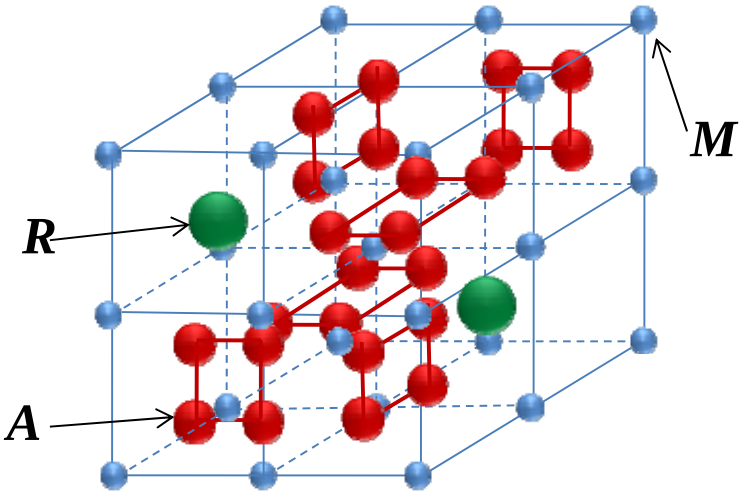

Figure 49 Unit cell of a filled skutterudite. *R*: filler atom, *M*: transitional metal, *A*: pnicogen atom

In this chapter, we report work on bulk p-type skutterudite nanocomposites of $Co_{0.9}Fe_{0.1+x}Sb_{3+2x}$. This composition can be reformulated as a base composition of $Co_{0.9}Fe_{0.1}Sb_3$ and a variant part of $FeSb_2$. It is our interest to initially demonstrate whether these nanocomposites can be synthesized and, if so, whether the existence of nanoinclusions can offer any positive influence. Four samples were synthesized with x = 0, 0.05, 0.1, and 0.2 respectively. A fifth sample was fabricated with composition $Co_{0.75}Fe_{0.25}Sb_3$ that has the same Fe/Co ratio as that of x=0.2 sample. Here x = 0 and $Co_{0.75}Fe_{0.25}Sb_3$ both serve as control groups to discern if property changes are related to Fe substitution for Co or $FeSb_2$ nanoinclusions.

4.1 Experiment

High purity starting materials of Co (powder), Fe (powder), and Sb (lump) were weighed according to the stoichiometric ratio and charged into carbon coated ampoules. The ampoules were sealed under vacuum of 10^{-6} Torr, heated to 1373K to melt the materials, and rapidly quenched in a cold water bath. The quenched samples were annealed at 973K for 3 days.

A disk was cut from the middle of each annealed ingot and further sectioned into rectangular parallelepiped with dimensions of approximately 3mm × 3mm × 8mm for measuring transport properties from 80K to 300K. Seebeck coefficient, electrical resistivity, and thermal conductivity were measured from 80K to 300K under vacuum using a steady state technique in a continuous flow cryostat with liquid nitrogen as a refrigerant. The accuracy of the electrical resistivity and thermal conductivity measurement is limited by the precision in measuring dimensions of samples, namely the distance between two thermocouple probes and the cross sectional area. They are also affected by and the thermal and electrical contacts between thermocouple probes and sample, which applies to Seebeck coefficient too. We estimated a 10% uncertainty in transport properties measurement from 80K-300K. A thin slab of approximate thickness of 1mm was cut out of the same low temperature measurement sample for Hall measurement. Hall coefficients and electrical resistivity from 60K to 400K were carried out using ac current in a varying magnetic field from -3T to 3T. The remnants from the disks were pulverized to powders for x-ray diffraction analysis and/or mounted on conducting epoxy for SEM imaging. X-ray diffraction patterns for all samples were collected from 2θ ranging from 20 to 90 degrees in a Rigaku MiniFlex 2 using Cu Kα radiation. SEM images were done in JEOL JSM 7500 high resolution field emission microscope.

High temperature TE transport properties were measured by our collaborators at University of Michigan. The electrical conductivity and the Seebeck coefficient in the interval 300K – 800K were measured in a home built apparatus under the protective atmosphere of argon on the same rectangular samples measured at temperatures below the ambient. Separate disks sectioned from individual ingots in proximity to where rectangular samples were cut were used for high temperature thermal conductivity measurements. The details for thermal conductivity measurement by laser flash technique have been described in previous experimental section.

4.2 Results

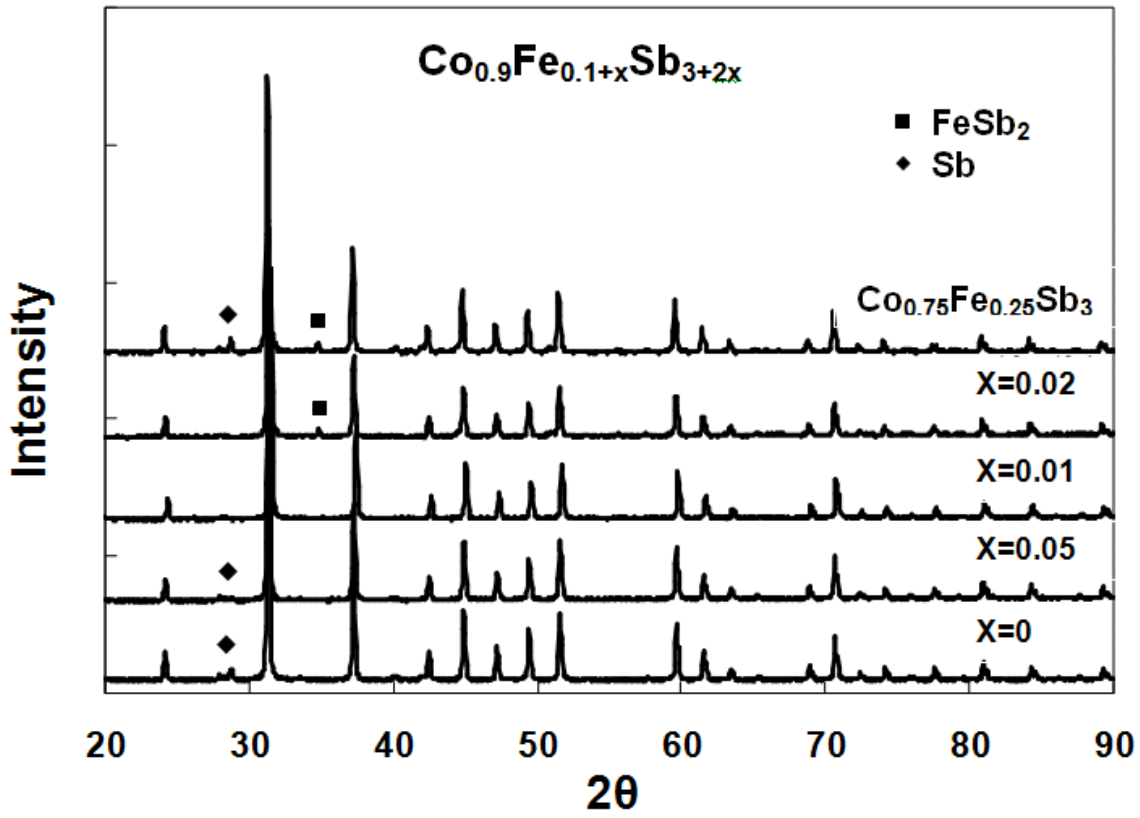

Figure 50 X-ray diffraction patterns of samples x=0, 0.05, 0.1, 0.2 and control sample $Co_{0.75}Fe_{0.25}Sb_3$

Figure 50 displays the x-ray diffraction patterns, which show that the skutterudite phase is the majority phase for all samples. A minute amount of Sb impurity phase is present in samples with x=0, x=0.05, and the control sample $Co_{0.75}Fe_{0.25}Sb_3$. As anticipated, the $FeSb_2$ phase can be found in samples with high Fe content, x = 0.2 and $Co_{0.75}Fe_{0.25}Sb_3$.

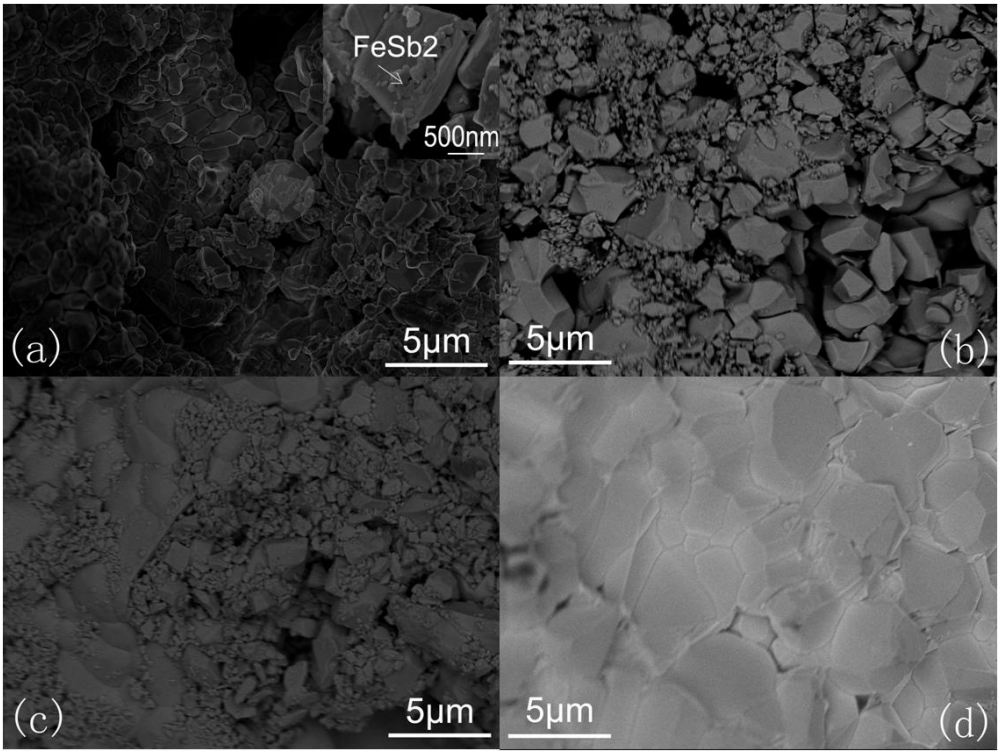

Figure 51 High resolution FESEM images on the fractured surface of nanocomposite samples $Co_{0.9}Fe_{0.1+x}Sb_{3+2x}$ and control sample $Co_{0.75}Fe_{0.25}Sb_3$. (a) x=0.05, the inset image zooms in the circled area to reveal the nanoscopic feature; (b) x=0.1; (c) x=0.2; (d) $Co_{0.75}Fe_{0.25}Sb_3$.

Figure 51 shows high resolution FESEM images of all nanocomposite samples (x=0.05, x =0.1, x=0.2), and control sample $Co_{0.75}Fe_{0.25}Sb_3$. The amount of nanoparticles present in the SEM images approximately scales with the $FeSb_2$ we intentionally added to the base composition $Co_{0.9}Fe_{0.1}Sb_3$ as shown from Figure 51 (a)–(c). In Figure 51 (d), which retains the

same Fe/Co ratio as x=0.2 sample but has the normal skutterudite composition MA_3, the nanoparticles have almost disappeared and grain boundaries are much cleaner compared to nanocomposite samples. This suggests that either Fe atoms were absorbed to form skutterudite or some $FeSb_2$ nanoparticles have grown up significantly to micron size. We also performed the EDS analysis in the same region as shown in Figure 51(b). By using "Point and ID Analyzer" function, we detected higher Fe but less Sb content in the regions with clusters of nanoparticles compared to the skutterudite grains without such features. Combined with x-ray diffraction results, we identified the nano-inclusions observed in our SEM images to be $FeSb_2$.

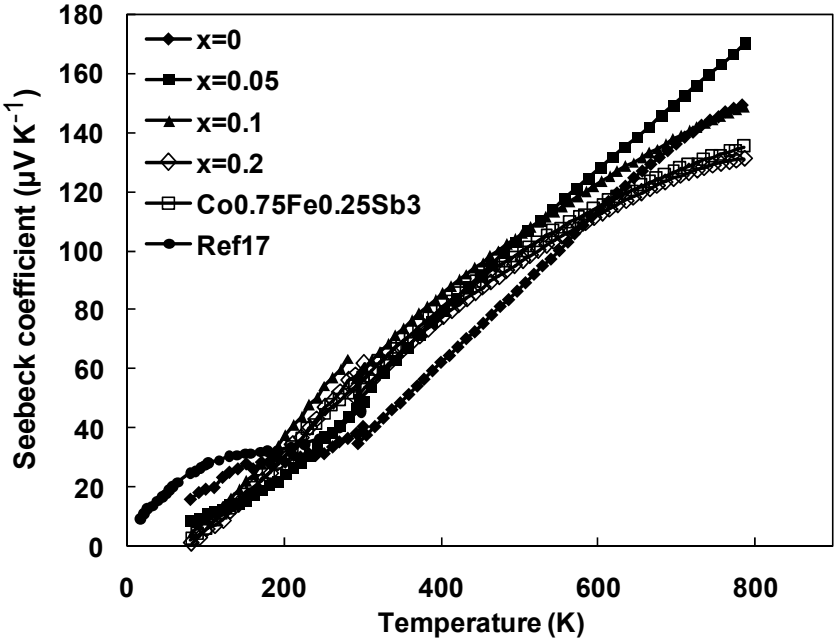

Figure 52 Seebeck coefficient as a function of temperature.
Ref data are excerpted from reference.[87]

The Seebeck coefficient as a function of temperature is plotted in Figure 52. Here, in order to compare their properties, we also include the results of $Co_{0.9}Fe_{0.1}Sb_3$ from the

literature.[87] All Seebeck coefficients increase monotonously with increasing temperature. Our base sample x=0 exhibits a very similar behavior to that of the reference. All nanocomposite samples and the higher Fe content control sample $Co_{0.75}Fe_{0.25}Sb_3$ exhibit higher Seebeck coefficients than the x=0 sample between 160K and 565K. Samples x=0.05 and x=0.01 extend the lead all the way up to the measurement limit at 788K. The Seebeck coefficients for the nanocomposite samples first increase with the amount of $FeSb_2$ (when $x<0.1$) and then start to drop for samples with higher amount of $FeSb_2$.

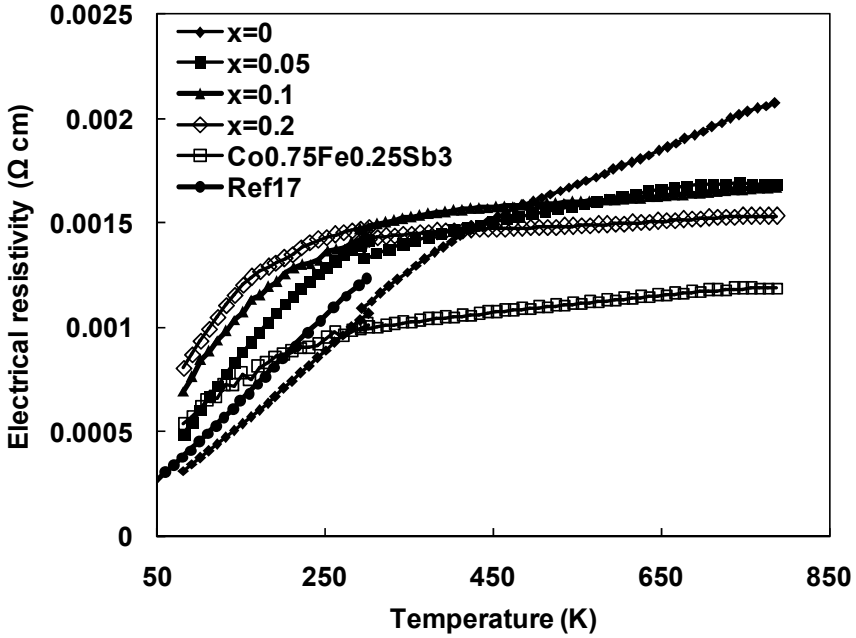

Figure 53 Electrical resistivity as a function of temperature

The electrical resistivity as a function of temperature is shown in Figure 53. The resistivity for all samples exhibits a metallic behavior, increasing with temperature. Nanocomposites have higher resistivity values than the control sample x=0 at lower temperature, but, interestingly, they begin to saturate near room temperature, a behavior that is not observed in

the sample with x=0. The crossover happens around 423K. Above 500K sample x= 0 has the largest electrical resistivity. $Co_{0.75}Fe_{0.25}Sb_3$ has the lowest resistivity, a phenomenon to be expected as the higher Fe substitution creates more holes, but it also exhibits the saturation behavior similar to the nanocomposite samples. The temperature dependence of power factor is displayed in Figure 54. All nanocomposite samples have higher power factors compared to control sample x=0. Sample x=0.05 shows the highest value of 17×10^{-6} $Wcm^{-1}K^{-2}$ at 788K.

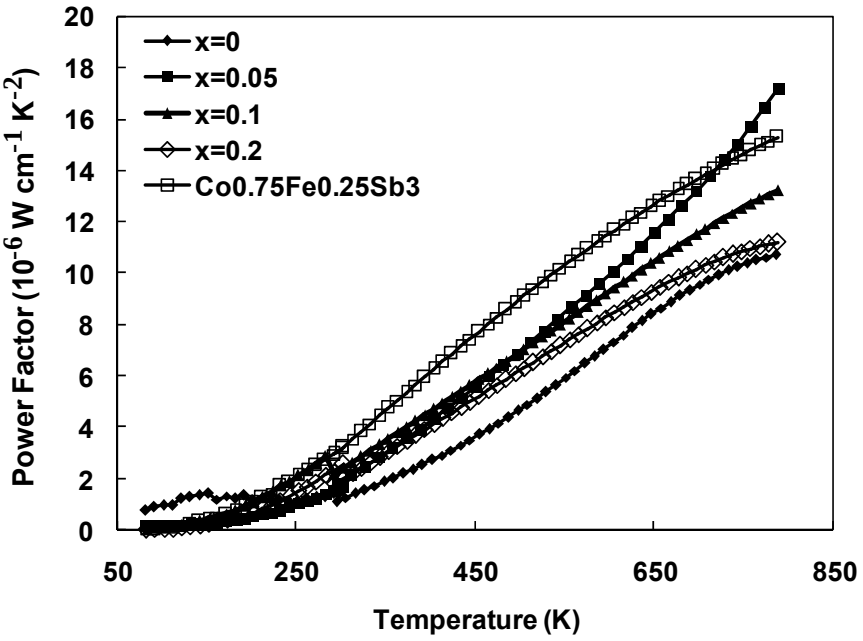

Figure 54 Temperature dependence of the power factor

The temperature dependence of the thermal conductivity is plotted in Figure 55. The thermal conductivity in all nanocomposite samples is substantially reduced with respect to the both control sample x=0 and $Co_{0.75}Fe_{0.25}Sb_3$ over the whole temperature range of measurement, and is even comparable to some filled skutterudites.[88]

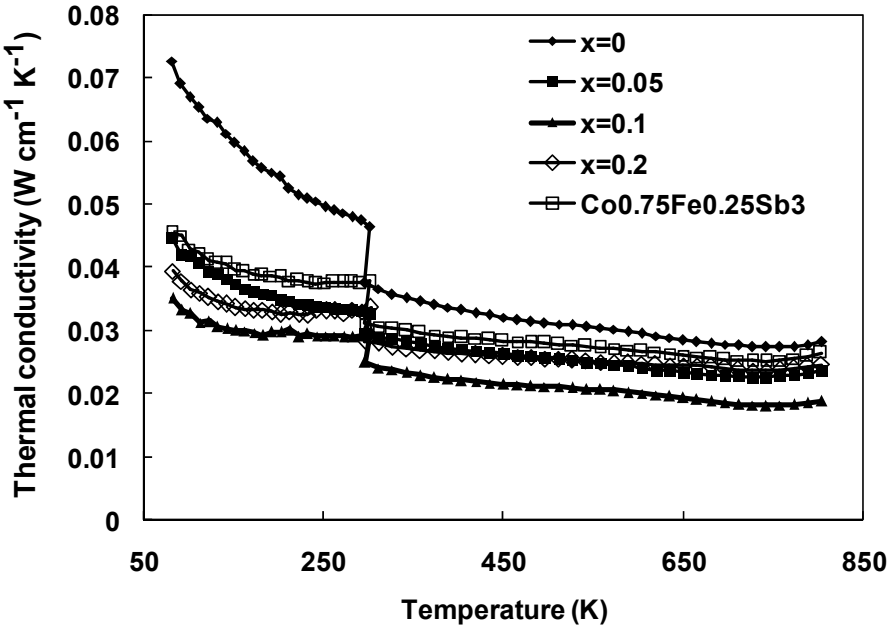

Figure 55 Thermal conductivity as a function of temperature

Mismatches between low and high temperature data sets at 300K for some samples do exist in electrical resistivity as well as thermal conductivity as shown in Figure 53 and Figure 55 respectively. The difference in resistivity is less than 6% for all samples. The largest difference in thermal conductivity is about 24% found in x=0 sample. We estimate the error is inherent to the geometric factor used for computing electrical resistivity and, in the case of thermal conductivity, due to different techniques used to determine thermal conductivity at low and high temperatures. The overall effect on *ZT*, however, is insignificant as the errors from resistivity and thermal conductivity partially cancel out each other. The combined enhancement of power factors and the reduction in thermal conductivity in our nanocomposites increase the *ZT* values compared to the control sample x=0 as shown in Figure 53. Sample x=0.05 displays a *ZT*=0.59 at 788K which is twice as large as that of sample x = 0, and shows no sign of reaching its peak at the limiting temperature of these measurements.

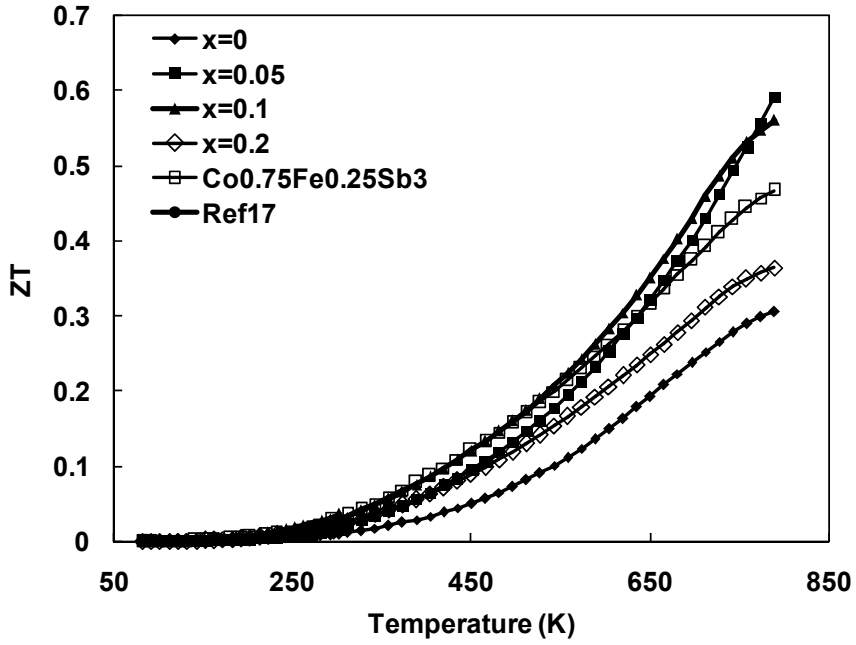

Figure 56 *ZT* as a function of temperature

4.3 Discussion

It is imperative to discern the influence of Fe substitution and justify that the enhancement of Seebeck coefficient can be attributed to the $FeSb_2$ nanoinclusions. To do so, we have calculated the lattice constant as a function of Fe substitution ratio on the metal site. Upon Fe replacement of Co, the lattice constant is expected to increase linearly with the Fe concentration. This is indeed the case for our control samples that satisfy the skutterudite formula MA_3 as shown in Figure 57. The lattice constants for the nanocomposites, on the other hand, first expand slightly compared to the control sample x=0, but eventually saturate with additional Fe content. This is a strong indication of the formation of $FeSb_2$ precipitates. For the $Co_{0.75}Fe_{0.25}Sb_3$ sample, the lattice constant is smaller than the value of 9.062Å reported on the

same composition.[89] So the actual amount of Fe going into the Co sites may be smaller than the stoichiometric amount, with the remaining Fe atoms combining with excess Sb to form $FeSb_2$.

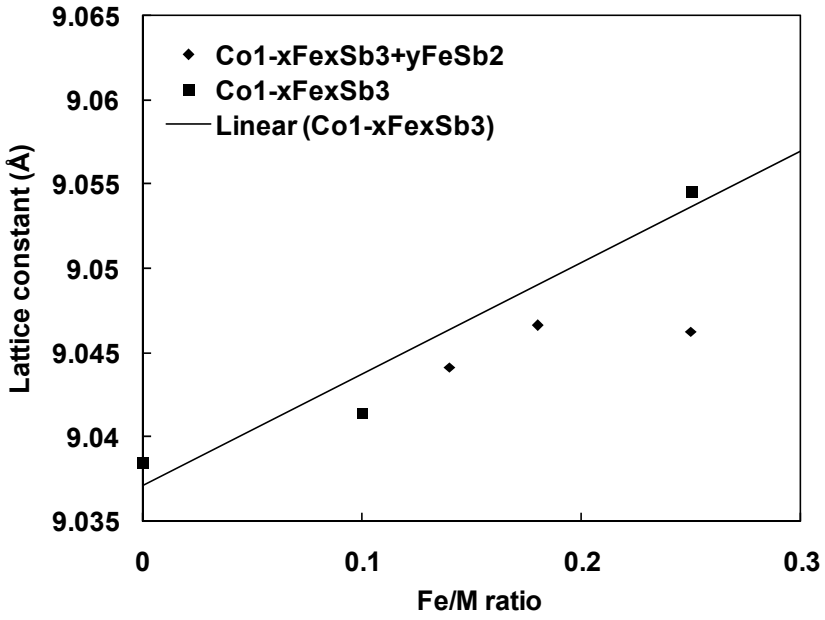

Figure 57 Lattice constant with respect to the Fe/metal ratio. The square at x=0 on the abscissa corresponds to $CoSb_3$ with a lattice constant of 9.0385Å[47]

We also plot the Seebeck coefficients at 300K as a function of hole concentration, known as the Pisarenko relation, in Figure 58. As Fe has one less valence electron than Co, Fe substitution for Co will increase the hole concentration. Thus given the similar DOS effective mass m^* and carrier scattering parameter s' (which determines the energy dependence of the carrier scattering time via the relation $\tau \sim E^{s'}$), the Seebeck coefficient should decrease with an increasing Fe substitution due to the increase of hole concentration. The data reported by Tang *et al* on $Fe_xCo_{4-x}Sb_{12}$ supports this assumption quite well.[89] Our control sample x=0 also agrees reasonably well with the fitted line based on Tang's data. The thermopowers for the

nanocomposites obviously diverge from the fit line for regular Fe substituted samples, which suggest the enhanced thermopower is due to an alteration either in the DOS effective mass m^* or the scattering parameter *s'* brought about by the $FeSb_2$ nanoinclusions. The other control sample $Co_{0.75}Fe_{0.25}Sb_3$ also diverges from the fit. Combining the analysis of the lattice constant and the behavior of the thermopower described above, we conclude that small amount of $FeSb_2$ must have existed in this sample too, influencing its properties.

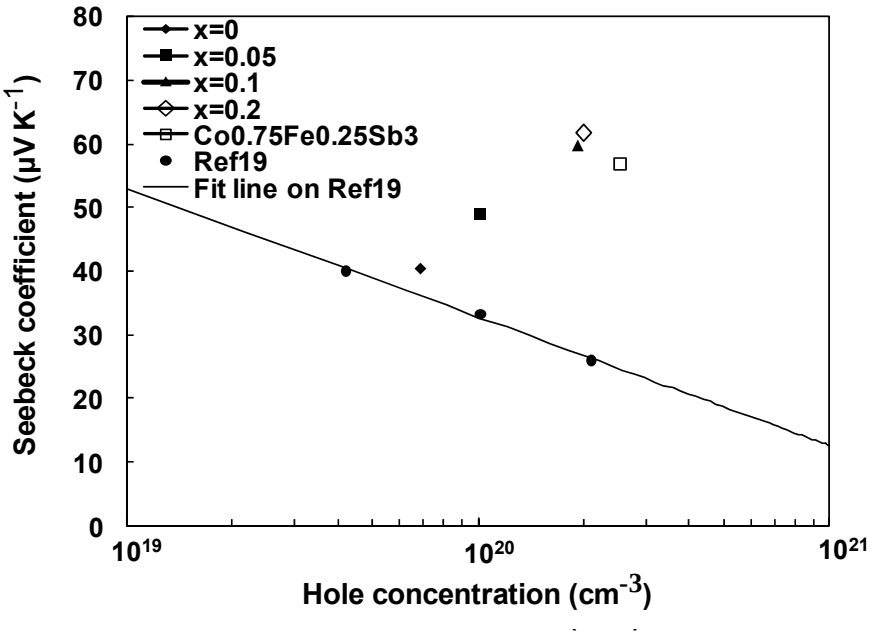

Figure 58 Seebeck coefficient as a function of hole concentration. Reference data are from Reference [88] on $Fe_xCo_{4-x}Sb_{12}$. The fitted line is calculated based on the reference.

4.4 Summary of the chapter

We have successfully synthesized p-type skutterudite nanocomposites based on $Co_{0.9}Fe_{0.1}Sb_3$ with $FeSb_2$ nanoinclusions. The existence of $FeSb_2$ nanoparticles not only provides extra phonon scattering that reduces the thermal conductivity, but also changes either

the DOS effective mass m^* or the scattering parameter s' resulting in an enhanced thermopower and hence power factors. Further experimental work and theoretical calculation is needed to determine which one plays a dominant role. The best nanocomposite sample displays a ZT=0.59 at 788K, which is a factor of two increase compared to the control sample x=0. Considering the prototype of the base material is Fe doped binary skutterudite, nanocomposite synthesis is a very promising approach for improving TE properties.

Chapter 5 High Temperature Thermoelectric and Magnetic Properties of P-type Yb filled skutterudite $Yb_xFe_yCo_{4-y}Sb_{12}$

In the previous chapter, we have successfully synthesized the unfilled p-type skutterudite nanocomposite and demonstrated a 100% enhanced thermoelectric performance. This inspired us to extend the work to p-type filled skutterudite. To do so, we need to identify a p-type matrix material upon which the nanocomposites can be created. Instead of using the Ce-filled p-type skutterudite, whose performance is the best so far, we took some effort to explore a new p-type system, the Yb-filled skutterudite.

Yb is an indispensible filling element in n-type filled skutterudites, but very little is known about their p-type counterparts for potential applications as thermoelectric materials. In this chapter, we report a systematic study of high temperature thermoelectric transport properties of p-type Yb-filled Fe-compensated skutterudites $Yb_xFe_yCo_{4-y}Sb_{12}$ with the aim to complement the knowledge base for the Yb-filled skutterudite family. The highest ZT_{max}=0.6 was found in $Yb_{0.6}Fe_2Co_2Sb_{12}$ at 782K. $YbFe_4Sb_{12}$ exhibits the second highest ZT_{max} =0.57 at780K, which is much higher than the previous estimate of 0.4 for the same composition. In addition, we also measured the magnetic properties of these compounds and our results agree with what have been reported previously.

5.1 Experiment

Pure element starting materials of Yb (pieces 99.9%), Fe (powder 99%), Co (powder 99.5%), and Sb (shot 99.999%) were weighed according to the stoichiometric ratio and placed inside graphite crucibles covered by graphite lids. The graphite crucibles were placed inside quartz ampoules and sealed under a vacuum of greater than 10^{-5} Torr. The graphite crucible serves as a protection layer to deter the spontaneous reaction between Yb and the quartz ampoule, which is otherwise very detrimental to TE properties especially at high rare earth filling fractions. From our experience, this step is crucial in order to obtain high quality homogeneous skutterudite ingots. The sealed ampoules were heated to 1373K at a rate slower than 0.5K/min and held at that temperature for 6 hours before rapid quenching in a cold water bath. The quenched samples were annealed at 923K for 3 days. The annealed ingots were ball milled into fine powders and hot pressed at 873K for 15min. The densities of all hot pressed samples are above 95% of the theoretical density.

A disk of approximately 1mm in thickness was cut from the as-pressed pellet for thermal diffusivity measurements. The balance of the pellet was sectioned into a rectangular parallelepiped with dimensions of approximately 2.4mm × 2.2mm × 8mm for Seebeck coefficient and electrical resistivity measurements. Details of the high temperature TE transport properties measurement techniques can be found in previous chapters. The magnetic properties were measured by the vibrating sample magnetometer (VSM) module in the Versalab. X-ray diffraction patterns for all samples were collected on powders in the range from 20 to 90 degrees of 2θ in a Rigaku MiniFlex II using Cu Kα radiation.

5.2 Results and discussion

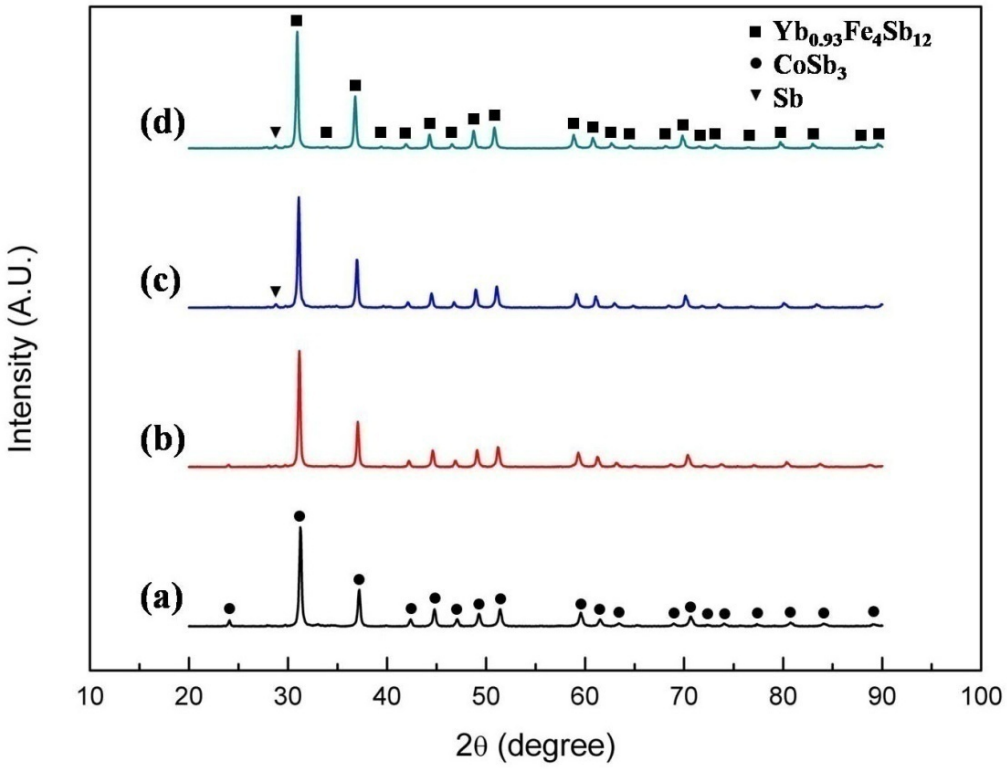

Figure 59 X-ray diffraction patterns for all samples. (a) x=0.4; (b) x=0.6; (c) x=0.8; (d) x=1

Four samples of $Yb_xFe_yCo_{4-y}Sb_{12}$ were prepared with x=0.4, y=1; x=0.6, y=2; x=0.8, y=3; and x=1, y=4. Table 3 summarizes some basic physical properties of these samples. Here, for the sake of simplicity, we identify our samples by their Yb filling fraction x. Figure 59 is the x-ray diffractogram for all samples. The characteristic peaks were indexed primarily to skutterudite phases with a trace of Sb impurity phase found in samples x=0.8 and x=1. The diffraction pattern of x=0.4 best matches the reference phase of $CoSb_3$ PDF#03-065-0671 and

Sample ID	x=0.4	x=0.6	x=0.8	x=1
Nominal composition	$Yb_{0.4}FeCo_3Sb_{12}$	$Yb_{0.6}Fe_2Co_2Sb_{12}$	$Yb_{0.8}Fe_3CoSb_{12}$	$YbFe_4Sb_{12}$
Estimated No. of carrier per formula unit	-0.2~0.2	0.2~0.8	0.6~1.4	1~2
Observed No. of carrier per formula unit	0.06	0.235	0.325	0.84
Carrier density at 300K ($\times 10^{20}$ cm^{-3})	1.479	6.03	8.54	21.5
Carrier mobility at 300K (cm^2 V^{-1} s^{-1})	28.95	14	17.3	9.53
Density (g cm^{-3})	7.512	7.635	7.927	7.895

Table 3 Some physical properties of Yb filled Fe compensated p-type skutterudite sample $Yb_xFe_yCo_{4-y}Sb_{12}$ at room temperature.

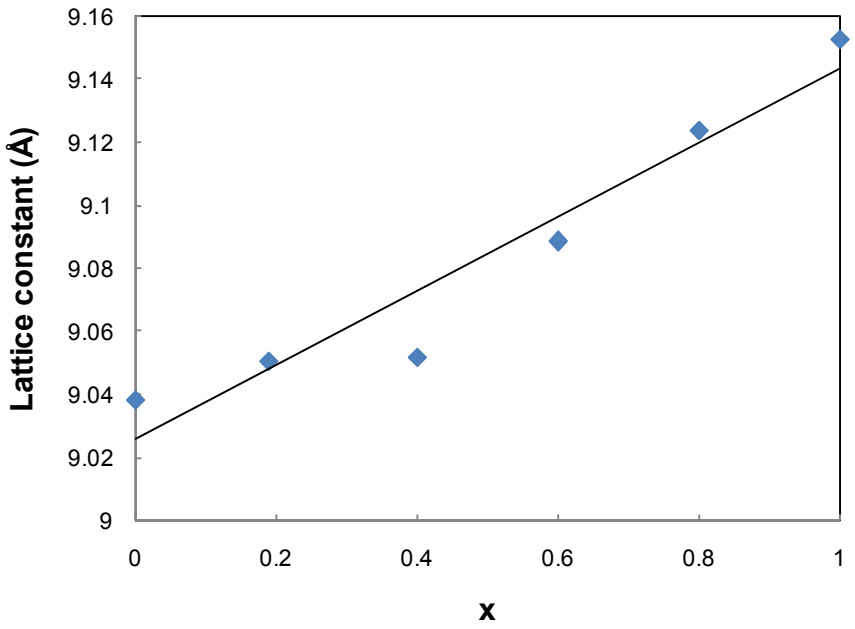

Figure 60 Lattice constant as a function of filling fraction x. Sample x=0.4 best matches $CoSb_3$ PDF#03-065-0671 while sample x=1 best matches $Yb_{0.93}Fe_4Sb_{12}$ PDF#00-056-1123. Lattice constants for x=0 and x=0.2 are from reference[47, 90]. Diffractions for other samples exhibit a gradual transition.

sample x=1 best matches that of $Yb_{0.93}Fe_4Sb_{12}$ PDF#00-056-1123, the skutterudite phase with the highest Yb filling fraction found in the database. Diffraction patterns for the remaining samples show a gradual transition from the binary $CoSb_3$ phase to the $Yb_{0.93}Fe_4Sb_{12}$ phase.

Figure 60 shows the lattice constant as a function of Yb filling fraction x. The lattice constant increases nearly linearly with the increasing amount of Yb, which is another good sign of successful rare earth filling. We must point out, however, that this linear expansion may not be the sole result of Yb filling, but a combination of Yb filling and Fe substitution for Co as the ionic radius for Fe^{2+} is larger than that of Co^{3+}. Nevertheless, the lattice constant for our x=1 sample is 9.153Å which agrees well with 9.156Å reported by Kuznetsov and Rowe for $YbFe_4Sb_{12}$[91] and 9.154Å by Berardan *et al*.[92].

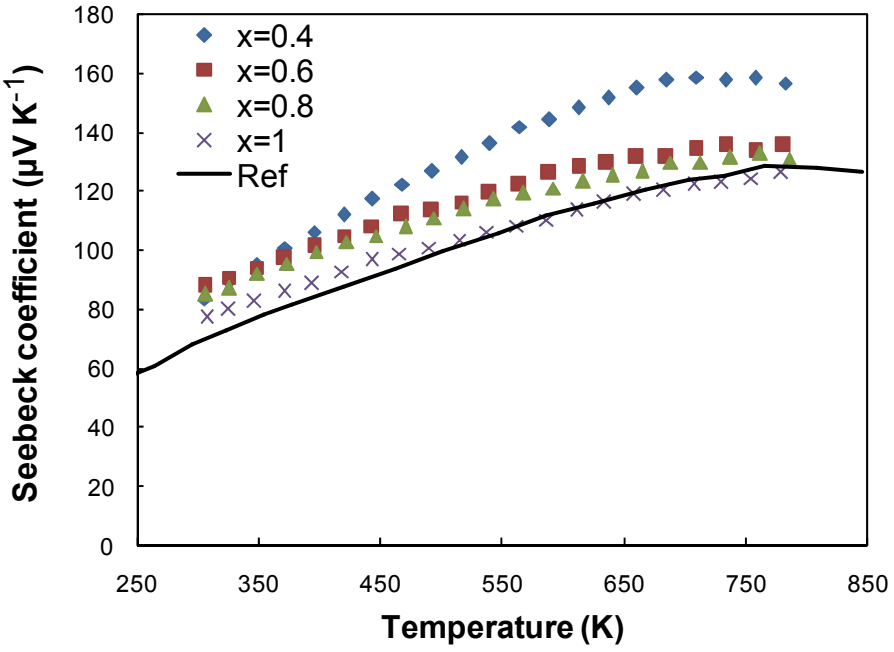

Figure 61 Temperature dependence of Seebeck coefficient. Ref data are the Seebeck coefficients of $YbFe_4Sb_{12}$ measured by Kuznetsov et al[91].

Figure 61 depicts the temperature dependence of the Seebeck coefficient. The Seebeck coefficient decreases with increasing Yb filling fraction x as a result of higher hole concentration induced by Fe compensation. The highest Seebeck coefficient was found in sample x=0.4 with its peak of 158 μV/K at 710K. The Seebeck coefficient for x=1 agrees well with that reported by Kuznetsov and Rowe for $YbFe_4Sb_{12}$.

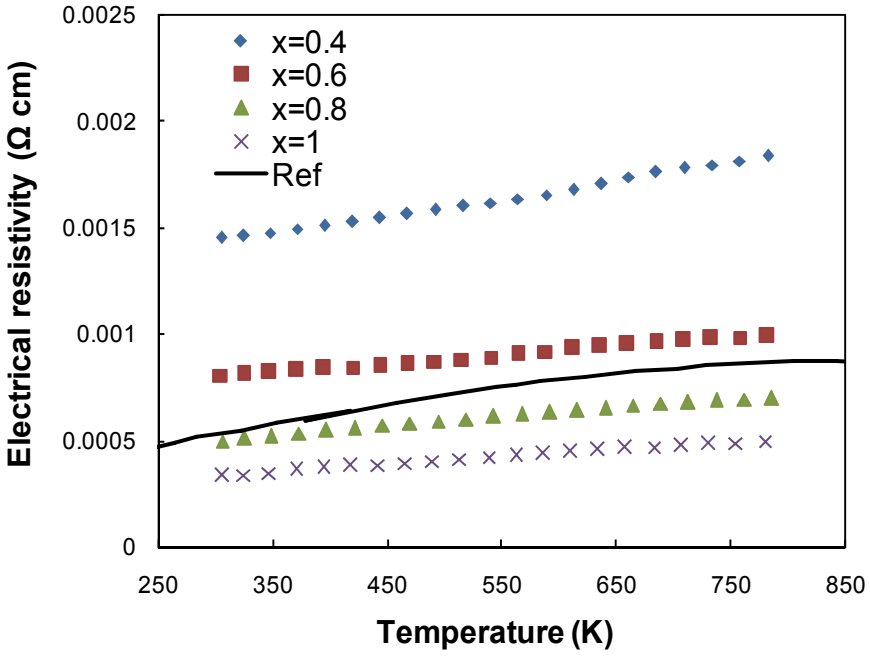

Figure 62 Electrical resistivity as a function of temperature. Ref data are $YbFe_4Sb_{12}$ measured by Kuznetsov et al[91]

Figure 62 shows the electrical resistivity as a function of temperature. Resistivity also decreases with increasing x as a result of the increasing carrier concentration. Our x=1 sample shows a resistivity smaller by almost a factor of two compared to that measured by Kuznetsov and Rowe. Therefore, as shown in Figure 63, the power factor in our x=1 sample is significantly enhanced compared to $YbFe_4Sb_{12}$ previously reported and is even on par with the power factor of

$Ce_{0.9}Fe_{3.5}Co_{0.5}Sb_{12}$. Power factor decreases with decreasing x value and is mostly influenced by the electrical resistivity as the Seebeck coefficients are comparable in all samples except x=0.4.

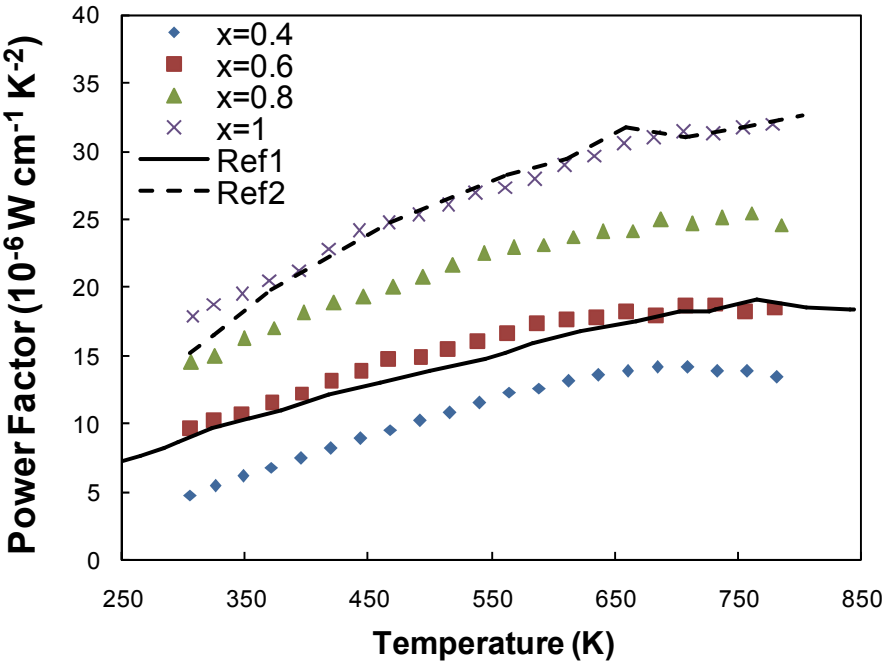

Figure 63 Power factors as a function of temperature. Ref1 are data calculated based on $YbFe_4Sb_{12}$ measured by Kuznetsov et al[91]. Ref2 is the power factor for $Ce_{0.9}Fe_{3.5}Co_{0.5}Sb_{12}$ synthesized by us as a control sample.

Figure 64 is the temperature dependence of thermal conductivity. The lattice thermal conductivity was obtained by subtracting the electronic part from the total thermal conductivity. The electronic thermal conductivity was estimated by using Wiedemann-Franz law $\kappa_e = L\sigma T$ where the Lorenz number $L=2.44\times10^{-8}$ $W\Omega/K^2$, a value reasonable for these degenerate semiconductors. Lattice thermal conductivities follow the *1/T* relation and decrease with increasing Yb filling fraction except for sample x=0.8. The lowest lattice thermal conductivity

was found to be 0.48 W/mK in sample x=1 at 710K. This value is very close to the theoretical limit of 0.2 W/mK that we have calculated assuming a phonon mean-free path equal to one interatomic spacing. Interestingly, the partially filled sample x=0.6 exhibits a smaller lattice thermal conductivity than the higher Yb filled sample x=0.8 and is very close to the fully filled sample x=1. Such a trend was observed previously in Ce-filled skutterudites at low temperatures. It seems to apply also in our case where a combination of different scattering processes (point defect, mass and size defect, and valence difference upon Fe substituting for Co) all contribute to the overall low lattice thermal conductivity.[78, 87, 93].

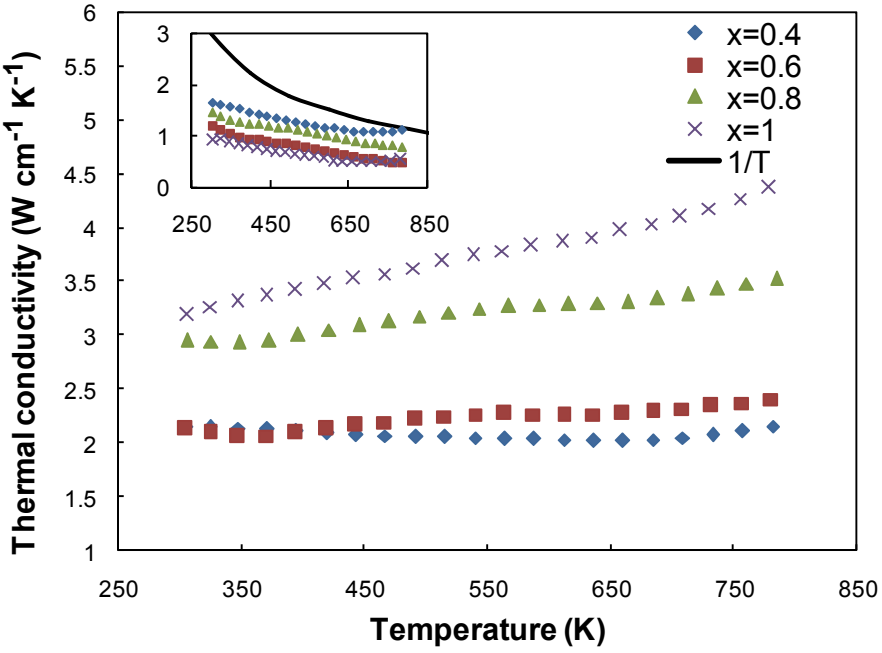

Figure 64 Thermal conductivity as a function of temperature. The inset graph shows the lattice thermal conductivity. 1/T relation is plotted as an aid to understand the graph.

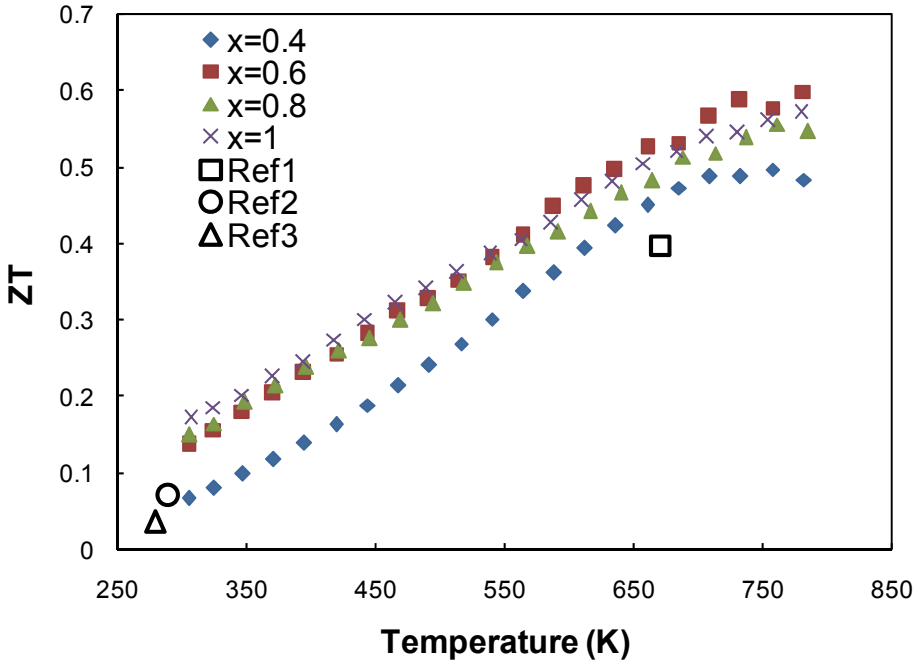

Figure 65 TE dimensionless figure of merit *ZT* as a function of temperature. Ref1 is the estimated highest ZT of $YbFe_4Sb_{12}$ by Kuznetsov et al[91]. Ref2 ($Yb_{0.8}Fe_4Sb_{12}$) and Ref3 ($Yb_{0.5}Fe_2Co_2Sb_{12}$) are near room temperature *ZT* reported by Bauer et al[94].

Figure 65 is the TE figure of merit *ZT* as a function of temperature. The maximum *ZT* was found to be 0.6 in sample x=0.6 at 782K as a result of a moderately high power factor and low thermal conductivity. Sample x=1 exhibits the next highest *ZT* of 0.57. Such *ZT* values, although lower than observed in the Ce filled p-type skutterudites[95], are much higher than previously reported *ZT* of 0.4 in $YbFe_4Sb_{12}$.[91] The room temperature *ZT* s for our x=0.6 and x=0.8 samples also double the values reported by others in materials of similar compositions[94]. We believe that this difference is primarily due to the lower resistivity of our samples, which is a consequence of the minimization of impurities and defects during the synthesis process.

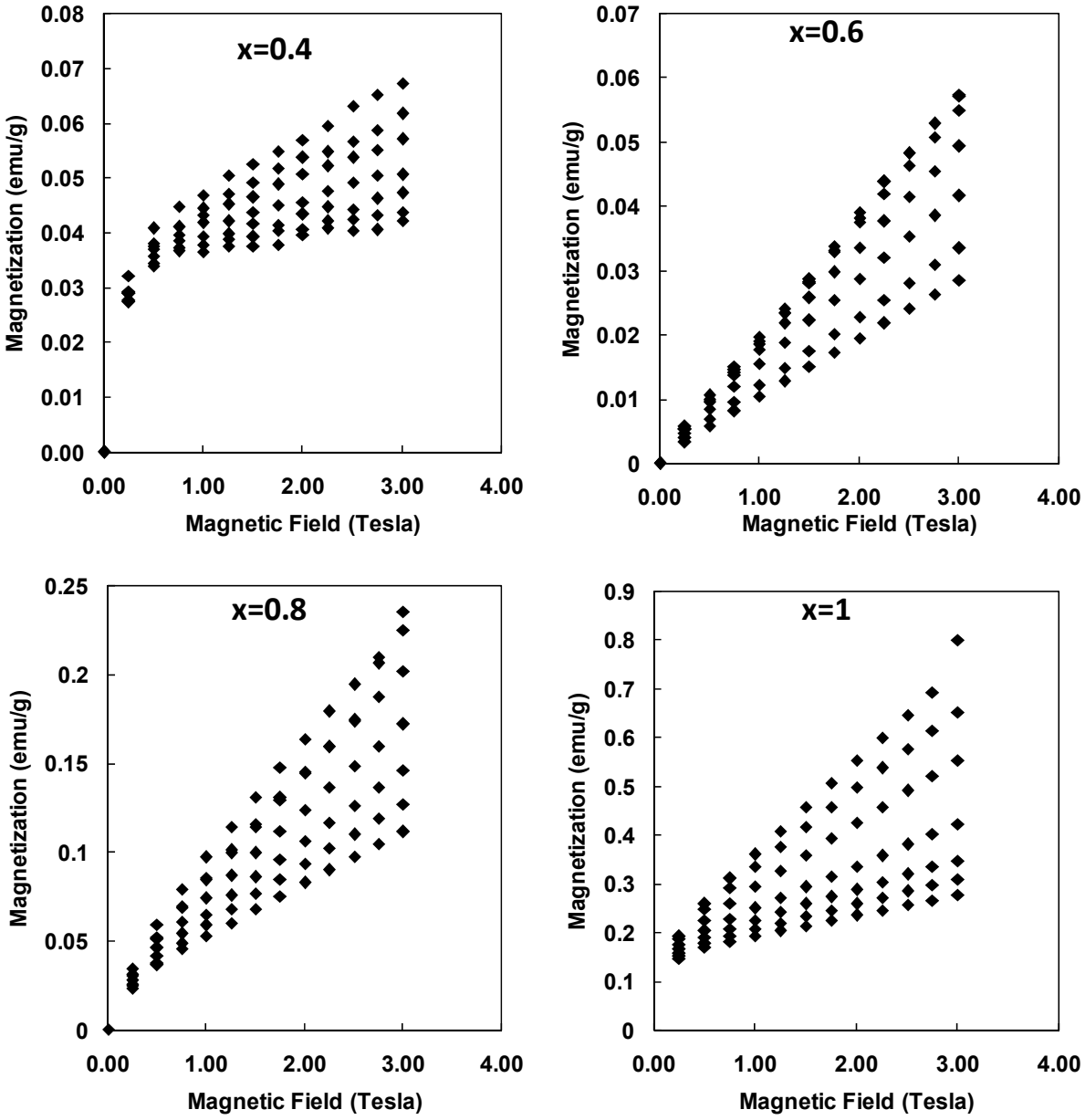

Figure 66 Magnetization of $Yb_xFe_yCo_{4-y}Sb_{12}$ for sample x=0.4, x=0.6, x=0.8 and x=1 at 60K, 80K, 100K, 150K, 200K, 250K and 300K.

The magnetizations for all samples are shown in Figure 66. The total magnetization consists of the following three parts: diamagnetic contribution M_{dia}, paramagnetic contribution M_{para}, and ferromagnetic contribution M_{ferro}. M_{dia} is linear in applied field and independent of

$$M = M_{dia} + M_{para} + M_{ferro} \quad (64)$$

temperature. M_{para} arises from the Yb filling and Fe substitution for Co. M_{ferro} comes from the Fe impurity and saturates at low magnetic fields below 1T. The different temperature and field dependence allows one to separate these three contributions. From the linear slope at high magnetic field (>1T), we estimate the susceptibility χ which includes both contributions from M_{dia} and M_{para}. Susceptibility χ follows the Curie-Weiss law given by Equation 65, where χ_0 is the diamagnetic contribution to the susceptibility and C is the Curie constant. The high

$$\chi = \chi_0 + \frac{C}{T} \quad (65)$$

temperature slope of χT vs T (shown in Figure 67) gives the value of χ_0. Subsequently, C is determined from the slop of $1/(\chi-\chi_0)$ vs T (shown in Figure 68). The effective moment μ_{eff} of each formula unit (Yb and Fe) can be obtained from Curie constant C by using Equation 66 where k is the Boltzmann constant, N_A is the Avogadro's number, μ_B is the Bohr magneton. Table 4 lists μ_{eff} together with other room temperature physical properties for all samples.

$$\mu_{eff} = \sqrt{\frac{3kC}{N_A \mu_B}} \quad (66)$$

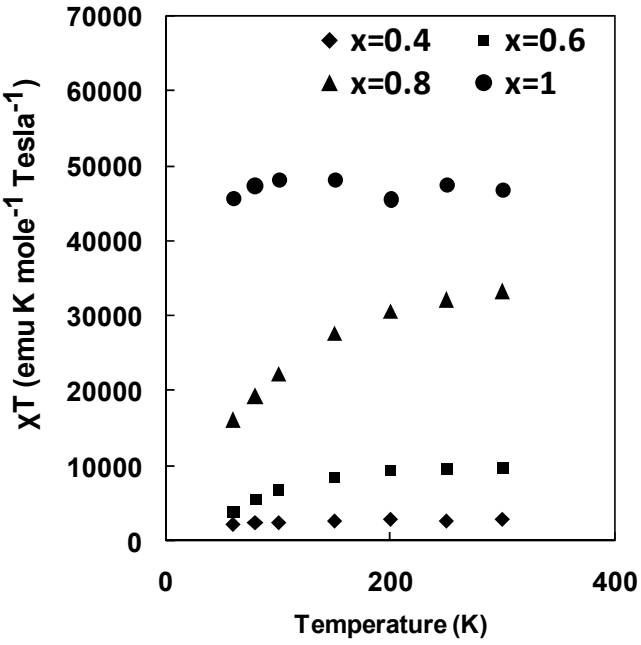

Figure 67 χT vs T

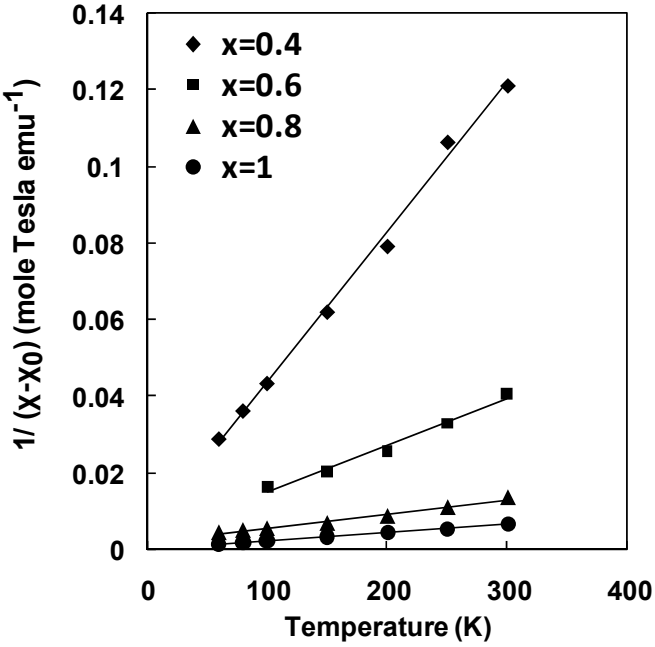

Figure 68 $1/(\chi - \chi_{0})$ vs T

Sample ID	x=0.4	x=0.6	x=0.8	x=1
Nominal composition	$Yb_{0.4}FeCo_3Sb_{12}$	$Yb_{0.6}Fe_2Co_2Sb_{12}$	$Yb_{0.8}Fe_3CoSb_{12}$	$YbFe_4Sb_{12}$
Estimated No. of carrier per formula unit	-0.2~0.2	0.2~0.8	0.6~1.4	1~2
Observed No. of carrier per formula unit	0.06	0.235	0.325	0.84
Carrier density at 300K ($\times 10^{20}$ cm^{-3})	1.479	6.03	8.54	21.5
Carrier mobility at 300K (cm^2 V^{-1} s^{-1})	28.95	14	17.3	9.53
μ_{eff}/ formula unit	0.714	1.285	2.318	3.064
Density (g cm^{-3})	7.512	7.635	7.927	7.895

Table 4 Some physical properties of Yb filled Fe compensated p-type skutterudite sample $Yb_xFe_yCo_{4-y}Sb_{12}$ at room temperature. The lower and upper boundaries of estimated number of carrier/formula unit are calculated assuming a variant Yb valence of +2 and +3. Minus sign in estimated number of carrier/formula unit indicates the major carrier is electron.

5.3 Summary of the chapter

We have systematically investigated the high temperature TE transport properties of p-type Yb-filled Fe-compensated skutterudite $Yb_xFe_yCo_{4-y}Sb_{12}$. With the aid of a graphite crucible during synthesis, we are able to obtain high quality ingots with excellent reproducibility. The lattice thermal conductivity is significantly reduced to the level near the theoretical limit upon Yb filling. Fe substitution for Co also depresses the lattice thermal conductivity through additional phonon scattering mechanisms. The highest ZT_{max} is 0.6 in sample x=0.6 at 782K. *ZT*s for other samples have also been significantly enhanced compared to published results on similar compositions. *ZT*s in high Yb filling fraction samples (x=0.8 and x=1) failed to exceed

that of Ce filled skutterudites due to the high electronic thermal conductivity κ_e, which, in the case of $YbFe_4Sb_{12}$, accounts for 67% of the total thermal conductivity at room temperature and up to 80% at 780K. The effective moments were measured and results agree with the values reported in literature.[92]

Now that we have a well-characterized p-type skutterudite matrix material in hand, we study the effect of $FeSb_2$ nanoinclusions on the TE properties of this system.

Chapter 6 Thermoelectric Properties and Galvanomagnetic Properties of P-type Yb-filled Skutterudite Nanocomposites with $FeSb_2$ Nanoinclusions

In this chapter, we extend the work to Yb-filled p-type skutterudite nanocomposites with in-situ formed $FeSb_2$ as nanoinclusions. Such a composite configuration utilizes a new p-type matrix $Yb_yFe_xCo_{4-x}Sb_{12}$, which is analogous to $Ce_yFe_xCo_{4-x}Sb_{12}$ but its high temperature TE properties have only been systematically studied recently.[96] The $FeSb_2$ nanoinclusion is the most probable impurity phases found in Fe compensated p-type skutterudite. Thus $Yb_yFe_xCo_{4-x}Sb_{12}/zFeSb_2$ nanocomposites are thermodynamically favorable and stable. These nanocomposites can be easily synthesized by fine control of the starting stoichiometry and the subsequent heat treatment process. A series of samples covering a wide range of ytterbium filling and Fe/Co ratio have been systematically studied in order to reveal the influence of nanosized $FeSb_2$ on the overall TE properties of the bulk nanocomposites. By taking advantage of these naturally occurring $FeSb_2$ nanoparticles, we achieve a ZT_{max}=0.74 in $Yb_{0.6}Fe_2Co_2Sb_{12}$ /0.05$FeSb_2$ at 780K. We also measured the Nernst coefficient on the best performing group $Yb_{0.6}Fe_2Co_2Sb_{12}/xFeSb_2$ and apply the method of four coefficients to calculate the DOS effective mass and the carrier scattering parameter. We find that a larger effective mass induced by the presence of nanoparticles is the origin of the enhanced Seebeck coefficient.

6.1 Sample synthesis

A series of $Yb_yFe_xCo_{4-x}Sb_{12}/zFeSb_2$ samples have been synthesized with Yb filling fraction y=0.4, 0.5, 0.6, 0.7, 0.8, 0.9, 1. The Fe composition x changes according to x=5y-1. The nominal $FeSb_2$ content z is set at 0.05, 0.1, and 0.2 for each combination of Yb filling y and Fe composition x. Table 5 summarizes the sample denomination and nominal chemical composition.

Pure element starting materials of Yb (pieces 99.9%), Fe (powder 99%), Co (powder 99.5%), and Sb (shot 99.999%) were weighed according to the stoichiometric ratio, and placed inside graphite crucibles. The graphite crucibles loaded with reactants were sealed under a vacuum of 10^{-5} Torr inside quartz ampoules. The sealed ampoules were heated to 1373K at a rate slower than 0.5K/min and held at that temperature for 6 hours before rapid quenching in a cold water bath. The quenched samples were annealed at 923K for another 3 days to promote homogeneity. The annealed ingots were ball milled into fine powders and hot pressed at 873K for 15min. The densities of all hot pressed samples are above 95% of the theoretical density.

The sample geometries, and measurement techniques are the same as those described in previous chapters. High temperature Seebeck coefficient and electrical resistivity (from room temperature to 800K) were measured on all samples in an ULVAC ZEM-3 system. The same rectangular bar sample was also used to measure the Nernst coefficient from 110K to 350K under a magnetic field from -2.2T to 2.2T in a homemade device. Nernst coefficient measurement were performed on the group of samples with Yb filling y=0.6. X-ray diffractions were performed on all samples to confirm the phase constitution. The thermal conductivity and Hall coefficient measurement were performed on selected sample groups of our interest.

Sample ID	Nominal chemical composition
12.4 0.4R	Yb0.4FeCo3Sb12
14.18 0.4R 0.05FS2	Yb0.4FeCo3Sb12/0.05FeSb2
14.9 0.4R 0.1FS2	Yb0.4FeCo3Sb12/0.1FeSb2
14.10 0.4R0.2FS2	Yb0.4FeCo3Sb12/0.2FeSb2
14.11 0.4R0.3FS2	Yb0.4FeCo3Sb12/0.3FeSb3
14.3 0.5R	Yb0.5Fe1.5Co2.5Sb12
14.12 0.5R 0.05FS2	Yb0.5Fe1.5Co2.5Sb12/0.05FeSb2
14.13 0.5R 0.1FS2	Yb0.5Fe1.5Co2.5Sb12/0.1FeSb2
14.14 0.5R0.2FS2	Yb0.5Fe1.5Co2.5Sb12/0.2FeSb2
12.5 0.6R	Yb0.6Fe2Co2Sb12
12.10 0.6R0.05FS2(1)	Yb0.6Fe2Co2Sb12/0.05FeSb2
13.9 0.6R0.05FS2(2)	Yb0.6Fe2.05Co2Sb12
12.11 0.6R0.1FS2	Yb0.6Fe2Co2Sb12/0.1FeSb2
12.12 0.6R0.2FS2	Yb0.6Fe2Co2Sb12/0.2FeSb2
12.9 0.7R	Yb0.7Fe2.5Co1.5Sb12
12.13 0.7R0.05FS2	Yb0.7Fe2.5Co1.5Sb12/0.05FeSb2
12.14 0.7R0.1FS2	Yb0.7Fe2.5Co1.5Sb12/0.1FeSb2
12.15 0.7R0.2FS2	Yb0.7Fe2.5Co1.5Sb12/0.2FeSb2
12.6 0.8R	Yb0.8Fe3CoSb12
12.16 0.8R0.05FS2	Yb0.8Fe3CoSb12/0.05FeSb2
12.17 0.8R0.1FS2	Yb0.8Fe3CoSb12/0.1FeSb2
12.18 0.8R0.2FS2	Yb0.8Fe3CoSb12/0.2FeSb2
12.8 0.9R	Yb0.9Fe3.5Co0.5Sb12
12.19 0.9R0.05FS2	Yb0.9Fe3.5Co0.5Sb12/0.05FeSb2
12.20 0.9R0.1FS2	Yb0.9Fe3.5Co0.5Sb12/0.1FeSb2
12.21 0.9R0.2FS2	Yb0.9Fe3.5Co0.5Sb12/0.2FeSb2
12.7 1R	YbFe4Sb12
12.22 1R0.05FS2	YbFe4Sb12/0.05FeSb2
12.23 1R0.1FS2	YbFe4Sb12/0.1FeSb2
12.24 1R0.2FS2	YbFe4Sb12/0.2FeSb2

Table 5 Sample ID and nominal chemical composition for $Yb_yFe_xCo_{4-x}Sb_{12}/zFeSb_2$ included in this study.

6.2 Results

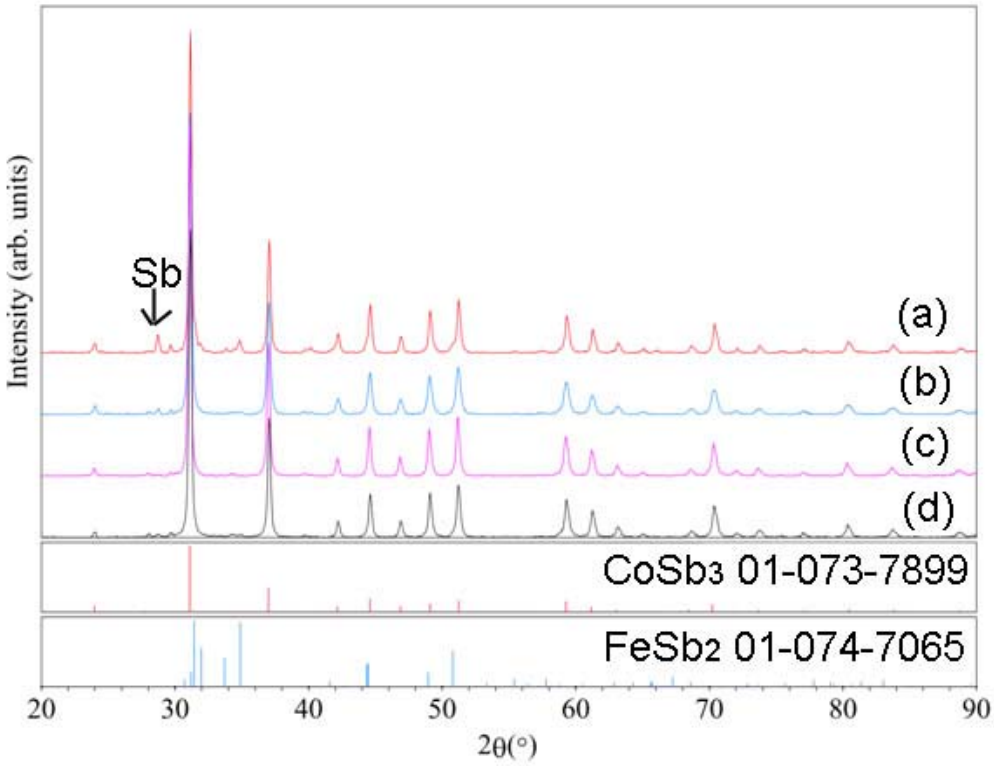

Figure 69 X-ray diffraction of $Yb_{0.6}Fe_2Co_2Sb_{12}/zFeSb_2$ (a) 12.12 0.6R 0.2FS2 (b) 12.11 0.6R 0.1FS2 (c) 12.10 0.6R 0.05FS2 (d) 12.5 0.6R. Trace antimony was also observed in (a)

Figure 69 is the x-ray diffraction of $Yb_{0.6}Fe_2Co_2Sb_{12}/zFeSb_2$ where skutterudite phase is found to be the primary phase for all sample. The impurity phase $FeSb_2$ was observed together with trace amount of Sb impurity. Figure 70 is the zoomed in x-ray diffraction of two $Yb_{0.6}Fe_2Co_2Sb_{12}/0.1FeSb_2$ samples synthesized under the same condition where $FeSb_2$ phase could be identified at multiple positions. The $CoSb_2$ which is isostructural with $FeSb_2$ and Sb were also observed.

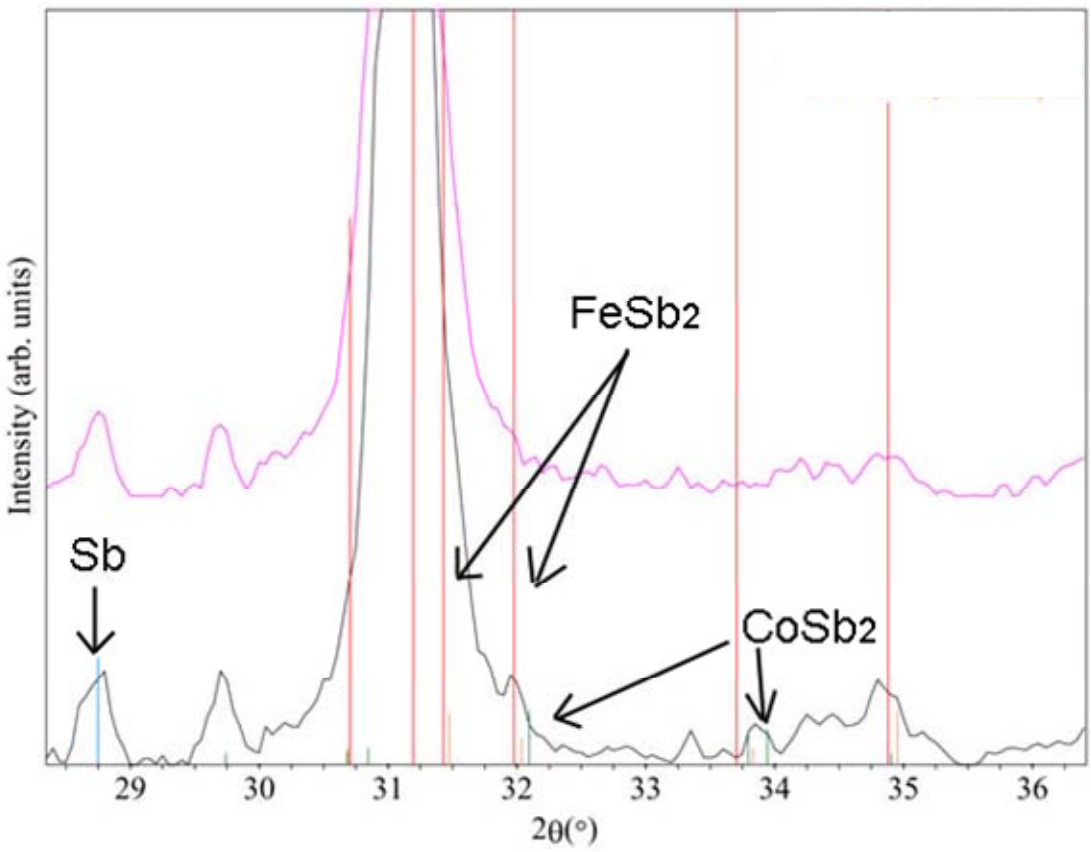

Figure 70 Zoomed in x-ray diffraction of two $Yb_{0.6}Fe_2Co_2Sb_{12}/0.1FeSb_2$ samples synthesized under the same condition. The major impurity phase is $FeSb_2$ while another closely related $CoSb_2$ and some Sb is also observed.

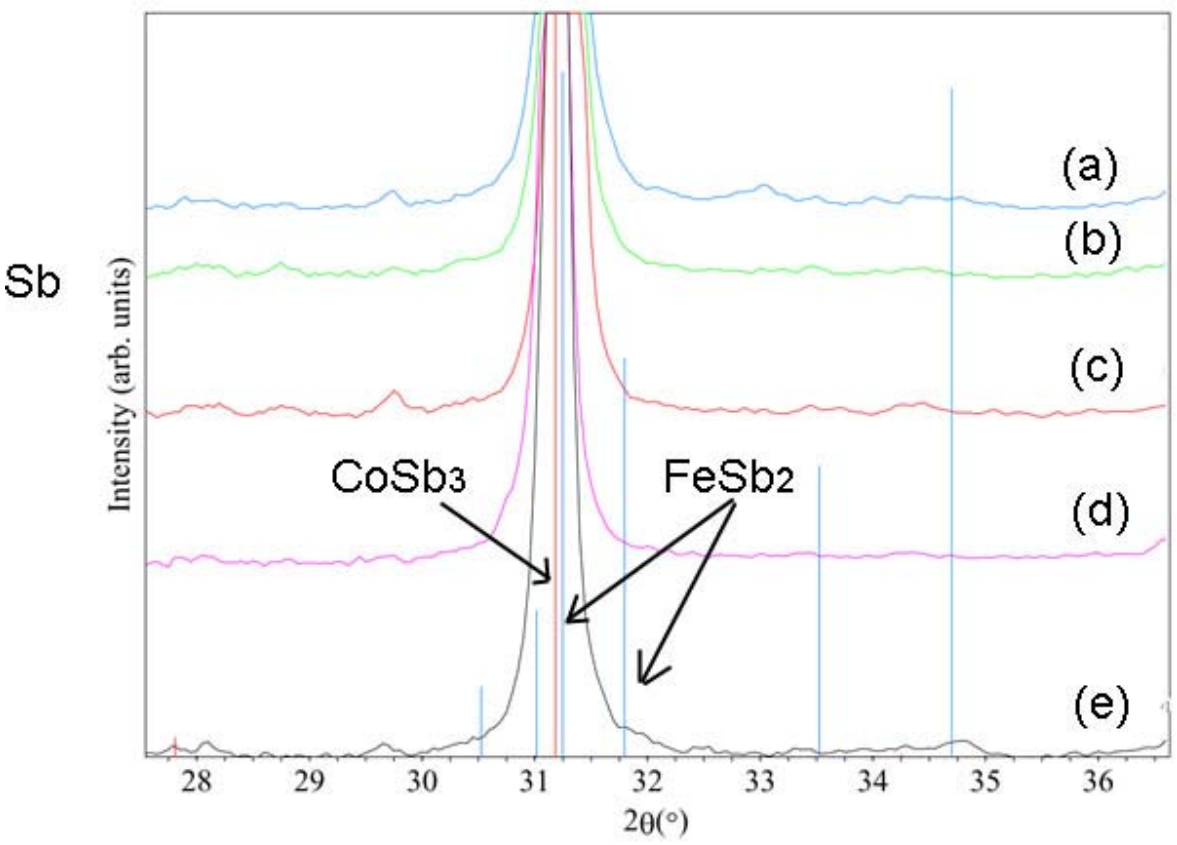

Figure 71 Zoomed in x-ray diffraction of $Yb_{0.4}FeCo_3Sb_{12}/zFeSb_2$ (a) 12.4 0.4R (b) 14.9 0.4R 0.1FS2 (c) 14.18 0.4R0.05FS2 (d) 14.10 0.4R 0.2FS2 (e) 14.11 0.4R 0.3FS2. The expansion of the primary skutterudite peak around 31 degree 2θ indicates the existence of $FeSb_2$.

Figure 71 is the zoomed in x-ray diffraction of $Yb_{0.4}FeCo_3Sb_{12}/zFeSb_2$. The most apparent indicator for $FeSb_2$ is the expansion of the primary skutterudites peak near 31 degree 2θ. X-ray diffractions of other Yb filling group show the similar results. Figure 72 shows high resolution SEM images taken on the fractured surface of sample 13.9 0.6R0.05FS2(2). We estimate the nanoparticle size to be about 20-40 nm based on Figure 2(b). From the results of our

previous work,[97] x-ray analysis and electron dispersive spectrum analysis, we believe the majority of nanoparticles present in Figure 72(d) are $FeSb_2$.

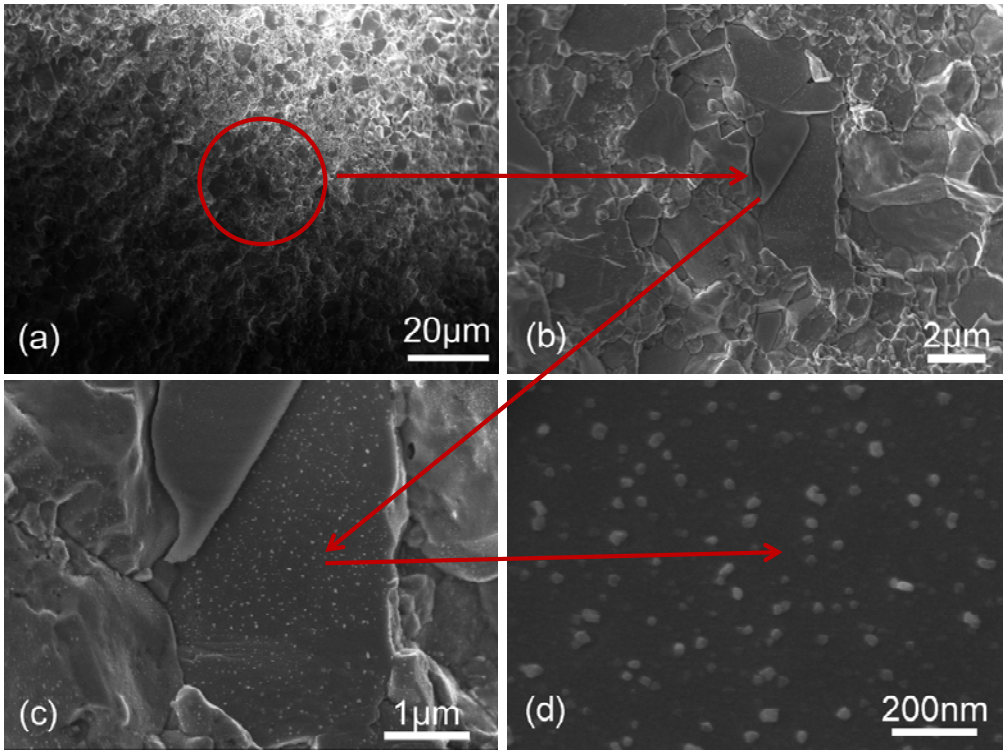

Figure 72 FESEM images on the fractured surface of sample 13.9 0.6R0.05FS2(1) which demonstrate the existence of $FeSb_2$ nanoparticle. Images from (a) to (d) are in increasing magnification.

Figure 73 (a)-(g) show the power factors as a function of temperature for the nanocomposite samples and control samples synthesized in compositions listed in Table 5. The materials are grouped based on the Yb filling ratio "y". Generally, nanocomposite samples exhibit enhanced power factors when $y \leq 0.7$ as shown from (a) to (d). Once $y > 0.7$, most nanocomposite samples show comparable or smaller power factors compared to control samples as shown from (e) to (g).

Figure 73 Power factors as a function of temperature.

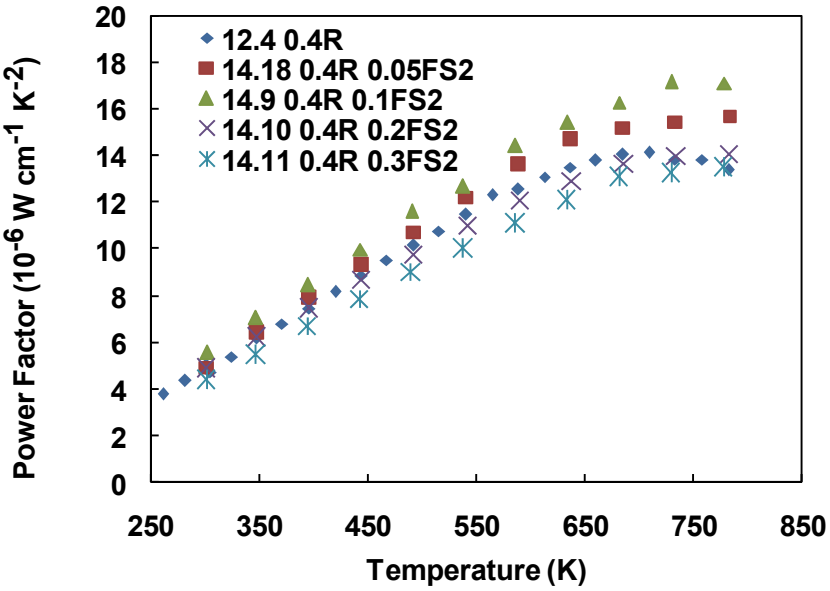

(a)

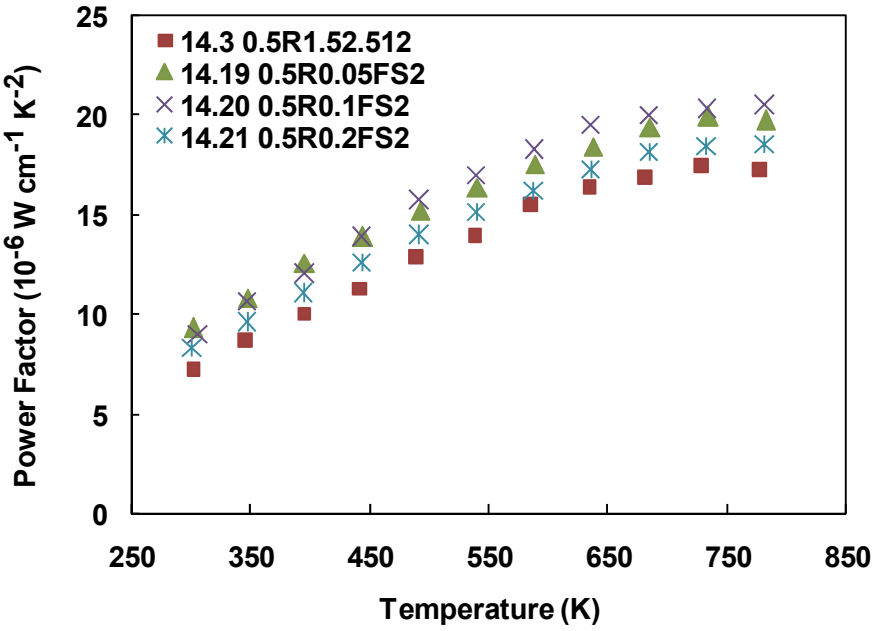

(b)

Figure 73 continued

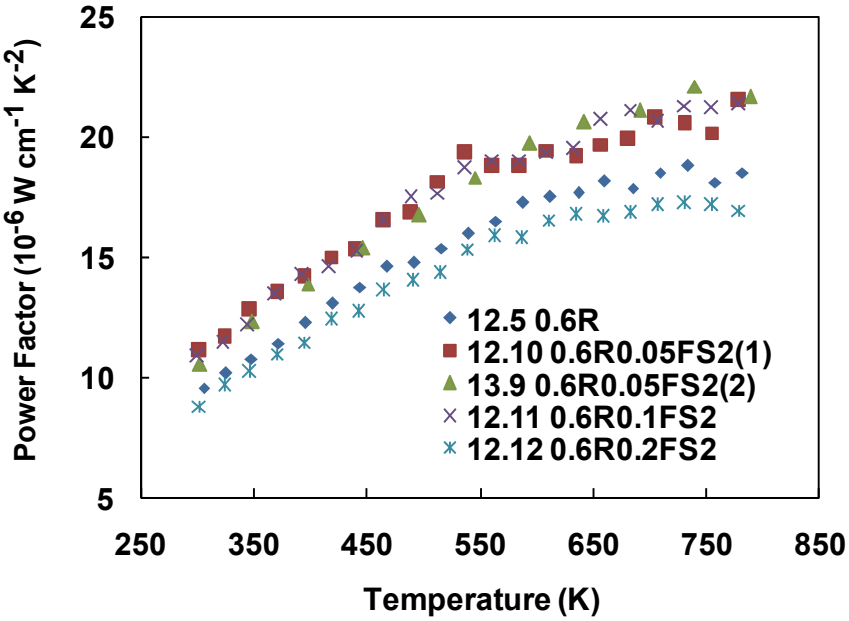

(c)

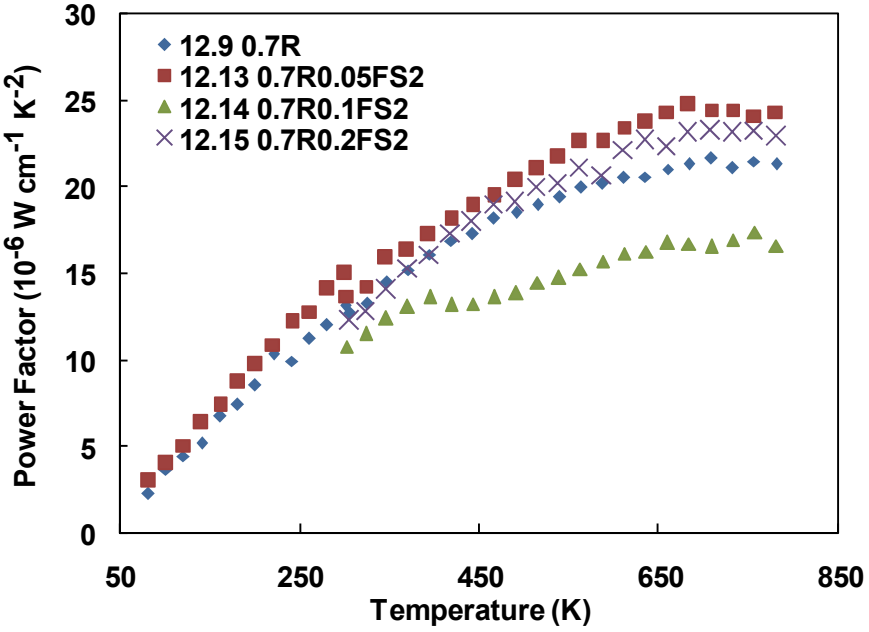

(d)

Figure 73 continued

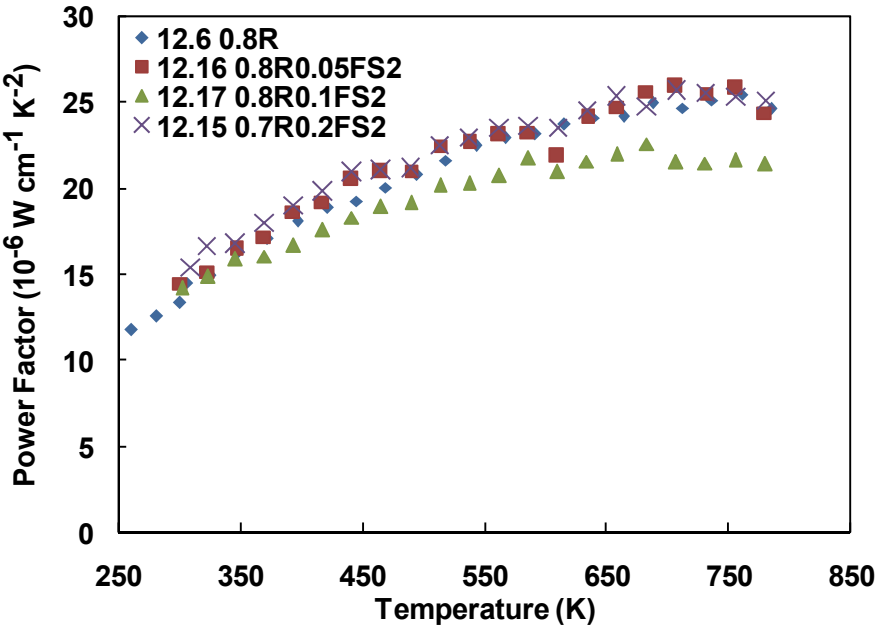

(e)

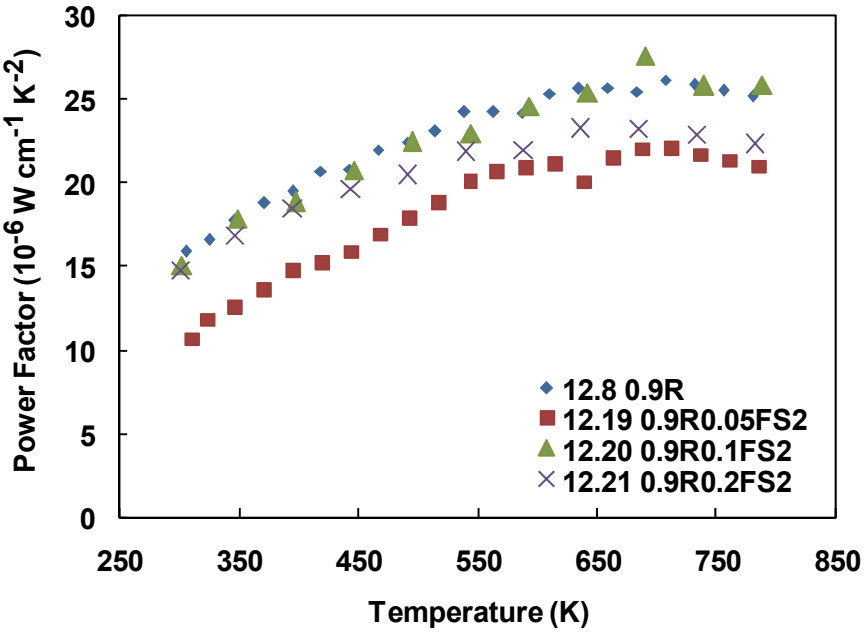

(f)

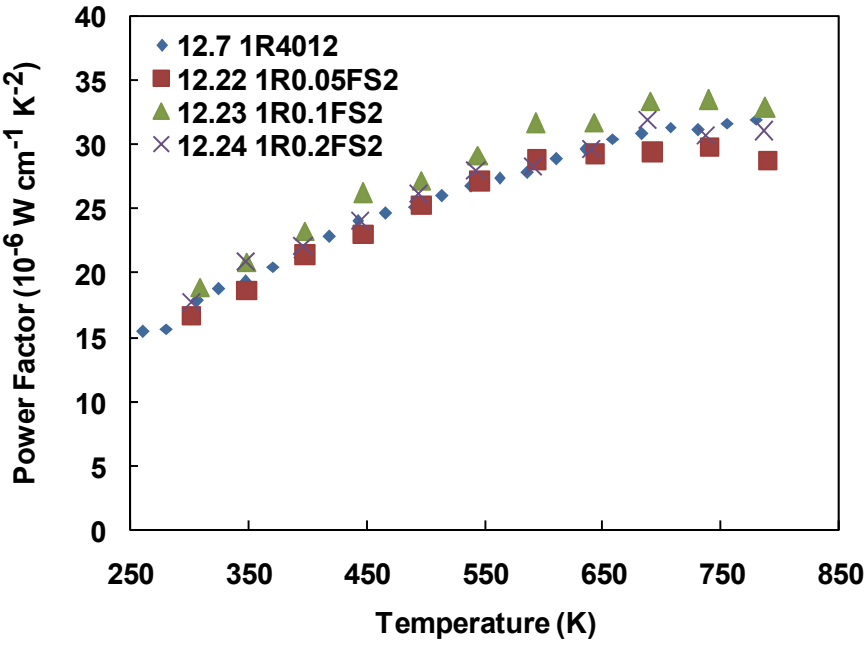

(g)

Figure 73 Power factors of nanocomposite samples and control samples as a function of temperature. The samples are grouped according to the Yb filling ratio "y" (a) y=0.4; (b) y=0.5; (c) y=0.6; (d) y=0.7; (e) y=0.8; (f) y=0.9; (g) y=1. Generally, nanocomposite samples could exhibit enhanced power factors when y≤0.7 as shown from (a) to (d). Once y>0.7, most nanocomposite samples show comparable or smaller power factors compared to control samples as shown from (e) to (g).

To seek the highest possible ZT and investigate the physical mechanisms for the enhanced electronic properties in some of the nanocomposites, we focus on characterizing the full TE transport properties, galvanomagnetic properties and applying the method of four coefficients on the group with Yb filling ratio y=0.6. To further simplify our discussion, we use the nominal $FeSb_2$ content x to denote our samples. Sample x=0 with no intentionally added $FeSb_2$ serves as a control sample. Sample x=0.05(2) which is of identical composition of

Sample ID	Corresponding notation in Figure 70 (c)	Nominal composition	Density (g cm^{-3})	Seebeck coefficient (μV/K)	Carrier density (10^{20} cm^{-3})
x=0	12.5 0.6R	$Yb_{0.6}Fe_2Co_2Sb_{12}$	7.635	87.67	6.03
x=0.05(1)	12.10 0.6R0.05FS2(1)	$Yb_{0.6}Fe_2Co_2Sb_{12}/0.05FeSb_2$	7.525	94.55	15.6
x=0.05(2)	13.9 0.6R0.05FS(2)	$Yb_{0.6}Fe_{2.05}Co_2Sb_{12}$	7.791	89.73	12.8
x=0.1	12.110.6R0.1FS2	$Yb_{0.6}Fe_2Co_2Sb_{12}/0.1FeSb_2$	7.759	85.63	9
x=0.2	12.12 0.6R0.2FS2	$Yb_{0.6}Fe_2Co_2Sb_{12}/0.2FeSb_2$	7.788	75.36	3.83

Table 6 Some room temperature physical properties of $Yb_{0.6}Fe_2Co_2Sb_{12}/xFeSb_2$ samples

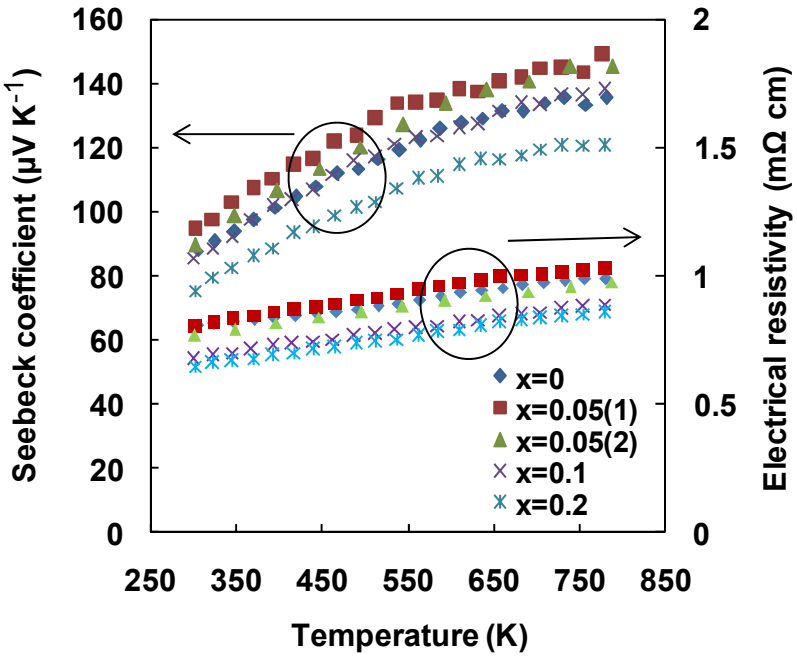

Figure 74 Seebeck coefficient and electronic resistivity as a function of temperature for $Yb_{0.6}Fe_2Co_2Sb_{12}/xFeSb_2$.

x=0.05(1) was used to reproduce and cross-check the transport properties of x=0.05(1). Table 6 lists some room temperature physical properties of the $Yb_{0.6}Fe_2Co_2Sb_{12}/xFeSb_2$ samples.

Figure 74 exhibits the Seebeck coefficient and electrical resistivity as a function of temperature. Seebeck coefficients for all samples increase monotonously as a function of temperature. Nanocomposite samples x=0.05(1), x=0.05(2) show consistent higher Seebeck coefficients over the whole temperature range compared to x=0. At 780K, x=0.05(1) has a Seebeck coefficient of 149μV/K, and x=0.05(2) has a Seebeck coefficient of 145 μV/K; while the Seebeck coefficient for x=0 is 138 μV/K. When the $FeSb_2$ content x>0.1, Seebeck coefficient deceases with an increasing x. Electrical resistivity for all samples exhibit a metallic behavior. x=0.05(1) and x=0.05(2) have electrical resistivity close to x=0 while x=0.1 and x=0.2 show lower resistivity values.

The temperature dependence of power factors is plotted in Figure 73 (c) [please refer to Table 6 for the corresponding notation in Figure 73 (c)]. Compared to x=0 at 780K, x=0.05(1) and x=0.05(2) show 17-19% power factor enhancement as a result of enhanced Seebeck coefficients; x=0.1 also shows a 15% enhancement due to the reduced electrical resistivity; while x=0.2 shows a reduction because of the greater influence from the reduced Seebeck coefficient.

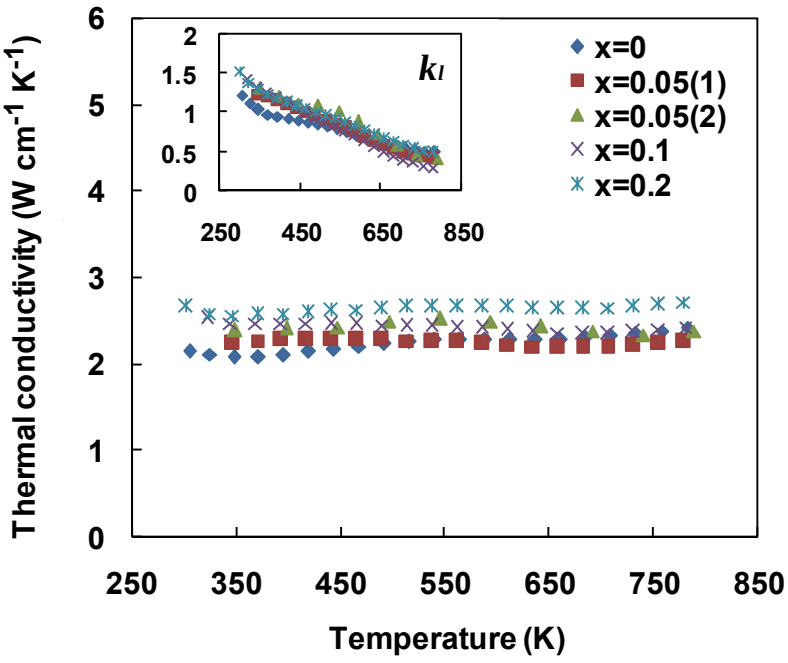

Figure 75 Temperature dependence of thermal conductivity for $Yb_{0.6}Fe_2Co_2Sb_{12}$/x$FeSb_2$. The inset graph displays the lattice thermal conductivity.

The thermal conductivity for all samples is insensitive to the temperature change as seen in Figure 75. To estimate the lattice thermal conductivity κ_l, we calculate the electronic thermal conductivity κ_e using Wiedemann Franz Law $\kappa_e = L\sigma T$, where L is the Lorenz number, σ the electrical conductivity and T temperature, and subtract κ_e from total thermal conductivity κ. Here, we assume $L = 2.44\times10^{-8}$ W Ω K^{-2}, a value that is suitable for degenerate semiconductors. Lattice thermal conductivities for all samples (inset of Figure 75) decrease with increasing temperature and do not show much deviation from each other. κ_l for nanocomposite samples except x=0.2, are slightly reduced compared to x=0 at higher temperature. As pointed out in our previous work,[96] κ_l for x=0 is 0.49 $Wm^{-1}K^{-1}$ at 780K, which is already very close to the theoretical

limit of 0.2 $Wm^{-1}K^{-1}$ we calculated assuming a mean free path equal to lattice spacing. So the weak reduction of κ_l in nanocomposite samples suggests that the opportunity for further lattice thermal conductivity reduction by nanostructuring is very limited. On the other hand, κ_e for x=0.1 and x=0.2 is greater than that of x=0, which negates the benefit from lattice thermal conductivity reduction if there is any. As a result, x=0.1 has a thermal conductivity similar to that of x=0, and x=0.2 has an even larger thermal conductivity.

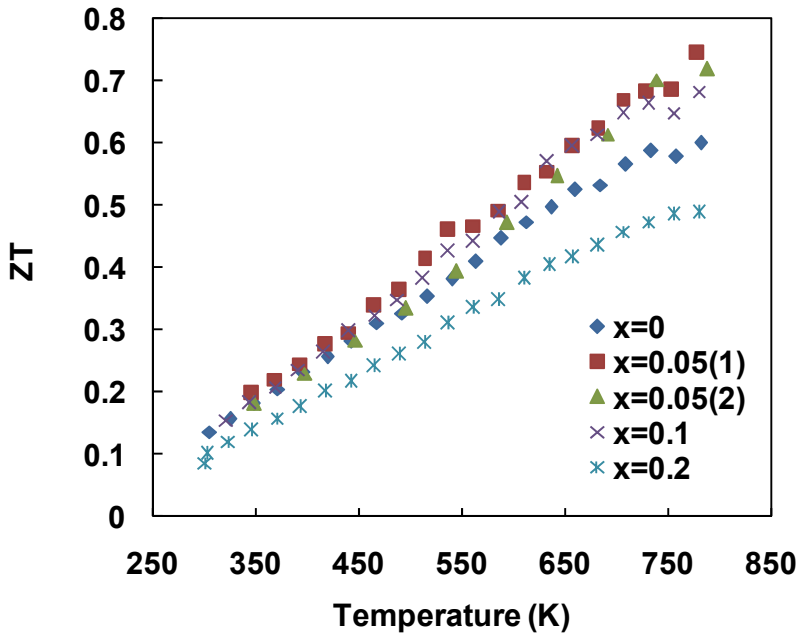

Figure 76 *ZT* as a function of temperature for $Yb_{0.6}Fe_2Co_2Sb_{12}/xFeSb_2$.

Figure 76 displays the *ZT* as a function of temperature. As a result of an enhanced power factor, x=0.05(1), x=0.05(2) and x=0.1 all demonstrate a higher ZT_{max} of 0.74, 0.72 and 0.68 respectively at 780K compared to ZT_{max}=0.6 of x=0.

6.3 Discussion

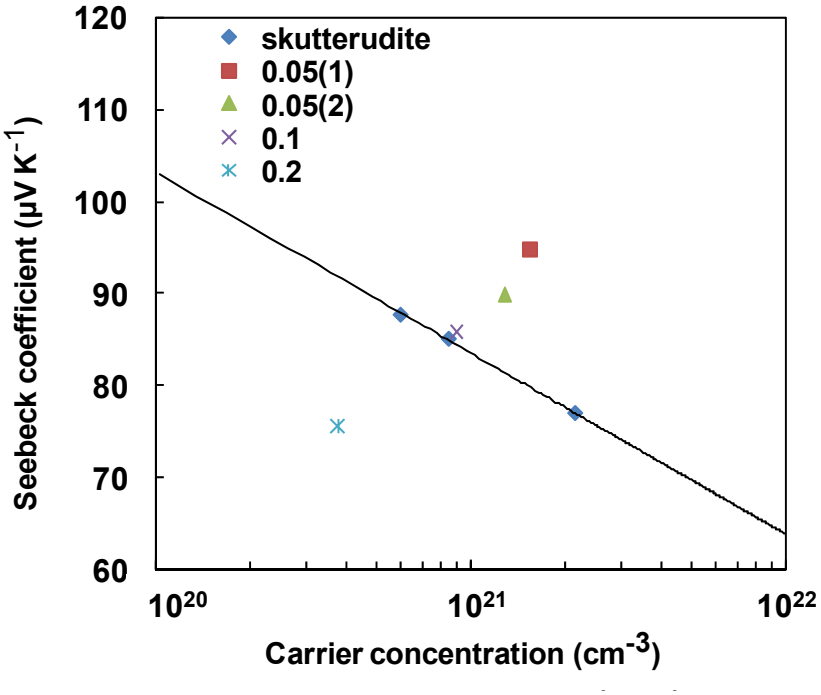

Figure 77 Pisarenko relation of nanocomposites and regular skutterudite samples at room temperature. Blue diamond (skutterudite) points represent regular skutterudite samples of various carrier concentrations prepared in our lab. The fit line serves as an aid to the eye.

As shown in Figure 74, x=0.05(1) and x=0.05(2) show enhanced Seebeck coefficients compared to x=0. x=0.1 has identical Seebeck coefficient but a lower electrical resistivity than x=0, which could be perceived as an equivalent of an increase in the Seebeck coefficient. To explain the mechanism for such an enhancement, we plot the room temperature Seebeck coefficient as a function of carrier concentration, known as the "Pisarenko relation",[36] in Figure 77. For a semiconductor with only one type carrier, Seebeck coefficient can be expressed as[36]

$$S = \frac{k}{e}\left(s + 2 + \ln \frac{2\left(2\pi m^* kT\right)}{h^3 n} \right) \qquad 67$$

where, s is the carrier scattering parameter, m^* the density of state effective mass, and n the carrier concentration. For bulk semiconductors with similar composition, s and m^* usually have comparable values, thus the Seebeck coefficient is proportional to the logarithm of inverse carrier concentration. This is exactly the case for the regular skutterudite samples shown in Figure 74, where samples obey a linear relation as suggested in Equation 67. Nanocomposite samples x=0.05(1) and x=0.05(2) show higher Seebeck coefficients than those projected by the fit.

To understand the effects of nanostructuring on s and m^*, we use four measured transport properties, namely Seebeck coefficient S, the electrical conductivity σ, the Nernst coefficient N, and Hall coefficient R_H to directly calculate the scattering parameter s, and the density of state effective mass m^*. The derivation of equations is provided below following Heremans *et al*'s work.[21, 51, 98] $\gamma(E)$ describes the non-parabolic energy of carriers given by Equation 68, where E_g is the bandgap.

$$\gamma(E) = \frac{\hbar^2 k^2}{2m_v^*} = E\left(1 + \frac{E}{E_g}\right)$$
$$\gamma' = 1 + 2\frac{E}{E_g} \qquad 68$$
$$\gamma'' = \frac{2}{E_g}$$

The carrier concentration, carrier mobility, Seebeck coefficient and Nernst coefficient can be expressed by Equation 69-72.

$$n(p) = \frac{\left[2m^*(E=0)\gamma(E)\right]^{3/2}}{3\pi^2\hbar^3} \approx \frac{1}{R_H e} \qquad 69$$

$$\mu = R_H \sigma = \frac{\sigma}{n(p)e} \tag{70}$$

$$S = \pm \frac{\pi^2}{3} \frac{k}{e} kT \left[(s+1) \frac{\gamma''}{\gamma} - 2 \frac{\gamma''}{\gamma'} \right] \tag{71}$$

$$N = \mu \frac{\pi^2}{3} \frac{k}{e} kT \left[\left(s - \frac{1}{2} \right) \frac{\gamma'}{\gamma} - 2 \frac{\gamma''}{\gamma'} \right] \tag{72}$$

These equations can be fitted by using mathematical software or solved explicitly as a function of measured parameters to yield Fermi energy E_F, scattering parameter s and DOS effective mass $m^*(E_F)$ from Equation 73-75.

$$E_F = \frac{E_g}{2} \frac{\left(-A + \frac{\pi^2 k^2 T}{eE_g} \right) + \sqrt{\left(A - \frac{\pi^2 k^2 T}{eE_g} \right)^2 + 2 \frac{\pi^2 k^2 T}{eE_g} A}}{A}, \quad A = S - \frac{N}{\mu} \tag{73}$$

$$s = \frac{1}{2} + \left(\frac{\frac{3N}{\mu E_g \frac{\pi^2 k^2 T}{eE_g}} + \frac{4}{E_g + 2E_F}}{1 + 2\frac{E_F}{E_g}} \right) E_F \left(1 + \frac{E_F}{E_g} \right) \tag{74}$$

$$m^*(E_F) = m^*(E=0) \gamma'(E_F) \tag{75}$$

In this study, we use the non-parabolic band model described by Equation 65, which has been used to study the band structure of $CoSb_3$.[99-101] The band gap E_g=0.5eV is adapted from literature on $YbFe_4Sb_{12}$.[102, 103]

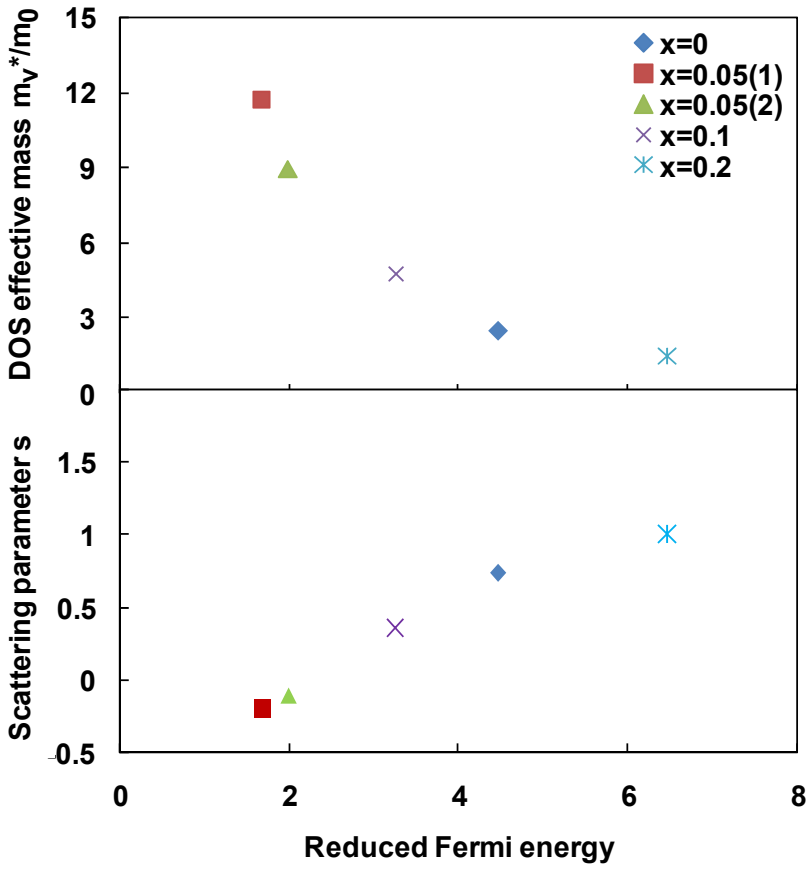

Figure 78 DOS effective mass m^* and carrier scattering parameter s as a function of reduced Fermi energy E_F.

It can be seen from Figure 78 that the DOS effective masses for x=0.05(1) and x=0.05(2) are 3 to 4 times greater than the effective mass for x=0. The large effective mass implies that the presence of nanoparticles could induce a localized sharp peak in the DOS that leads to enhanced Seebeck coefficients. The scattering parameter s, on the other hand, has changed from acoustic phonon scattering in x=0.05(1) and x=0.05(2) to neutral impurity scattering in x=0.1, and to mixed neutral and ionized impurity scattering in x=0.2. Matrix skutterudite x=0 also has an s indicating neutral impurity scattering. Thus, it is the effective mass rather than the scattering

parameter that results in an enhanced Seebeck coefficient, and hence, the power factor for our nanocomposite samples.

6.4 Summary of the chapter

In conclusion, we investigated the high temperature TE properties of p-type skutterudite nanocomposite $Yb_yFe_xCo_{4-x}Sb_{12}/zFeSb_2$. These nanocomposites can be easily formed in-situ during solidification via fine control of starting stoichiometry and subsequent heat treatment process. The presence of small amount of $FeSb_2$ nanoparticles can increase the power factors in a range of nanocomposites with Yb filling ratio $y \leq 0.7$ and $FeSb_2$ content $z \leq 0.1$.

We thoroughly characterized the full TE transport properties, galvanomagnetic properties and applied the method of four coefficients to calculate the scattering parameter *s* and DOS effective mass *m**. We found that an enhanced effective mass induced by the $FeSb_2$ nanoparticles is the driving force for the enhanced Seebeck coefficient, hence the enhanced electronic properties. The lattice thermal conductivity is slightly reduced in nanocomposites as well but the reduction is insignificant to cause a dramatic enhancement in *ZT* due to the near phonon glass lattice thermal conductivity in the matrix skutterudite. Sample x=0.05(1) demonstrated the highest ZT_{max}=0.74 at 780K which is 23% enhancement over the matrix x=0.

Chapter 7 Thermoelectric Properties of Double Filled P-type Skutterudite $Yb_yGa_zFe_xCo_{4-x}Sb_{12}$

In previous two chapters, we have seen that filled p-type skutterudites that exhibit high *ZT*s are generally very conductive, with an electrical resistivity typically below 1 mΩ cm. The lattice thermal conductivity, on the other hand, is very close to the theoretical minimum. This implies the room for further *ZT* enhancement by reducing the lattice thermal conductivity is very limited and the electronic thermal conductivity is a significant contribution to the total thermal conductivity, sometimes even exceeding 50%. Therefore it is important to seek new mechanisms on improving the Seebeck coefficient *S* because 1) the square power will amplify any gain from *S*; 2) increasing σ will also increase κ_e in the denominator which partially cancels out the gain.

$$ZT = \frac{S^2\sigma}{\kappa_l + \kappa_e}T = \frac{S^2\sigma}{\kappa_l + L\sigma T}T \Rightarrow S = \sqrt{\left(\frac{1}{T}\right)\left(LT + \rho\kappa_l\right)} \qquad 76$$

To explicitly show what a Seebeck coefficient is needed for certain lattice thermal conductivity and resistivity in order to get a *ZT*=1, we start from the definition of *ZT* and express the Seebeck coefficient *S* as a function of electrical resistivity ρ and lattice thermal conductivity κ_l as shown in Equation 76. If we assume *ZT* =1 at 800K and the Lorenz number $L=2.44\times10^{-8}$ $V^2\ K^{-2}$, we plot the projected Seebeck coefficient a function of electrical resistivity ρ and lattice thermal conductivity κ_l as shown in Figure 79(a). The cross section area at κ_l = 0.2W/mK shown in Figure 79(b) is used to identify the minimum Seebeck coefficients needed to attain a certain *ZT*. Taking *ZT* =1, for example, if we assume ρ=1 mΩ cm, then a *S* >164 μV/K is needed to achieve the goal.

(a)

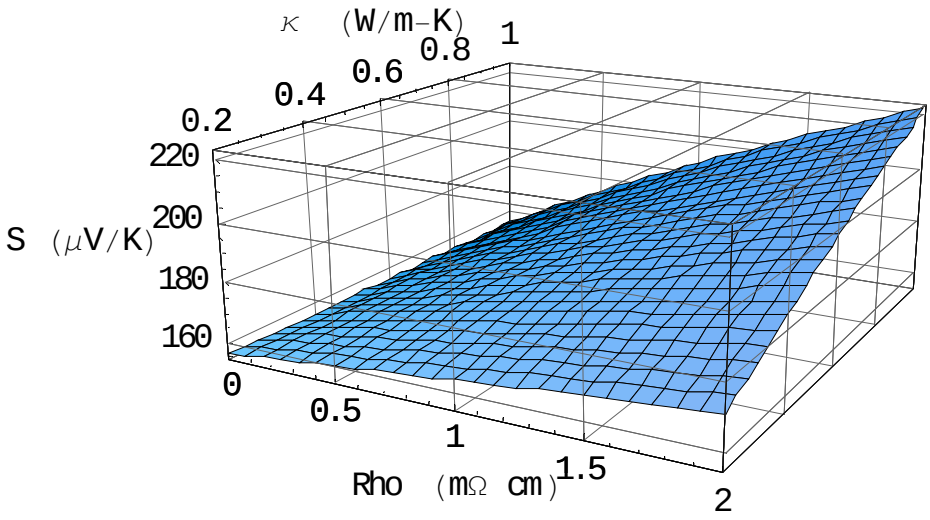

(b)

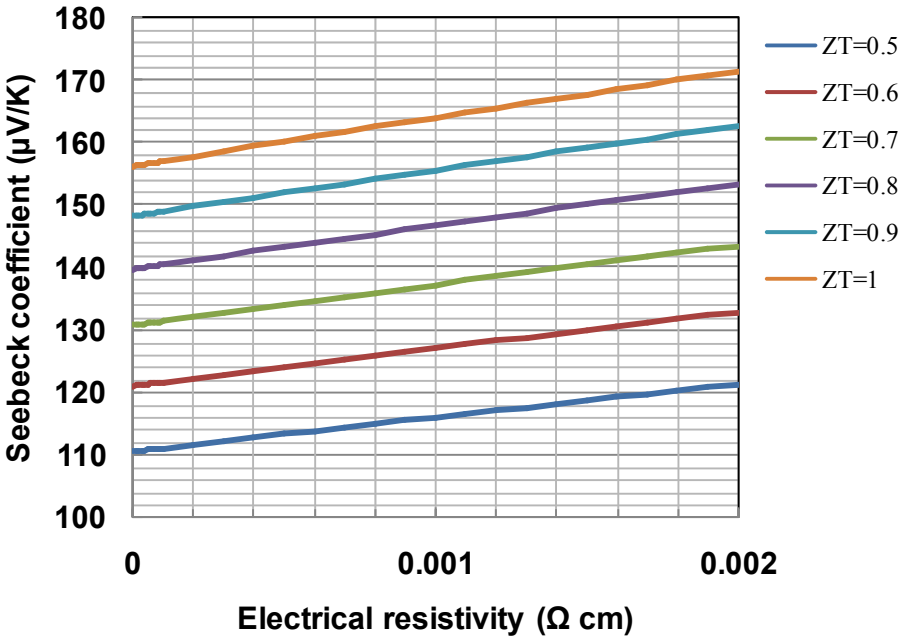

Figure 79 (a) 3D graph of the projected Seebeck coefficient S as a function of electrical resistivity ρ and lattice thermal conductivity κ_l. (b) Cross section of κ_l = 0.2W/mK from (a) which is used to identify the minimum Seebeck coefficient needed to attain certain ZT.

In this chapter, we report the high temperature thermoelectric properties of a new p-type double filled skutterudite $Yb_yGa_zFe_xCo_{4-x}Sb_{12}$. We choose Ga as the second filler atom because 1) theoretical calculation identified Ga and other group III elements In, Tl as impurities being able to induce a deep defect state in narrow band semiconductors;[104] 2) Ga has been reported as a filler atom for $CoSb_3$, although discrepancy of the exact filling fraction exists.[105, 106] We have also applied the method of four coefficients[48] to calculate the DOS effective mass m^* and carrier scattering parameter s, with the hope of elucidating the unconventional behavior of electronic properties observed in some samples.

7.1 Sample synthesis

Sample ID	Nominal composition	Density ($g\ cm^{-3}$)
Y60	$Yb_{0.6}Fe_2Co_2Sb_{12}$	7.635
Y60G10	$Yb_{0.6}Ga_{0.1}Fe_2Co_2Sb_{12}$	7.807
Y60G15	$Yb_{0.6}Ga_{0.15}Fe_2Co_2Sb_{12}$	7.726
Y60G20	$Yb_{0.6}Ga_{0.2}Fe_2Co_2Sb_{12}$	7.758
Y65	$Yb_{0.65}Fe_{1.5}Co_{2.5}Sb_{12}$	7.57

Table 7 Sample designation of double filled skutterudite $Yb_yGa_zFe_xCo_{4-x}Sb_{12}$.

High purity starting materials Yb (pieces 99.9%), Fe (powder 99%), Co (powder 99.5%), Sb (shot 99.999%), and Ga (pieces 99.999%) were used to synthesize the skutterudite ingots. The annealed ingots were pulverized into powders and consolidated by hot pressing. The details of

the synthesis can be found elsewhere.[96] A total of five samples have been prepared. Table 7 serves as a key to the sample designation. The first four samples are based on $Yb_{0.6}Fe_2Co_2Sb_{12}$ with a variant Ga filling fraction "z" ranging from 0 to 0.2. The fifth sample with a higher Yb filling fraction and lower Fe/Co ratio is used to probe the transport behavior at a lower carrier concentration.

7.2 Results

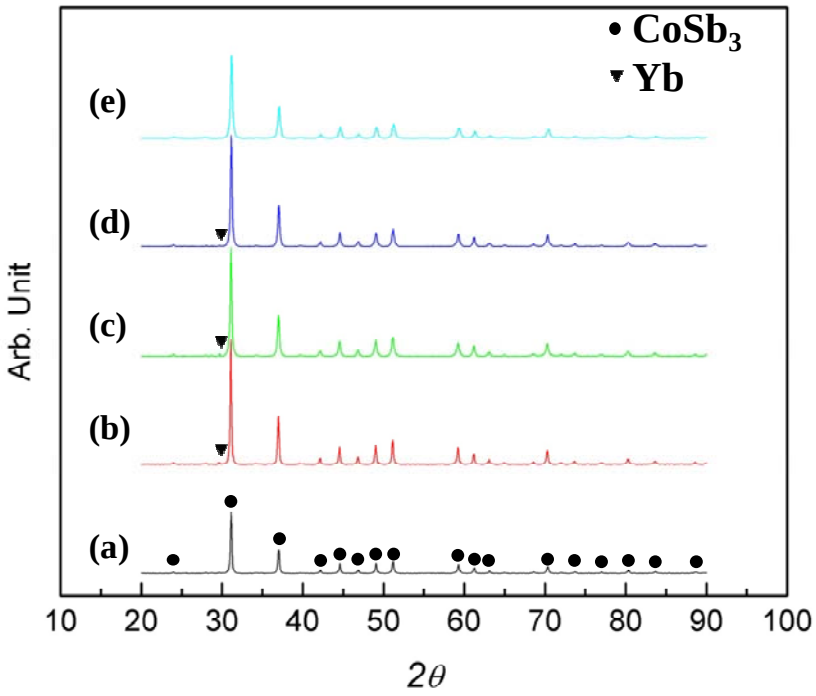

Figure 80 Powder x-ray diffraction patterns of samples included in the study. (a) Y60; (b) Y60G10; (c) Y60G15; (d) Y60G20; (e) Y65. The major peaks of all samples are indexed to the skutterudite phase $CoSb_3$ PDF# 01-073-7899. Trace amount of Sb phase can also be detected in (a) but unidentifiable in the graph. Trace amount of Yb can be found in (b), (c), and (d) and are labeled in the graph accordingly.

Figure 80 displays the powder x-ray diffraction patterns of samples listed in Table 7. Skutterudite phase was found to be the primary phase for all samples and the patterns match PDF# 01-073-7899. Trace amount of Sb can be detected by x-ray analysis software JADE in sample Y60, which is common for Sb based skutterudites. However the amount is so small that the intensity is closer to the background noise and unobservable in the figure. A trace amount of Yb can also be detected in sample Y60G10, Y60G15, and Y60G20.

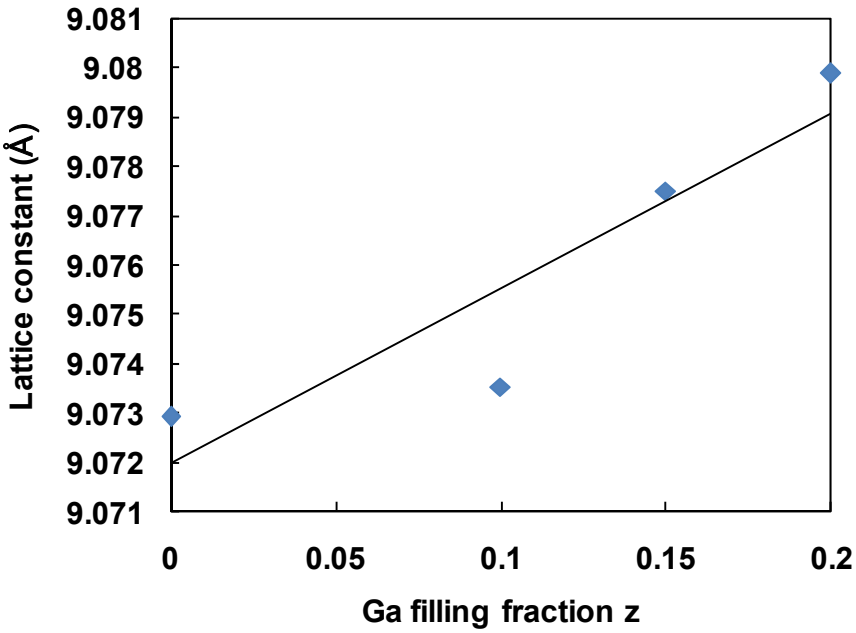

Figure 81 Lattice constant as a function of Ga filling fraction.

The filling fraction of Ga has been a matter of controversy in previous literature reports. Su et al reported that Ga filling could reach as high as x=0.22 in $Ga_xCo_4Sb_{12}$;[105] on the other hand Harnwunggmoung and co-workers reported a Ga filling fraction at a miniscule x=0.02.[106] The exact Ga filling fraction is out of the scope of this work and may be subject to change with the complexity of another filler element and Fe substitution on the Co site. We plot

the lattice constant as a function of Ga filling fraction z as shown in Figure 81 and our result agrees more with Su's work. We cannot clearly detect Ga and its compounds in x-ray, nor could we find the evidence in the EDS analysis. This suggests either we have successfully inserted Ga into the skutterudite cages up to z=0.2 or the Ga impurity phase is below the detection limit of our instruments considering that even the most Ga rich sample Y60G20 has a Ga concentration of only 1.2at%. Further evidences for Ga filling can be sought in the difference of transport properties.

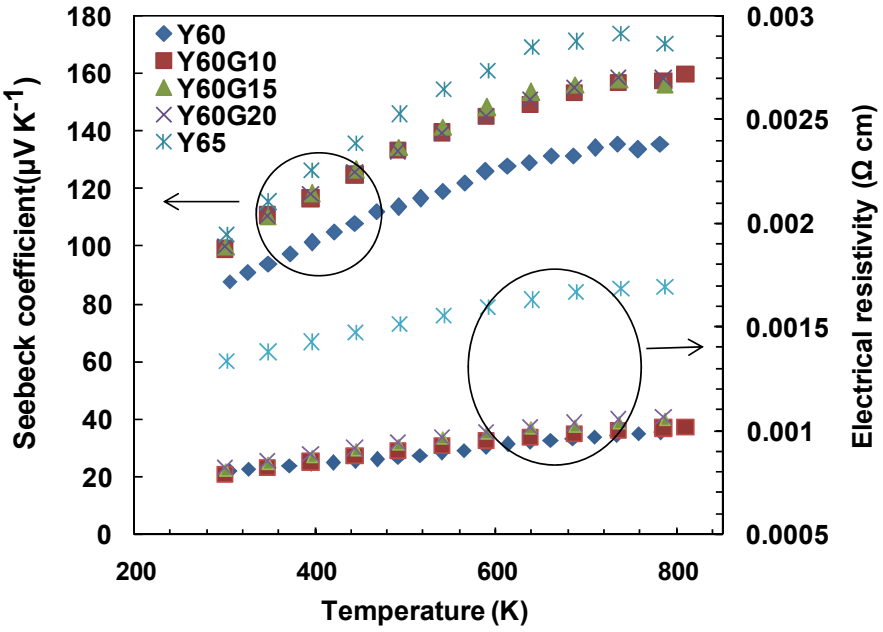

Figure 82 Temperature dependence of the Seebeck coefficient and the electrical resistivity.

Figure 82 displays the temperature dependence of the electronic properties. Seebeck coefficients for all samples exhibit the typical behavior for heavily doped semiconductors: increasing monotonously with the increasing temperature before reaching the intrinsic region. Sample Y65 has a higher Seebeck coefficient compared to Y60, which is what one would expect from a reduced carrier concentration due to the combined effects of a higher Yb filling fraction

and a lower Fe/Co ratio. Ga filled samples also exhibit enhanced Seebeck coefficients compared to sample Y60. But unlike Y65, their resistivities remain almost the same as Y60, a phenomenon quite different from that expected for ordinary doping optimization. As a result, the power factors in these Ga filled samples demonstrated an over 30% enhancement compared to Y60, as shown in Figure 82. The power factor for the best performing sample Y60G10 reaches 25 $Wcm^{-1}K^{-2}$ at 810K.

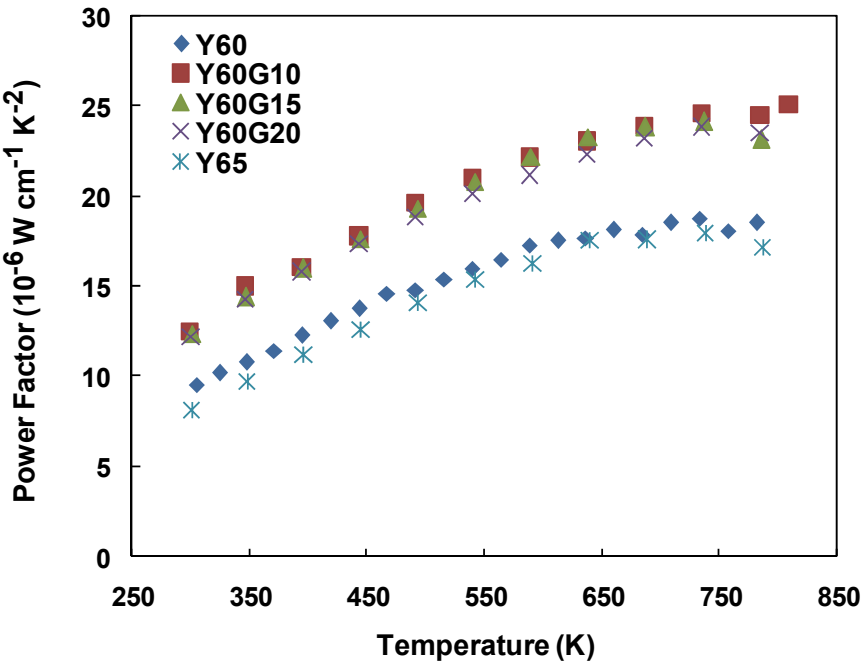

Figure 82 Power factor as a function of temperature.

Figure 83 shows the thermal conductivity as a function of temperature. The lattice thermal conductivity κ_l is obtained by subtracting the electronic thermal conductivity $\kappa_e=L\sigma T$ from the total thermal conductivity κ. Here, we use the Lorenz number $L=2\times10^{-8}$ V^2 K^{-2}, a value typically used for filled skutterudites.[108] The lattice thermal conductivity is first reduced slightly with Ga filling in Y60G10, and rises up with higher Ga filling in Y60G15 and Y60G20.

This can be understood as the actually Yb filling fraction may be affected by the extra filler Ga. As it is seen from Figure 80, trace amount of Yb impurity phase is present in samples with Ga, which indicates adding Ga indeed repels some Yb out of the skutterudite cages. The similar phenomenon has also been reported by Xiong *et al* in n-type Yb filled skutterudite with Ga[107], where actual Yb filling fraction decreases with increasing Ga. Thus, the lattice thermal conductivity reflects the collateral effects of additional phonon scattering from second filler Ga and the loss of primary filler Yb.

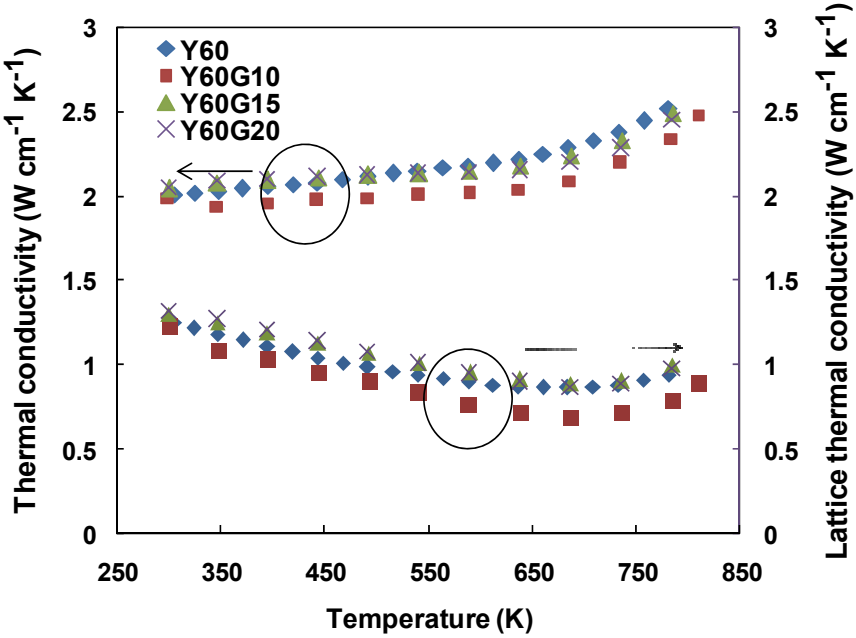

Figure 83 Total thermal conductivity and lattice thermal conductivity as a function of temperature.

Because of the enhanced power factors, Ga filled samples demonstrate enhanced *ZTs* compared to that of Y60 as shown in Figure 84. Sample Y60G10 exhibits the highest ZT_{max}=0.83 at 736K, which is 46% enhancement compared to that of Y60, and over 100% enhancement compared to ZT_{max}=0.4 in $YbFe_4Sb_{12}$ from an earlier report.[91]

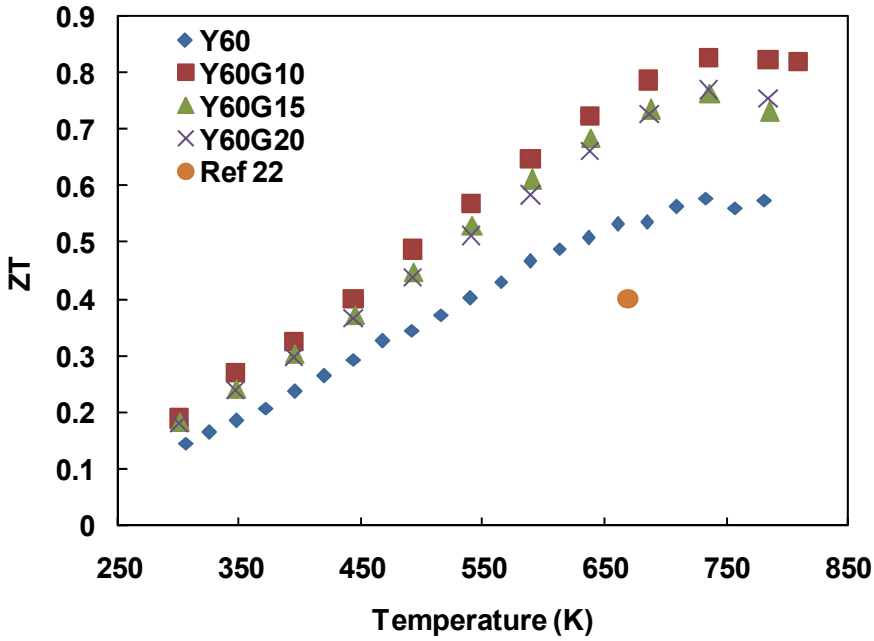

Figure 84 *ZT* as a function of temperature. Ref represents *ZT* of $YbFe_4Sb_{12}$ reported by Kuznetsov and Rowe[91]

7.3 Discussion

As we have seen repeatedly throughout this work, a good way to probe the behavior of Seebeck coefficient is to plot the "Pisarenko relation",[36] which is the Seebeck coefficient as a function of carrier concentration. A series of control samples of various Seebeck coefficients and carrier concentrations create a fit line based on Equation 77 which assumes comparable DOS effective mass m^* and scattering parameter s for compounds of similar compositions. If samples significantly deviate from such a fit line, it is a good indication of either a different m^* or s. Figure 85 is the Pisarenko relation at room temperature for our skutterudite samples, where sample Y60, Y65, and other single filled Yb samples create the fit line. It is obvious that at the

same carrier concentration, samples co-filled with Ga have a higher Seebeck coefficient compared to those without Ga.

$$S = \frac{k}{e}\left(s + 2 + \ln \frac{2\left(2\pi m^* kT\right)}{h^3 n} \right) \qquad 77$$

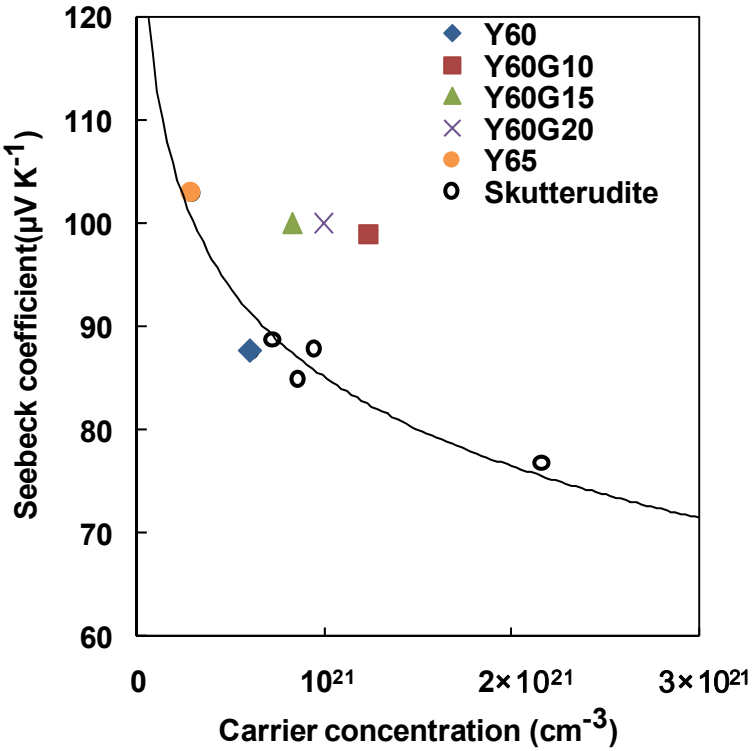

Figure 85 Pisarenko relation of single filled Yb based p-type skutterudite and Yb Ga double filled skutterudite at 300K. Circles in the figure represent additional Yb filled skutterudite samples. Fit line represents the logarithmic relation expressed by Equation 74 and serves as an aid to the eye.

To understand which of m^* and s is the dominant mechanism for the enhanced Seebeck coefficient in Ga filled samples, we measured the Nernst coefficient and applied the method of four coefficients to compute m^* and s. Details of this method have already been mentioned in previous chapter. In this study, we use the non-parabolic band model described by Equation 78,

$$\frac{\hbar^2 k^2}{2m_v^*} = E\left(1 + \frac{E}{E_g}\right) \quad 78$$

which has been used to study the band structure of $CoSb_3$.[99-101] The band gap E_g=0.5eV is adapted from literature on $YbFe_4Sb_{12}$.[102, 103] Using this method, we calculate m^*, s, and E_F for all our samples listed in Table 7. From classical physics, the DOS $g(E) \propto (m^*)^{3/2}$, so the energy dependence of m^* can be viewed at least as a qualitative reflection of the shape of $g(E)$. As shown in Figure 86(a), at 300K, Ga filled samples exhibit a higher effective mass m^* compared to Y60 at a Fermi energy level closer to the valence band edge, between 35meV and 54meV in contrast to over 100meV for Y60. Sample Y65 is also pushed closer to the valence band edge at approximately 30meV, which is expected due to the low carrier concentration. The slightly increased m^* appears to reflect the natural DOS of Yb-filled p-type skutterudite near the valence band edge,[102, 103] but smaller m^* for Y65 means it has less carriers and should enter the intrinsic region at a lower temperature compared to Ga-filled samples. This agrees with Figure 82 which shows that the Seebeck coefficient of sample Y65 reaches a maximum near 740K and begins to decrease above that temperature. The single filled Yb samples forms a relatively flat slope while the much higher m^* found in Ga co-filled samples suggests the existence of spike like features in $g(E)$ which translates to a larger Seebeck coefficient. This finding is also corroborated by the carrier concentration data shown in Figure 87. When Ga is inserted into the voids of skutterudites, it should contribute electrons. Su et al estimated that each Ga donates 0.9 electrons.[105] If this is the case, the hole concentration should decrease instead of increase in our Ga-filled samples. The anomalous increase of the hole concentration combined

(a)

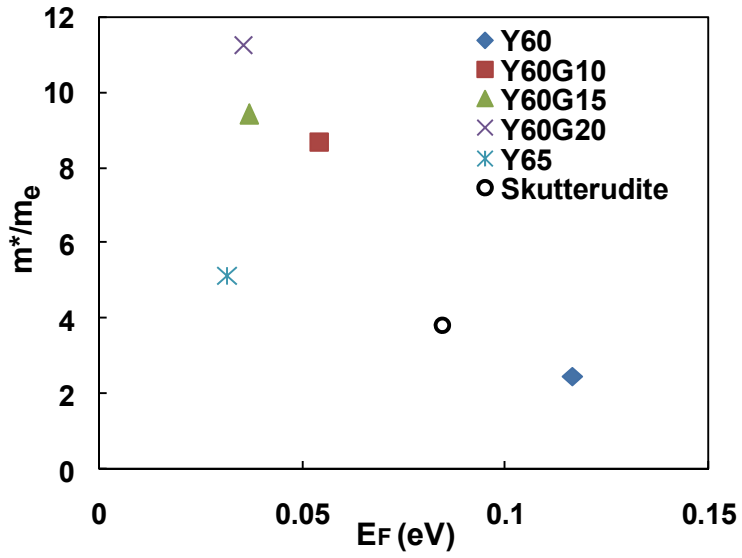

(b)

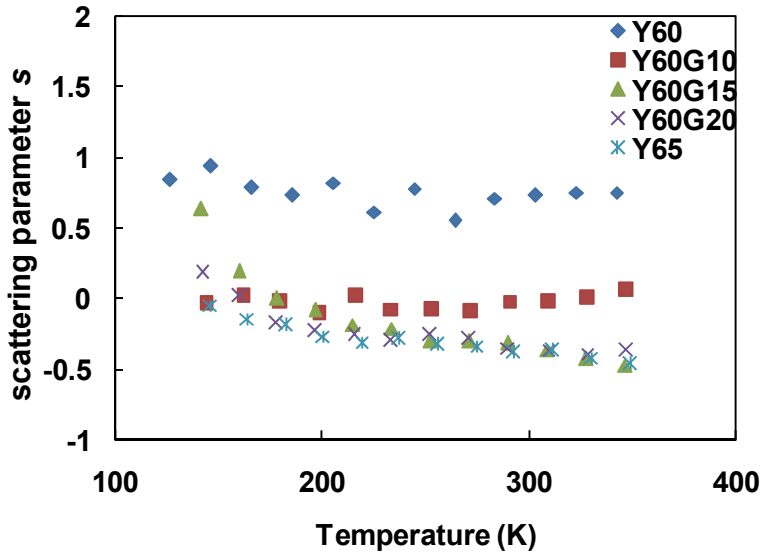

Figure 86 (a) DOS effective mass as a function of Fermi energy E_F at 300K. Circle represents Yb filled skutterudite and serves as supplemental datum. (b) Carrier scattering parameter s as a function of temperature.

with the reduced Fermi level suggests the deep defect states induced by Ga alter the band structure closer to the valence band edge. The scattering parameters *s* shown in Figure 86(b)

imply a neutral impurity scattering for Y60 and acoustic phonon scattering for other samples, so that *s* is not the driving force for the enhanced Seebeck coefficient.

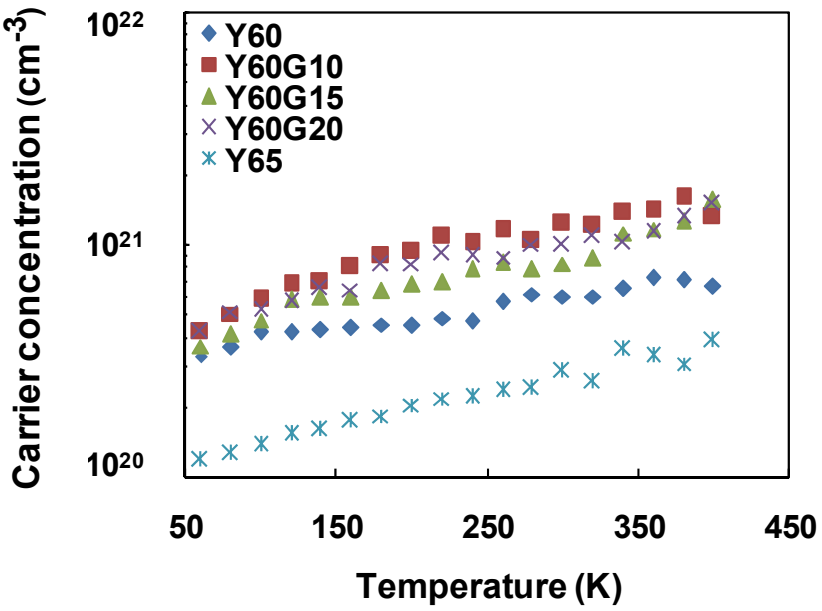

Figure 87 Carrier concentration as a function of temperature.

7.4 Summary of the chapter

In conclusion, we have successfully synthesized double filled p-type skutterudite $Yb_{0.6}Ga_zFe_2Co_2Sb_{12}$. The results suggest that the second filler atom Ga induces a deep defect level in the band structure which pins the Fermi level closer to the valence band edge. The unique role of Ga greatly enhances the Seebeck coefficient without affecting the electrical conductivity. The best performing sample has a ZT_{max}=0.83 at 736K which is 46% enhancement compared to the control sample synthesized by ourselves, and over 100% enhancement compared to ZT_{max} =0.4 in $YbFe_4Sb_{12}$ from an earlier report.[91] Although, such a *ZT* value is still lower than *ZT*=0.9 in $Ce_{0.9}Fe_{3.5}Co_{0.5}Sb_{12}$ (synthesized in our laboratory) and the even higher

ZT in didymium-filled skutterudites[40, 109], it certainly narrows the gap and demonstrates the potential for the once overlooked Yb-filled p-type skutterudites. Future theoretical calculations on the band structure of partially filled skutterudite may improve our understanding of the influence of defect states and guide the exploration for p-type skutterudites with higher *ZT*.

Chapter 8 Conclusions and Future Work

We have successfully employed multiple approaches to synthesize bulk nanocomposite materials for thermoelectric applications. Two material systems are of our interest: they are bismuth telluride and its alloy based nanocomposites, and p-type skutterudite based nanocomposites.

For bismuth telluride and its alloys based nanocomposites, we select $Bi_2Te_{2.85}Se_{0.15}$ as the n-type matrix and $Bi_{0.4}Sb_{1.6}Te_3$ as the p-type matrix respectively. Through careful process optimization, we obtain matrix materials with reproducible TE properties. The nanocomposite materials were prepared by a solution based incipient wetness impregnation method, followed by burning off the organic ligands and consolidating the powders by hot pressing. TEM images suggest that the PbTe nanoparticles retain their nano-sized feature after hot pressing. For n-type nanocomposites, adding PbTe nanoparticles create a two carrier system which severely degrade the electronic properties. For p-type nanocomposites, adding PbTe nanoparticles can more effectively reduce the lattice thermal conductivity at lower temperature. But the doping effect from the excess Pb ion plays a dominant role compared to nanostructuring which increases electrical conductivity but decreases the Seebeck coefficient. This results in a decreased power factor. The total thermal conductivity is not reduced for nanocomposites as well due to the enhanced contribution from the electronic thermal conductivity.

For skutterudite based nanocomposites, we focus our attention on the under-developed p-type skutterudites. We start from the primitive Fe-doped binary skutterudite nanocomposite $Co_{0.9}Fe_{0.1}Sb_3$ with in-situ formed $FeSb_2$ as nanoparticles to test the viability of this approach.

The best performing nanocomposites enhance the *ZT* by a factor two compared to the control sample. The success led us to proceed with filled skutterudite with antimony impurities as the nano-inclusions. A new Yb filled p-type skutterudite is developed as the matrix material. By revising the synthesis procedure, we successfully reduce the spontaneous reaction between the rare earth element and the quartz ampoule, thus enhancing the thermoelectric power factor by 100% and the *ZT* by 50% compared to the literature reported a decade ago. We explored the thermoelectric properties of Yb filled p-type skutterudite nanocomposites for a wide range of Yb filling fraction and $FeSb_2$ amount. We discovered enhanced power factors in these nanocomposites when the Yb filling fraction is not greater than 0.7. The best performing nanocomposites were found when Yb filling fraction is 0.6. These nanocomposite compositions embody and exemplify all the theoretical and technical advancements in thermoelectrics: using rattlers to scatter phonons, creating a solid solution by partially filling the voids and using Fe substitution on Co site, and taking advantage of naturally occurring nanoscopic impurity phases to further improve *ZT*. By combining our results with other literature reports, we find that the marginal enhancement of nanocomposite tends to dwindle as the properties of the matrix materials are enhanced, from a 100% enhancement in our prototype demonstration in binary skutterudite nanocomposites, to 23% enhancement to p-type filled skutterudites to merely 14% in advanced n-type skutterudites.[27, 107, 110].

Last but not least, we investigated the double filled p-type skutterudite $Yb_{0.6}Ga_zFe_2Co_2Sb_{12}$. The unique role of Ga inducing a deep defect state in band structure greatly enhances the Seebeck coefficient without affecting the electrical resistivity. The best performing sample has a ZT_{max}=0.83 at 736K which is 46% enhancement compared to

$Yb_{0.6}Fe_2Co_2Sb_{12}$ with only Yb filler and over 100% enhancement compared an earlier report.[91] Such a *ZT* value certainly makes these double filled skutterudites an alternative to Ce-filled skutterudite due to their reduced consumption of precious rare-earth elements.

Future work for preparing bulk nanocomposites should seek more compatible material systems where the feasibility of the approach and the complexity of the possible interactions between the matrix material and nano-inclusions should be given all-round evaluation before the execution of the project. Nanostructuring should not be deemed as a preconceived elixir to the enhancement of TE properties aforehand, not even for the reduction of thermal conductivity, but as a high risk adventure where the property matching between matrix material and nano-inclusions is crucial. An abundant nano material supply and well-equipped characterization facilities are needed to guarantee a thorough investigation. For in-situ synthesized bulk nanocomposite materials, it remains a question if this approach is viable for mass production as the cooling rate in a big ingot is quite different from a laboratory scale trial experiments. But the melt-spinning technique at least opens a door to the possibility. In addition, there is still room for improving the electronic properties through band structure engineering. More theoretical calculations are needed to guide the experimental work.

While “nano” has been employed by many researchers as the ultimate solution to many problems, it does seem to provide significant benefits when applied to thermoelectrics. Time and more research will tell if this approach is ultimately a viable one.

Bibliography

Bibliography

[1] HJ Goldsmid (1960) Applications of Thermoelectricity. John Wiley & Sons Inc., New York

[2] JR Drabble, HJ Goldsmid (1961) Thermal Conduction in Semiconductors. Pergamon Press,

[3] TM Tritt (2004) Thermal Conductivity, Theory, Properties and Applications. Kluwer Academic/Plenum Publishers, New York

[4] R Berman (1976) Thermal conduction in Solids. Oxford Univeristy Press, Oxford

[5] GA Slack, S Galginaitis (1964) Physical Review 133: A253. Doi:10.1103/PhysRev.133.A253

[6] AV Ioffe, AF Ioffe (1954) Dokl. Akad. Nauk SSSR. 97: 821.

[7] AV Ioffe, AF Ioffe (1954) Dokl. Akad. Nauk SSSR. 98: 757.

[8] AV Ioffe, AF Ioffe (1956) Izv. Akad. Nauk SSSR 20: 65.

[9] SR Brown, SM Kauzlarich, F Gascoin, G Jeffrey Snyder (2006) Chemistry of Materials 18: 1873.

[10] DT Morelli, GP Meisner (1995) Journal of Applied Physics 77: 3777.

[11] LD Hicks, MS Dresselhaus (1993) Physical Review B 47: 16631.

[12] X Sun, Z Zhang, MS Dresselhaus (1999) Applied Physics Letters 74: 4005.

[13] MS Dresselhaus, G Chen, MY Tang, et al. (2007) Advanced Materials 19: 1043.

[14] DKC MacDonald (1961) Thermoelectricity: an introduction to the principles. John Wiley & Sons, Inc.,

[15] LD Hicks, TC Harman, X Sun, MS Dresselhaus (1996) Physical Review B 53: 10493.

[16] TC Harman, DL Spears, MJ Manfra (1996) Journal of Electronic Materials 25: 1121.

[17] T Koga, SB Cronin, MS Dresselhaus, JL Liu, KL Wang (2000) Applied Physics Letters 77: 1490.

[18] TC Harman, PJ Taylor, MP Walsh, BE LaForge (2002) Science 297: 2229.

[19] R Venkatasubramanian, E Siivola, T Colpitts, B O'Quinn (2001) Nature 413: 597.

[20] SJ Thiagarajan, V Jovovic, JP Heremans (2007) Physica Status Solidi-Rapid Research Letters 1: 256. Doi:10.1002/pssr.200701144

[21] JP Heremans, CM Thrush, DT Morelli (2004) Physical Review B 70.

[22] X Shi, J Yang, JR Salvador, et al. (2011) Journal of the American Chemical Society 133: 7837.

[23] KF Hsu, S Loo, F Guo, et al. (2004) Science 303: 818. Doi:10.1126/science.1092963

[24] J Androulakis, KF Hsu, R Pcionek, et al. (2006) Advanced Materials 18: 1170. Doi:10.1002/adma.200502770

[25] YZ Pei, J Lensch-Falk, ES Toberer, DL Medlin, GJ Snyder (2011) Advanced Functional Materials 21: 241. Doi:10.1002/adfm.201000878

[26] JP Heremans, V Jovovic, ES Toberer, et al. (2008) Science 321: 554. Doi:10.1126/science.1159725

[27] H Li, XF Tang, QJ Zhang, C Uher (2009) Applied Physics Letters 94: 102114. Doi:10.1063/1.3099804

[28] DY Chung, T Hogan, P Brazis, et al. (2000) Science 287: 1024. Doi:10.1126/science.287.5455.1024

[29] DY Chung, TP Hogan, M Rocci-Lane, et al. (2004) Journal of the American Chemical Society 126: 6414. Doi:10.1021/ja039885f

[30] MV Vedernikov, VA Kutasov, LN Luk'yanova, PP Konstantinov (1997) Proceedings of the 1997 16th International Conference on Thermoelectrics, ICT'97, August 26, 1997 - August 29, 1997IEEE, Dresden, Ger

[31] O Yamashita, S Sugihara (2005) Journal of Materials Science 40: 6439.

[32] JP Fleurial, L Gailliard, R Triboulet, H Scherrer, S Scherrer (1988) Journal of Physics and Chemistry of Solids 49: 1237.

[33] JP Fleurial, L Gailliard, R Triboulet, H Scherrer, S Scherrer (1988) Journal of Physics and Chemistry of Solids 49: 1249.

[34] M Carle, P Pierrat, C LaHallegravier, S Scherrer, H Scherrer (1995) Journal of Physics and Chemistry of Solids 56: 201. Doi:10.1016/0022-3697(94)00166-9

[35] T Caillat, M Carle, P Pierrat, H Scherrer, S Scherrer (1992) Journal of Physics and Chemistry of Solids 53: 1121. Doi:10.1016/0022-3697(92)90087-t

[36] AF Ioffe (1957) Semiconductor Thermoelements and Thermoelectric Cooling. Infosearch Limited, London

[37] T Caillat, JP Fleurial, A Borshchevsky (1997) Journal of Physics and Chemistry of Solids 58: 1119. Doi:10.1016/s0022-3697(96)00228-4

[38] GS Nolas, M Kaeser, RT Littleton, TM Tritt (2000) Applied Physics Letters 77: 1855. Doi:10.1063/1.1311597

[39] PF Qiu, J Yang, RH Liu, et al. (2011) Journal of Applied Physics 109: 063713. Doi:10.1063/1.3553842

[40] G Rogl, A Grytsiv, P Rogl, et al. (2010) Intermetallics 18: 2435.

[41] G Rogl, A Grytsiv, P Rogl, E Bauer, M Zehetbauer (2011) Intermetallics 19: 546. Doi:10.1016/j.intermet.2010.12.001

[42] JP Dismukes, E Ekstrom, DS Beers, EF Steigmeier, I Kudman (1964) Journal of Applied Physics 35: 2899. Doi:10.1063/1.1713126

[43] XF Tang, P Li, SK Deng, QJ Zhang (2008) Journal of Applied Physics 104: 013706. Doi:10.1063/1.2951888

[44] C Yu, TJ Zhu, RZ Shi, Y Zhang, XB Zhao, J He (2009) Acta Materialia 57: 2757. Doi:10.1016/j.actamat.2009.02.026

[45] A Gueguen, PFP Poudeu, C-P Li, et al. (2009) Chemistry of Materials 21: 1683. Doi:10.1021/cm803519p

[46] EA Skrabek, DS Trimmer (03/08/1972) Teledyne, Inc., USA

[47] DM Rowe (2005-12-09) Thermoelectrics Handbook MACRO TO NANO. CRC,

[48] DL Young, TJ Coutts, VI Kaydanov, AS Gilmore, WP Mulligan (2000) Journal of Vacuum Science and Technology A: Vacuum, Surfaces and Films 18: 2978.

[49] IA Chernik, VI Kaidanov, Vinograd.Mi, Kolomoet.Nv (1968) Soviet Physics Semiconductors-Ussr 2: 645.

[50] V Jovovic, SJ Thiagarajan, JP Heremans, T Komissarova, D Khokhlov, A Nicorici (2008) Journal of Applied Physics 103. Doi:053710
10.1063/1.2890150

[51] V Jovovic, SJ Thiagarajan, J West, et al. (2007) Journal of Applied Physics 102. Doi:10.1063/1.2771048

[52] DJ Bergman, O Levy (1991) Journal of Applied Physics 70: 6821. Doi:10.1063/1.349830

[53] S Ganguly, SL Brock (2011) Journal of Materials Chemistry 21: 8800.

[54] O Yamashita, S Tomiyoshi (2004) Journal of Applied Physics 95: 6277.

[55] HP Ha, DB Hyun, JY Byun, YJ Oh, EP Yoon (2002) Journal of Materials Science 37: 4691.

[56] O Yamashita, S Tomiyoshi, K Makita (2003) Journal of Applied Physics 93: 368.

[57] JR Wiese, L Muldawer (1960) Journal of Physics and Chemistry of Solids 15: 13.

[58] TS Oh, DB Hyun, NV Kolomoets (2000) Scripta Materialia 42: 849.

[59] H-C Kim, S-K Lee, T-S Oh, D-B Hyun (1998) IEEE, Nagoya, Jpn

[60] HP Ha, TH Kim, DB Hyun, EP Yoon (2001) Society of Materials Science Japan, Akita, Japan

[61] I Yashima, H Watanave, T Ogisu, R Tsukuda, S Sato (1998) Japanese Journal of Applied Physics Part 1-Regular Papers Short Notes & Review Papers 37: 2472.

[62] JJ Lidong Chen, Xun Shi (2003) Mat. Res. Soc. Symp. Proc. Materials Research Society,

[63] JM Schultz, WA Tiller, JP McHugh (1962) Journal of Applied Physics 33: 2443.

[64] H Scherrer, R Martin-Lopez, B Lenoir, A Dauscher, S Scherrer (2001) Institute of Electrical and Electronics Engineers Inc., Beijing, China

[65] WS Choi, BG Park, IM Park, YH Park (2008) Metals and Materials International 14: 701.

[66] Z Stary, J Horak, M Stordeur, M Stolzer (1988) Journal of Physics and Chemistry of Solids 49: 29.

[67] J Horak, Z Stary, P Lostak, J Pancir (1990) Journal of Physics and Chemistry of Solids 51: 1353.

[68] P Pecheur, G Toussaint (1994) Journal of Physics and Chemistry of Solids 55: 327.

[69] DV Talapin, CB Murray (2005) Science (Washington, DC, United States) 310: 86.

[70] M Law, JM Luther, Q Song, BK Hughes, CL Perkins, AJ Nozik (2008) Journal of the American Chemical Society 130: 5974.

[71] D Kusano, Y Hori (2002) Thermoelectrics, 2002. Proceedings ICT '02. Twenty-First International Conference on,

[72] T Plechacek, J Horak (1999) Journal of Solid State Chemistry 145: 197.

[73] T Plechacek, J Navratil, J Horak, P Lost'ak (2004) Philosophical Magazine 84: 2217. Doi:10.1080/14786430410001678226

[74] PW Zhu, Y Imai, Y Isoda, Y Shinohara, XP Jia, GT Zou (2005) Journal of Physics-Condensed Matter 17: 7319. Doi:10.1088/0953-8984/17/46/015

[75] T Caillat, A Borshchevsky, JP Fleurial (1993) Proceedings of the 28th Intersociety Energy Conversion Engineering Conference, August 8, 1993 - August 13, 1993Publ by SAE, Atlanta, GA, USA

[76] GS Nolas, DT Morelli, TM Tritt (1999) Annual Review of Materials Science 29: 89. Doi:10.1146/annurev.matsci.29.1.89

[77] C Uher (2001) Semiconductors and Semimetals. Academic Press, San Diego

[78] BX Chen, JH Xu, C Uher, et al. (1997) Physical Review B 55: 1476.

[79] DT Morelli, T Caillat, JP Fleurial, et al. (1995) Physical Review B 51: 9622.

[80] DJ Braun, W Jeitschko (1980) Journal of the Less-Common Metals 72: 147.

[81] DJ Braun, W Jeitschko (1980) Journal of Solid State Chemistry 32: 357.

[82] W Jeitschko, D Braun (1977) Acta Crystallographica Section B-Structural Science 33: 3401.

[83] DM Rowe (1995) CRC Handbook of Thermoelectrics. CRC Press, Boca Raton, London

[84] BC Sales, D Mandrus, RK Williams (1996) Science 272: 1325.

[85] X Shi, H Kong, CP Li, et al. (2008) Applied Physics Letters 92: 182101.

[86] G Chen, MS Dresselhaus, G Dresselhaus, JP Fleurial, T Caillat (2003) International Materials Reviews 48: 45.

[87] J Yang, GP Meisner, DT Morelli, C Uher (2001) Physical Review B 63: 014410.

[88] JR Salvador, J Yang, X Shi, et al. (2009) Philosophical Magazine 89: 1517.

[89] XF Tang, LD Chen, G Takashi, H Toshio, RZ Yuan (2000) Acta Physica Sinica 49: 1120.

[90] XY Zhao, X Shi, LD Chen, et al. (2006) Applied Physics Letters 89: 092121. Doi:092121 10.1016/1.2345249

[91] VL Kuznetsov, DM Rowe (2000) Journal of Physics-Condensed Matter 12: 7915.

[92] D Berardan, C Godart, E Alleno, S Berger, E Bauer (2003) Journal of Alloys and Compounds 351: 18.

[93] DT Morelli, GP Meisner, BX Chen, SQ Hu, C Uher (1997) Physical Review B 56: 7376.

[94] E Bauer, A Galatanu, H Michor, et al. (2000) European Physical Journal B 14: 483.

[95] J-P Fleurial, A Borshchevsky, T Caillat, DT Morelli, GP Meisner (1996) Proceedings of the 1996 15th International Conference on Thermoelectrics, ICT'96, March 26, 1996 - March 29, 1996, Pasadena, CA, USA

[96] C Zhou, D Morelli, X Zhou, G Wang, C Uher (2011) Intermetallics 19: 1390. Doi:doi:10.1016/j.intermet.2011.04.015

[97] C Zhou, J Sakamoto, D Morelli, X Zhou, G Wang, C Uher (2011) Journal of Applied Physics 109: 063722.

[98] V Jovovic, SJ Thiagarajan, JP Heremans, T Komissarova, D Khokhlov, A Nicorici (2008) Journal of Applied Physics 103: 7. Doi:10.1063/1.2890150

[99] DJ Singh, WE Pickett (1994) Physical Review B 50: 11235.

[100] JO Sofo, GD Mahan (1999) Materials Research Society Symposium - Proceedings 545: 315.

[101] K Koga, K Akai, K Oshiro, M Matsuura (2002) Thermoelectric Materials 2001-Research and Applications, November 26, 2001 - November 29, 2001Materials Research Society, Boston, MA, United states

[102] YS Dedkov, SL Molodtsov, H Rosner, et al. (2007) Physica C: Superconductivity and its Applications 460-462 I: 698.

[103] K TAKEGAHARA, H HARIMA (2002) J Phys Soc Jpn 71: 240.

[104] S Ahmad, K Hoang, SD Mahanti (2006) Physical Review Letters 96: 056403. Doi:10.1103/PhysRevLett.96.056403

[105] XL Su, XF Tang, H Li, SK Deng (2008) Acta Physica Sinica 57: 6488.

[106] A Harnwunggmoung, K Kurosaki, T Plirdpring, et al. (2011) Journal of Applied Physics 110: 013521. Doi:10.1063/1.3606417

[107] Z Xiong, XH Chen, XY Huang, SQ Bai, LD Chen (2010) Acta Materialia 58: 3995. Doi:10.1016/j.actamat.2010.03.025

[108] J Graff, S Zhu, T Holgate, J Peng, J He, TM Tritt (2011), 5 edn. Springer New York, 233 Springer Street, New York, NY 10013-1578, United States

[109] G Rogl, A Grytsiv, P Rogl, E Bauer, M Zehetbauer (2011) Intermetallics 19: 546.

[110] H Li, X Tang, Q Zhang, C Uher (2008) Applied Physics Letters 93: 252109.